Olga Sergeevna Kleptsova

Unstructured Orthogonal Meshes for Modeling

Coastal and Ocean Flows

Unstructured Orthogonal Meshes for Modeling Coastal and Ocean Flows

---

PROEFSCHRIFT

ter verkrijging van de graad van doctor
aan de Technische Universiteit Delft,
op gezag van de Rector Magnificus prof.ir. K.C.A.M. Luyben,
voorzitter van het College voor Promoties,
in het openbaar te verdedigen

op vrijdag 26 april 2013 om 12:30 uur

door

Olga Sergeevna KLEPTSOVA

ingenieur in de toegepaste wiskunde
geboren te Sidorovka, Sovjet Unie

Dit proefschrift is goedgekeurd door de promotoren:
Prof.dr. J.D. Pietrzak
Prof.dr.ir. G.S. Stelling

Samenstelling promotiecommissie:

Rector Magnificus, voorzitter	Technische Universiteit Delft, NL
Prof.dr. J.D. Pietrzak, promotor	Technische Universiteit Delft, NL
Prof.dr.ir. G.S. Stelling, promotor	Technische Universiteit Delft, NL
Prof.Dr. V. Casulli	University of Trento, IT
Prof.dr.ir. J.A. Roelvink,	UNESCO-IHE Institute for Water Education, NL
Prof.dr.ir. A.W. Heemink,	Technische Universiteit Delft, NL
Dr. O.B. Fringer,	Stanford University, USA
Dr. Jacek A. Jankowski,	Bundesanstalt für Wasserbau, DE
Prof.dr.ir. A.E. Mynett, reservelid	Technische Universiteit Delft, NL

CIP-DATA KONINKLIJKE BIBLIOTHEEK, DEN HAAG

Olga Sergeevna Kleptsova

Unstructured Orthogonal Meshes for Modeling Coastal and Ocean Flows
Delft: TU Delft, Faculteit Civiele Techniek en Geowetenschappen
Thesis Technische Universiteit Delft.

Met samenvatting in het Nederlands.

ISBN 978-90-8891-610-6

Subject headings: shallow-water equations, modelling, unstructured mesh.

Printed by: Proefschriftmaken.nl || Uitgeverij BOXPress, The Netherlands.

To my teachers, colleagues, friends, and family

Unstructured Orthogonal Meshes for Modeling Coastal and Ocean Flows

Olga Sergeevna Kleptsova

Abstract

In this thesis a $z-$layer unstructured C-grid finite volume hydrostatic model is presented. An efficient and highly scalable implicit technique for the solution of the free surface equation is combined with an Eulerian approach for the advection of momentum. A consistent velocity reconstruction procedure which not only satisfies the continuity law but also guarantees the discrete kinetic energy conservation is presented. It is shown that an accurate velocity reconstruction procedure is of crucial importance not only for discretization of the Coriolis term, but also for the correct advection of momentum, especially in the multilayer case. Unlike other $z-$layer models the method presented here ensures that the staircase representation of bathymetry and free surface has no influence on the vertical structure of the flow. The method is therefore guaranteed to be strictly momentum conservative, also in the layers containing the free surface and bed.

A number of test cases are presented to show that the model is able to accurately simulate Coriolis dominated flows and flooding and drying processes both in the depth-averaged case and in the presence of multiple $z-$layers. A simulation of the 2004 Indian Ocean tsunami is used to evaluate the ability of the method to simulate fast propagating tsunami waves and detailed inundation processes. Results obtained using two different rupture models are compared to the tide gauge arrival times, satellite altimetry data and the inundation observations in the Banda Aceh area. The comparison is used not only to assess the quality of the underlying rupture models but also to determine the value of the available data sources for such an assessment.

Preliminary results of the unstructured grid fine resolution tidal model the southern North Sea including the Rhine-Scheldt Delta region are presented. The model is able to correctly reproduce the essential characteristics of the M2 tide, as well as of the most important nonlinear shallow water overtides M4 or M6. The simulated velocity field was used to evaluate the Simpson-Hunter stratification parameter, the variability of frontal positions due to tidal advection and spring-neap adjustment.

Unstructured Orthogonal Meshes for Modeling Coastal and Ocean Flows

Olga Sergeevna Kleptsova

Samenvatting

In dit proefschrift wordt een ongestructureerd C-type grid, eindige-volume, hydrostatisch model met z-lagen gepresenteerd. Een efficinte en zeer schaalbare, impliciete techniek voor het oplossen van de vrije wateroppervlak vergelijking wordt gecombineerd met een Euleriaanse aanpak voor het transport van impuls. Een consistente snelheidsreconstructie procedure wordt gepresenteerd die niet alleen aan de continuteitsvergelijking voldoet, maar ook aan discreet energiebehoud. Aangetoond wordt dat een nauwkeurige snelheidsreconstructie cruciaal is voor zowel de Coriolis term als het juiste transport van impuls, vooral in het geval van meerdere lagen. De methode in dit proefschrift verzekert, in tegenstelling tot andere z-lagen modellen, dat een trapsgewijze representatie van de bathymetrie en het vrije wateroppervlak geen invloed heeft op de verticale structuur van de stroming. De methode gegarandeerd daarom strikt impuls behoud, ook in de lagen die het vrij wateroppervlak en de bodem bevatten.

Een aantal testgevallen toont aan dat het model in staat is om nauwkeurig Coriolis gedomineerde stromingen en overstromingen en droogvallen te modelleren, zowel in het diepte-gemiddelde geval, als in de aanwezigheid van meerdere z-lagen. Een simulatie van de tsunami in de Indische Oceaan van 2004 is gebruikt om te evalueren of de methode in staat is om snel voortplantende golven en gedetailleerde inundatie te simuleren. Resultaten met twee verschillende breukmodellen worden vergeleken met gemeten peilschaal aankomsttijden, satelliet hoogtedata en inundatie observaties in het Banda Aceh gebied. Deze vergelijking wordt niet alleen gebruikt om de kwaliteit van de onderliggende breukmodellen te beoordelen, maar ook om de waarde van dergelijke beschikbare bronnen in te schatten.

Voorlopige resultaten van het ongestructureerde fijn-grid getij model van de zuidelijke Noordzee, inclusief de Rijn-Schelde Delta gebied, worden gepresenteerd. Het model is in staat om de essentile eigenschappen van het M2 getij correct te reproduceren, alsmede de meest belangrijke niet-lineaire ondiepwater hoger harmonischen M4 en M6. Het gesimuleerde snelheidsveld is gebruikt om de Simpson-Hunter stratificatie parameter, de variabiliteit van de frontale posities ten gevolge van getij-transport en spring-doodtij variaties te bepalen.

Acknowledgments

First of all I would like to acknowledge the Department of Mathematics at Ufa State Aviation Technical University which provided an excellent education in theoretical mathematics.

I am very grateful to Prof. Roger M. Cooke and Prof. Arnold W. Heemink for accepting me as a MSc student for the Risk and Environmental Modeling programme. Participating in the programme was a great experience which allowed me to finally apply my theoretical knowledge to practical problems. This study connected probability theory and statistics, my BSc major, to numerical modeling which became the topic of my PhD project.

I am very grateful to my promotors Prof. Julie Pietrzak and Prof. Guus Stelling for believing in my strengths and tolerating my weaknesses. I greatly enjoyed the working experience with Julie and Guus, who made many significant contributions to my work, to my knowledge and skills.

I would also like to thank all the members of my thesis committee for their interest in my work, for their desire to participate in the committee, and for the useful remarks improving the thesis.

I am very thankful to my parents, my sister and especially to my husband Demid Borodin for always being there for me, for their support and understanding.

I would like to thank Sander van der Pijl for his help with the Dutch translation.

Olga Sergeevna Kleptsova Delft, The Netherlands, April 2013

Table of Contents

List of Figures

List of Tables

1 Introduction

To accurately model processes in the coastal ocean, and in particular to simulate flows in the shallow near shore region, including flooding and drying problems, it is important to employ a high resolution grid. By using unstructured grids it is possible to achieve highly variable resolution in complex geometries and thus to resolve accurately particular regions of interest, while modeling other regions at an acceptable cost. Staggered mesh methods are attractive in incompressible fluid dynamics since they do not display spurious pressure modes, allow the exact satisfaction of the continuity equation and are shown to have a number of local conservation properties. While many staggering schemes are possible, the so called C-grid staggering is of particular interest.

In a staggered C-grid the velocity points are placed at the mid-points of the cell edges and the pressure or elevation points are located at the cell centers. It is worth noting that the cell centers do not necessarily coincide with the polygon geometric centers. A number of oceanographic models using the C-grid staggering have been recently developed. These models all discretize the continuity equation in a finite-volume manner, but differ in the way velocity is calculated. Models by Walters and Casulli (2001); Miglio et al. (1999); Hanert et al. (2009) use a finite-element approach, whereas Casulli and Walters (2000); Casulli and Zanolli (2002) discretize the momentum equation in a finite-difference manner. Each of the methods has it own advantages and disadvantages. The finite-difference schemes are in general more efficient, but they require a careful treatment of the Coriolis term. Depending on the placement of the pressure variables finite-difference models may also have significant restrictions on the grid. A detailed comparison of the finite-difference and finite-elements methods can be found in Walters et al. (2009); Hanert et al. (2003).

Both the structured and unstructured finite-difference C-grid based models solve for the cell normal velocities. The full velocity vector which is required in the calculation of the momentum advection and Coriolis terms needs to be interpolated from the surrounding cell normal values. The tangential velocity reconstruction is not an obvious task for either structured or unstructured grids. Espelid et al. (2000) showed for structured grids that an improper discretization of the Coriolis term can become an infinite source of energy, especially in the case of variable bottom topography. For unstructured grids the problem was explored by for example, Perot (2000); Ham et al. (2007); Kleptsova et al. (2009). It was shown that the interpolation should be consistent and ensure no energy production due to the Coriolis term. The latter requirement is fulfilled if the velocity reconstruction is such that the matrix of the semi-discrete system of equations is skew-symmetric. This is a necessary, but not sufficient condition for model stability.

A mesh obtained by the standard Delaunay procedure for which all circumcenters are within the triangles is called orthogonal. Although generation of the unstructured orthogonal meshes requires much more effort than the generation of other meshes, they have some attractive properties. Since the interval joining two adjacent column centers is parallel to the normal of the face between those water columns, the pressure gradient on such a grid can be discretized in a straightforward manner with a central difference scheme as it is done in Casulli and Walters (2000).

In the non-orthogonal case, a larger stencil is required to calculate the projection of the discretized pressure gradient onto the column side normal, see for example Wenneker et al. (2002); Ham et al. (2005). However, as shown in Ham et al. (2007), a scheme in which the pressure gradient stencil is expanded to cover more surface elevation points, is neither conservative nor uniformly dissipative in any L^2 norm. It is therefore possible the scheme will exhibit growing modes given suitable initial conditions and sufficiently long time integration. Besides that it is not possible to create a Coriolis discretization with the proper skew symmetric properties for a centroid based scheme except on a regular grid where the centroid and circumcenter are at the same location, Ham et al. (2007).

In finite-elements models such as those by Walters and Casulli (2001); Miglio et al. (1999) treatment of the Coriolis term falls out naturally using a standard finite element approximation. Here to compute the Coriolis term the set of basis functions is modified rather than the nodal values. Note also that the reconstruction by Perot (2000) used in a number of finite-difference models

is, in fact, identical to the approximation by a polynomial from the lowest order Raviart-Thomas space. The RT0 scheme by Miglio et al. (1999) uses a circumcentre based approach and results in a scheme similar to Delfin, Ham et al. (2005). The approach requires an orthogonal grid and therefore is subject to the same grid restriction as the finite-difference models. The scheme by Walters and Casulli (2001) has no grid restrictions, but it is slightly less accurate. The finite-element approach of Hanert et al. (2009) also has a simple solution for the Coriolis term, but it results in a full velocity matrix which can be computationally expensive.

Here a new version of the unstructured staggered C-grid model, Delfin, is presented. It was originally developed by Ham et al. (2005) and adopts the mixed finite difference, finite volume, orthogonal C-grid approach by Casulli and Walters (2000). The model is able to accurately simulate Coriolis dominated flows, as well as flooding and drying processes. A proper velocity reconstruction procedure is central to both of these problems. Reconstruction of velocity is also of crucial importance for development of 3D models.

The unstructured finite volume scheme of Casulli and Walters (2000) uses a semi-Lagrangian approach for discretization of the advection term. Originally this approach was also adopted in Delfin, Ham et al. (2005). The main advantage of such a scheme is its stability at any flow Courant number ($Cr = u\frac{\Delta t}{\Delta x}$). However, a Courant number large enough to benefit from the semi-Lagrangian approach may not be attainable since most real life applications have low Cr in the majority of the domain and the CFL constraints ($CFL = \sqrt{gh}\frac{\Delta t}{\Delta x}$) of the discrete continuity equation. Besides that, most implementations of the semi-Lagrangian advection scheme do not provide conservation of momentum which is required for accurate simulation of flooding and drying phenomena. Due to a particular interest in accurately simulating flows in the shallow near shore region, including flooding and drying problems, an Eulerian advection scheme which is guaranteed to be momentum conservative has been chosen. The method developed in Kleptsova et al. (2010) is used, which is a generalization of the advection scheme by Kramer and Stelling (2008) for the multilayer case.

While in the two-dimensional case conservation of momentum is achieved automatically for the Eulerian advection scheme, special attention is required to the discretization of the momentum equation in the presence of multiple $z-$layers. It is common practice to vary only the thickness of the top and bottom layers to represent the free surface and bathymetry variation. The thickness of the internal layers which do not contain the free surface and bed are

kept constant. The heights of the faces for these layers are usually defined to be equal to the heights of the layers, thus replicating the flat bed case. In Kleptsova et al. (2010) it is shown that this can generate a staircase problem which leads to inaccurate solutions and may erroneously introduce vertical structure in the flow, yield stability and conservation problems. To solve this problem a local layer remapping procedure is proposed. The remapping procedure also deals with the case of an uneven number of layers adjacent to a column side, thus allowing one to simulate flooding and drying phenomena in a $z-$layer three-dimensional model. This is particularly useful for simulation of vertical mixing, thermal and density stratification associated with the tidal motion and exchange between inland freshwater systems and coastal seas, as well as studies of sedimentation processes associated with tsunami inundation.

1.1 Structure of the thesis

Chapter 2 introduces the shallow water equations and the core structures of the discretization including the mesh structure and variable placement. Next a general description of the model is given.

In Chapter 3 a spatial discretization of the Coriolis term is considered. A tangential velocity reconstruction procedure for the depth-averaged shallow water equations by Ham et al. (2007) is compared with an unstructured grid variant of the reconstruction by Espelid et al. (2000). Both the schemes are shown to distort the Coriolis term in the case of variable bottom topography, while being theoretically energy conserving. Next a reconstruction which correctly accounts for bathymetry variations is proposed. The velocity reconstruction procedure is further generalized for the multiple layer case.

In Chapter 4 the discretization of the advection term is addressed. The Eulerian advection scheme proposed by Perot (2000) is compared with the scheme by Kramer and Stelling (2008). The latter scheme was shown to give better results for dam break type problems. The scheme by Kramer and Stelling (2008) is generalized for the multilayer case.

Chapter 5 is concerned with the discretization of the momentum equation in the presence of multiple $z-$layers. A layer remapping procedure is proposed to ensure that the staircase representation of bathymetry and free surface has no influence on the vertical structure of the flow.

In Chapter 6 and Chapter 7 Delfin is applied to two real life problems. Chapter 6 presents preliminary results of the unstructured grid fine resolution tidal

model of the southern North Sea, including the Rhine-Scheldt Delta region. It is shown that the model is able to correctly reproduce the essential characteristics of the M2 tide. The simulated velocity field is used to evaluate the Simpson-Hunter stratification criterion.

In Chapter 7 a simulation of 2004 Indian Ocean tsunami is used to evaluate the ability of the method to simulate fast propagating tsunami waves and detailed inundation processes. Results obtained using two different rupture models are compared to the tide gauge arrival times, satellite altimetry data and the inundation observations in the Banda Aceh area. The comparison is used not only to assess the quality of the underlying rupture models, but also to determine the value of the available data sources for such an assessment.

2

General model description

Note. The content of this chapter is based on the the following paper: *Kleptsova et al. (2012), On a momentum conservative z-layer unstructured C-grid ocean model with flooding*

2.1 Equations of motion

Large scale coastal flows may be modeled using the shallow water equations, a well known simplification of the Navier-Stokes equations. To derive the shallow water equation it is assumed that

- Vertical accelerations are small compared with gravity, that is the pressure is considered to be hydrostatic ($\frac{\partial p}{\partial z} = -\rho g$).
- Density differences are considered to be small compared to the reference density ρ_0 and, hence, the density may be assumed to be constant except in the pressure gradient term.

Let $\mathbf{d}$ be any unit vector in the horizontal plane and let $u_{\mathbf{d}} = \mathbf{u} \cdot \mathbf{d}$. Then the shallow water equations may be written as follows:

$$\nabla \cdot \mathbf{u} = 0 \tag{2.1}$$

$$\frac{Du_{\mathbf{d}}}{Dt} = \left(\frac{1}{\rho_0} \nabla_{xy} \int_z^\eta \rho g dz \right) \cdot \mathbf{d} \tag{2.2}$$

$$+\nabla_{xy} \cdot \nu^h \nabla_{xy} u_{\mathbf{d}} + \frac{\partial}{\partial z} \nu^v \frac{\partial u_d}{\partial z} + (2\mathbf{\Omega} \times \mathbf{u}) \cdot \mathbf{d}$$

where $\mathbf{\Omega} = [0, 0, 0.5f]$ is the Earth's rotation vector, ν^h and ν^v are the horizontal and vertical turbulence viscosities. Here

$$\frac{D}{Dt} = \frac{\partial}{\partial t} + \mathbf{u} \cdot \nabla \tag{2.3}$$

is the Lagrangian or material derivative with ∇ being the gradient operator. In the case when a two dimensional field is encountered, a subscript xy is used to indicate the two dimensional gradient operator ∇_{xy}.

The equations (2.1)-(2.2) are to be solved for the velocity $\mathbf{u}$ and the free surface elevation η. The density field is determined by an equation of state $\rho = \rho(S, T)$ in terms of the salinity S and temperature T. The transport equations for temperature and salinity are given by

$$\frac{\partial S}{\partial t} + \nabla \cdot (\mathbf{u}S) = \nabla_{xy}(\gamma^h \nabla_{xy} S) + \frac{\partial}{\partial z}(\gamma^v \frac{\partial S}{\partial z}) \tag{2.4}$$

$$\frac{\partial T}{\partial t} + \nabla \cdot (\mathbf{u}T) = \nabla_{xy}(\kappa^h \nabla_{xy} S) + \frac{\partial}{\partial z}(\kappa^v \frac{\partial T}{\partial z}), \tag{2.5}$$

where the horizontal and vertical turbulent mass and thermal diffusivities are denoted as γ^h, γ^v, κ^h and κ^v respectively.

Currently the effects of density differences are not considered, so the density cancels out of the pressure gradient term. In common with similar models (Casulli and Walters (2000); Baptista et al. (2005)) the horizontal mixing is disregarded. Therefore, the equations actually solved by Delfin are:

$$\nabla \cdot \mathbf{u} = 0 \tag{2.6}$$

$$\frac{\partial u_{\mathbf{d}}}{\partial t} + \mathbf{u} \cdot \nabla u_d + g \nabla_{xy} \eta \cdot \mathbf{d} + \frac{\partial}{\partial z} \nu^v \frac{\partial u_d}{\partial z} - f(\mathbf{u} \cdot \mathbf{d}^{\perp}) = 0 \tag{2.7}$$

where $\mathbf{d}^{\perp}$ is the vector orthogonal to $\mathbf{d}$.

The Equation (2.7) shows that the momentum equation is rotationally invariant and it is possible to solve for horizontal momentum components in any basis vectors directions rather then x and y. The vertical velocity can be obtained from the continuity equation, Equation (2.6).

2.1.1 Kinematic boundary conditions at the free surface and bed

Assuming bottom impermeability, the normal component of the velocity at the sea bed must vanish. Given that the surface elevation η and the bottom height

b are suitably smooth functions of position in the horizontal plane, this can expressed by the following kinematic conditions:

$$\frac{D\eta}{Dt} = \frac{\partial \eta}{\partial t} + \mathbf{u}_{xy} \cdot \nabla_{xy}\eta = w \qquad \text{at } z = \eta \tag{2.8}$$

$$\frac{Db}{Dt} = \mathbf{u}_{xy} \cdot \nabla_{xy} b = w \qquad \text{at } z = b \tag{2.9}$$

Additionally the bed is assumed to be stationary in time.

2.1.2 Bottom stress

The friction with bed is represented with a quadratic dependence on velocity:

$$\nu^v \frac{\partial \mathbf{u}_b}{\partial t} = C_d ||\mathbf{u}_b|| \mathbf{u}_b \tag{2.10}$$

where $\mathbf{u}_b$ is the horizontal fluid velocity at the cell nearest to bed. The dimensionless bottom drag coefficient either specified as a constant or calculated from a given bottom roughness length z_0 as

$$C_d = \left(\frac{\kappa}{\ln\left(\frac{z_b + z_0}{z_0}\right)} \right)^2 \tag{2.11}$$

where z_b is the distance from the bed to the point at which $\mathbf{u}_b$ is computed; $\kappa = 0.4$ is the von Karman constant.

2.1.3 The depth integrated continuity equation

The kinematic boundary conditions (2.9)-(2.8) may be used in combination with the continuity equation integrated over the water column to produce the following expression for the free surface:

$$\frac{\partial \eta}{\partial t} + \frac{\partial}{\partial x}[\int_b^\eta u dz] + \frac{\partial}{\partial y}[\int_b^\eta v dz] = 0 \tag{2.12}$$

To do this the divergence of the velocity is integrated over z using the Leibniz integral rule in its divergence operator form.

2.2 The unstructured grid

In order to achieve accurate results in the coastal region it is important to employ a high resolution grid. Using a grid with a small grid size for a large domain is, however, computationally inefficient. Therefore it is necessary to vary the grid resolution in space to be able to resolve accurately a particular regions of interest while modeling other regions at acceptable cost. Some grid variation is possible using curvilinear structured grids. However by using unstructured grids it is possible to achieve highly variable resolution in complex geometries.

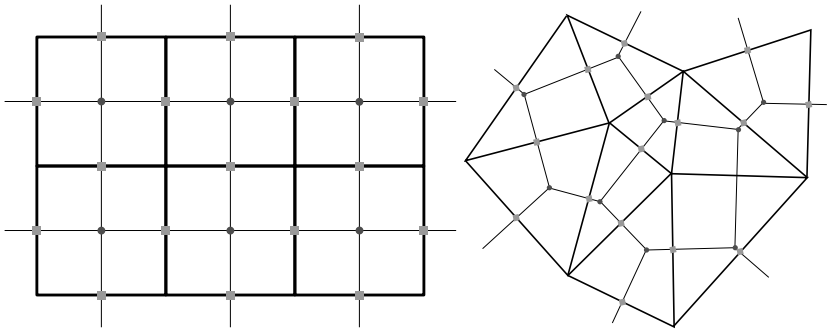

Figure 2.1: Structured (a) and orthogonal unstructured (b) C-grids. The normal fluxes (squares) are calculated at the mid-points of the cell edges and the pressure or elevation points are located at the cell centers (circles).

Here orthogonal unstructured C-grids, as introduced in the paper by Casulli and Walters (2000) are considered. Figure 2.1 shows both a structured C-grid and an orthogonal unstructured C-grid. The similarity between both grids is apparent: within each polygon a point (cell center) is identified in such a way that the segment joining the centers of two adjacent polygons (thin blue lines in Figure 2.1) and the side shared by the two polygons, have a non-empty intersection and are orthogonal to each other. The normal fluxes are calculated at the mid-points of the cell edges and the pressure or elevation points are located at the cell centers. It is worth noting that the cell centers do not necessarily coincide with the polygon geometric centers. For the grids shown in Figure 2.1 the cell centers are equivalent to the centers of the circumscribed circle (circumcenters) which are known to be the point of intersection of the perpendicular bisectors of the sides. However, unless all of the angles in a triangle are acute, its circumcenter will lie outside outside the triangle. Besides

that, a small distance between the circumcenters of the neighboring cells, as in case of the two nearly right angled triangles sharing hypotenuse, can result in an almost infinitely large Courant number.

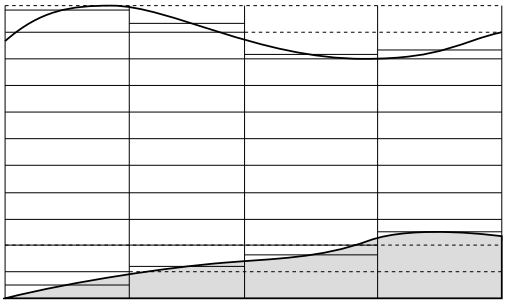

Figure 2.2: Slice through a domain showing the regular grid structure in the vertical and the partial cells at the bed and free surface.

In order to obtain accurate horizontal velocity resolution prismatic elements are used. First a two-dimensional grid is generated for the domain. This grid defines a set of water columns stretching from the free surface down to the bed. Each water column is then divided into a series of cells. This is implemented as a $z-$level scheme, although other vertical discretisations are in principle possible Pietrzak et al. (2002). Figure 2.2 shows a slice through part of a mesh demonstrating the vertical structure.

Figure 2.2 also shows the representation of the bed and free surface. Movement of the free surface may cause the number of $z-$layers in a water column to change resulting in the addition or subtraction of cells at the free surface. At the bed, the exact bathymetry at the water column center is used to specify the bed elevation for the column, which almost always results in a partial cell at the bottom of the water column. This partial cell representation reduces the extent to which a variable bathymetry is represented as a staircase. In this grid structure the scalar and momentum elevation points are aligned vertically. This allows for the efficient evaluation of the pressure gradient term and enables a partial decoupling of the momentum and continuity equations which has advantageous scaling properties.

Notations used to refer to the data associated with water columns and column sides, are summarized in Table 2.1. Definitions of faces require a little explanation. The column side f shown in Figure 2.3 has two adjacent columns c_L and c_R with water depths h_L and h_R and respectively. Bottom height of the column side is defined as maximum (shallowest) of the adjacent columns bottom heights, that is $b_f = b_R$ in our case. Surface elevation on the column

Table 2.1: Notation for data associated with water columns and column sides.

k	Vertical level. The layer of a horizontal face above above level k is $k+\frac{1}{2}$ and the layer below is $k-\frac{1}{2}$
z_k	Height (altitude) of the vertical level k
A_c	Cell or water column cross section area
A_f	Column side area
$A_{f,k}$	Cell face area
l_f	Length of the edge
$\mathbf{n}_f$	Cell face or column side normal vector
$\mathbf{N}_{f,c}$	Normal vector at side f which points outward relative to the adjacent column c
d_f	Orthogonal distance between cirumcenters of the columns sharing the side f
$d_{f,c}$	Orthogonal distance between the side f and the column c circumcenters
$\delta_{f,c}$	Function defined for each side f and column c such that $\delta_{f,c} = \begin{cases} 1 \text{ if column } c \text{ contains side } f \\ 0 \text{ otherwise} \end{cases}$
$s_{f,c}$	Function defined for each side f and column c such that $s_{f,c} = \delta_{f,c}(\mathbf{n}_f \cdot \mathbf{N}_{f,c}) = \begin{cases} 1 & \text{if } f \in c \text{ and } \mathbf{n}_f \text{ points outward} \\ -1 & \text{if } f \in c \text{ and } \mathbf{n}_f \text{ points inward} \\ 0 & \text{if cell } c \text{ does not contain face } f \end{cases}$
b_*	Bed height. The bed height b_f at the face f is defined as the shallowest of the adjacent columns bed heights. That is $b_f = max(b_{c_1}, b_{c_2})$
η_*	Free surface height. The free surface height η_f at the side f is defined as the upwind water level.
h_*	Water depth. $h_* = \eta_* - b_*$
$\mathbf{u}_{c,k}$	Velocity vector at the circumcenter of the cell c
$\mathbf{u}_{f,k}$	Velocity vector at the center of the face f
$u_{f,k}$	Component of the $\mathbf{u}_{f,k}$ vector in the normal direction $\mathbf{n}_f$
$\mathbf{u}_{c,k\pm\frac{1}{2}}$	Velocity vector at the center of the top $(+)$ and bottom $(-)$ face centers of the cell c_k
$u_{c,k\pm\frac{1}{2}}$	Component of the $\mathbf{u}_{c,k\pm\frac{1}{2}}$ vector in the direction normal to the top $(+)$ and bottom $(-)$ faces of the cell c_k. The normal is assumed to point in the positive z direction.

An asterisk is a wildcard for a member of {f,c}. For temporally variable data, time step will be indicated with a superscript.

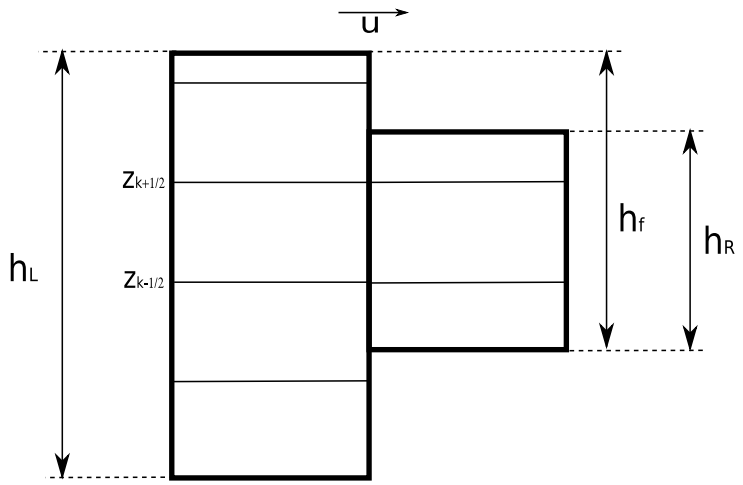

Figure 2.3: Face height definitions.

side is taken to be the value in the upwind column, that is $\eta_f = \eta_L$ in the case shown in 2.3

As can be seen from Figure 2.3 the column side has adjacent cells located at five vertical levels, therefore five faces at the column side are defined. Heights of the faces need to be defined in such a way that their sum is equal to the height of the column side, that is

$$\sum_k h_{f,k} = h_f \tag{2.13}$$

Heights of the cells adjacent to the column side satisfy the following equality

$$\sum_k \max(h_{L,k}, h_{R,k}) = \max(\eta_L, \eta_R) - \min(b_L, b_R), \tag{2.14}$$

where heights of the undefined cells in the right column are set to zero. Therefore, height of the face f on vertical level k can be defined as

$$h_{f,k} = \frac{h_f * \max(h_{L,k}, h_{R,k})}{\max(\eta_L, \eta_R) - \min(b_L, b_R)} \tag{2.15}$$

2.3 Discretisation of the equations

The continuity equation is discretized using a finite volume scheme with a single triangle as the control volume, while the pressure gradient term is discretized using a form of finite difference scheme.

A semi-implicit $\theta-$scheme as the temporal discretisation of the free surface equation is chosen. The momentum equation is solved for the velocity component normal to each cell face. The advection and Coriolis operators are dealt with explicitly relative to the pressure term. For the time evolution of the pressure gradient, the same $\theta-$method chosen for the free surface equation is adopted. The vertical viscosity term is discretized in space in a straightforward central differencing manner and in time using a fully implicit backward Euler scheme. A detailed description of the model can be found in Ham et al. (2005).

Thus the following set of discrete equations is obtained:

$$A_c\eta_c^{n+1} = A_c\eta_c^n - \theta\Delta t\sum_f \left(s_{f,c}l_f\sum_k h_{f,k}^n u_{f,k}^{n+1}\right) -$$

$$(1-\theta)\Delta t\sum_f \left(s_{f,c}l_f\sum_k h_{f,k}^n u_{f,k}^n\right)$$

$$u_{f,k}^{n+1} = u_{f,k}^n + \Delta t a_{f,k}^n + F(\mathbf{u})_{f,k}^n - g\Delta t(\theta G_f^{n+1} + (1-\theta)G_f^n) + \tag{2.16}$$

$$\frac{\Delta t}{\Delta z_{f,k}^n}\left(\nu^v_{f,k+\frac{1}{2}}\frac{u_{f,k+1}^{n+1}-u_{f,k}^{n+1}}{\Delta z^n_{f,k+\frac{1}{2}}} - \nu^v_{f,k-\frac{1}{2}}\frac{u_{f,k}^{n+1}-u_{f,k-1}^{n+1}}{\Delta z^n_{f,k-\frac{1}{2}}}\right)$$

The equations for the top and bottom layers may have additional terms inserted to account for wind stress and bottom friction. The operators a and F are explicit operators which account for the contribution from the discretisation of advection and the Coriolis terms respectively, discussed in Chapter 3 and 4.

2.3.1 Pressure gradient term

On an orthogonal grid the interval joining two adjacent column centers is parallel to the normal of the face between those water columns. Therefore the pressure gradient term can be discretized in with a central difference scheme. The linear operator G for pressure gradient term is defined as:

$$G_f = s_{f,c_1}\frac{\eta_{c_1}-\eta_{c_2}}{d_f}, \tag{2.17}$$

with c_1 and c_2 being the two cells sharing the face f.

2.3.2 Flooding and drying

To implement flooding and drying it is a common practice to mask a column c as dry if its water depth h_c becomes less than a threshold value. Following Stelling and Duinmeijer (2003) water surface elevation η_f at a column side f is defined using the first-order upwinding as following

$$\eta_f = \begin{cases} \eta_{c_1} \text{ if } s_{f,c_1} u_f > 0 \\ \eta_{c_2} \text{ if } s_{f,c_2} u_f < 0 \\ \max(\eta_{c_1}, \eta_{c_2}) \text{ if } u_f = 0 \end{cases} \tag{2.18}$$

The column side f is then masked as dry and the velocity u_f at the column side is set to zero ones the water depth $h_f = \eta_f - b_f$ becomes less than a prescribed threshold value h_{min}. Thus the water depth used to calculate outgoing fluxes of a column c is that of the column itself. Therefore, there will nether be a flux out of a dry column. Stelling and Duinmeijer (2003) show that non-negative water depth is ensured if:

$$\frac{\Delta t u_f^n}{\Delta x} \leq 1 \tag{2.19}$$

This condition is the same as the CFL condition, and, thus, poses no additional restriction on the time step.

2.3.3 Solution algorithm and matrix structure

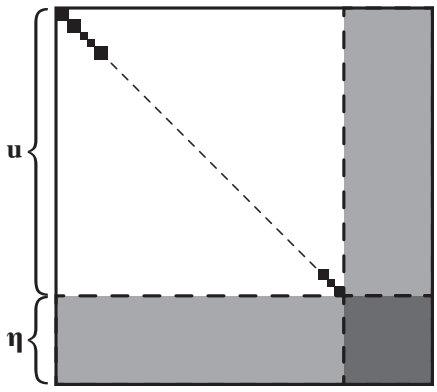

Figure 2.4: The matrix structure of the discrete system. The form of the velocity submatrix (upper left submatrix) allows the velocity variables to be eliminated from the free surface equation.

The choice of explicit and implicit terms (Casulli and Walters (2000)) results in the advantageous matrix structure. If a numbering m of the velocity unknowns is chosen so that $m(f, k+1) = m(f, k) + 1$ then the matrix has the form shown in Figure 2.4 The upper left quarter of the matrix is block diagonal and is made up purely of the tridiagonal mass matrices. These matrices can be inverted using fast direct methods.

The block diagonal structure of the velocity submatrix results directly from the explicit treatment of the advection and Coriolis terms.

3

Treatment of the Coriolis term on a C-grid discretisation

Note. The content of this chapter is based on the the following papers: *Kleptsova et al. (2009), On the accurate and stable reconstruction of tangential velocities in C-grid ocean models*.

The accurate propagation of inertia-gravity waves is an important issue in any numerical model of large scale geostrophic flows. However, in developing discretisations suitable for modeling such flows, the possibility of generating spurious pressure or velocity modes is always an important consideration. Arakawa and Lamb (1977) analyzed the representation of inertia–gravity waves on different grids and showed that C-grid models yield the most accurate numerical solutions if the Rossby radius is well resolved. If, however, the radius of deformation is coarsely resolved the C-grid models demonstrate intolerable level of gridscale noise, existence of which is caused by the discretization of the Coriolis force.

Both the structured and unstructured C-grid based models solve for the cell normal velocities, whereas the tangential velocity required in the calculation of the Coriolis term $F(\mathbf{u})$ is interpolated from the surrounding cell normal values. In the case of a structured C-grid shown in Figure 3.1 four neighboring values are typically employed in the averaging procedure

$$F(\mathbf{u})_{i,j-\frac{1}{2}} = f v_{i,j-\frac{1}{2}}, \quad F(\mathbf{u})_{i+\frac{1}{2},j} = -f u_{i+\frac{1}{2},j}$$

$$v_{i,j-\frac{1}{2}} = \frac{1}{4}(v_{i-\frac{1}{2},j} + v_{i+\frac{1}{2},j} + v_{i-\frac{1}{2},j-1} + v_{i+\frac{1}{2},j-1}) \tag{3.1}$$

$$u_{i+\frac{1}{2},j} = \frac{1}{4}(u_{i,j-\frac{1}{2}} + u_{i,j+\frac{1}{2}} + u_{i+1,j+\frac{1}{2}} + u_{i+1,j-\frac{1}{2}})$$

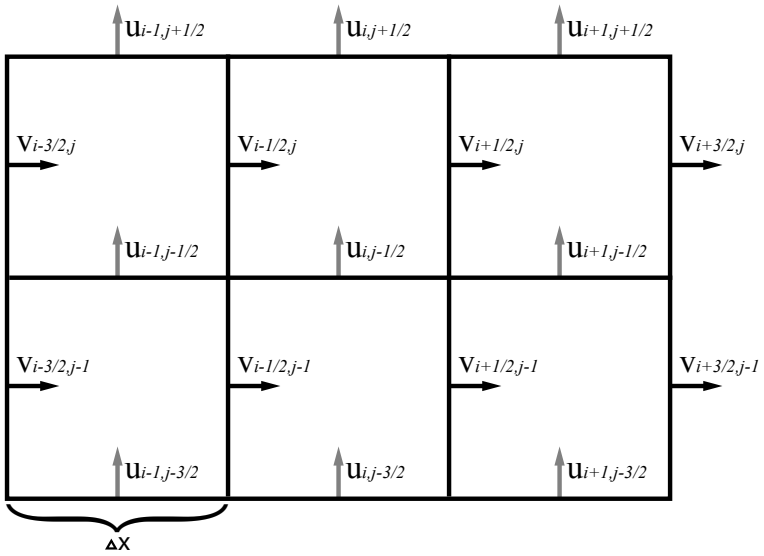

Figure 3.1: Structured grid velocity variable placement.

As shown by Espelid et al. (2000) this simple averaging procedure can lead to instability in the case of variable bathymetry.

Espelid et al. (2000) studied the linear inertia-gravity wave equations and considered the eigenvalues of the propagation matrices of the semi-discrete (in space) partial differential equations:

$$\frac{d}{dt}\begin{bmatrix}\mathbf{u}\\ \eta\end{bmatrix} = A\begin{bmatrix}\mathbf{u}\\ \eta\end{bmatrix} = \begin{bmatrix}F & P\\ C & 0\end{bmatrix}\begin{bmatrix}\mathbf{u}\\ \eta\end{bmatrix} \tag{3.2}$$

In the case of hyperbolic problems one should only have imaginary eigenvalues, Strang (1988). This property is shared by skew-symmetric matrices ($A^T = -A$) or matrices similar to skew-symmetric, that is matrices such that $D^{-1}AD$ is skew-symmetric for some diagonal matrix D. For a structured grid the system matrix (3.2) is similar to skew-symmetric in the absence of Coriolis or bathymetry variations.

Consequently Espelid et al. (2000) demonstrated that it is possible to derive a proper weighting of the Coriolis term which ensures skew-symmetry of the tangential velocity interpolation matrix as well as the system matrix. This allows us to derive a stable method which conserves energy both locally and globally.

However, in the case of orthogonal unstructured C-grids, Figure 3.2, the tangent velocity interpolation is not an obvious task. A number of reconstructions of a vector from its components are found in literature, see Bonaventura and Ringler (2005); Shashkov et al. (1998); Perot (2000). These procedures assume a piecewise linear velocity field and, thus, are all equivalent to the approximation by a polynomial from the zero order Raviart-Thomas space, see Perot et al. (2006). The distinctive feature of the Perot (2000) approach is that it does not require any a priory knowledge of the polygon type used in the grid. It allows for mixed grids consisting of any cyclic polygons as used in Casulli and Walters (2000) type models and, thus, appear somewhat more general in this respect. The reconstruction procedure can be written in a very compact form which allows for a much simpler analysis.

3.1 Tangential velocity interpolation in 2D case

As a starting point adopt a velocity reconstruction presented by Perot (2000), who considered energy conservative discretisations of the 2D Navier-Stokes equations, in the case of non-rotating flows, with constant depth. The interpolation can be considered as a two stage process: first the full velocity vector $\mathbf{u}_c$ in the cell interior is reconstructed out of the normal velocity components u_f of the cell faces. The velocity vector $\mathbf{u}_f$ at the face center is approximated as a linear combination of the two neighboring cell velocity vectors $\mathbf{u}_c$, see Figure 3.2. Then this reconstructed full velocity vector is projected back to the cell faces tangent direction.

For the 2D case the reconstruction by Perot (2000) can be expressed using the position of the circumcenter as follows:

$$\mathbf{u}_c = \sum_f \delta_{f,c} d_{f,c} \frac{l_f}{A_c} u_f \mathbf{n}_f \tag{3.3}$$

$$\mathbf{u}_f = \sum_c \delta_{f,c} \frac{d_{f,c}}{d_f} \mathbf{u}_c \tag{3.4}$$

In order to obtain an energy balance, one multiplies the velocity equation with $l_f d_f u_f h_f$ and sums over the edges. Here h_f is the water depth at the face f (it should be consistent with the way in which the continuity equation is solved). This implies that

$$\sum_f l_f d_f h_f u_f (\mathbf{u}_f \cdot \mathbf{t}_f) \tag{3.5}$$

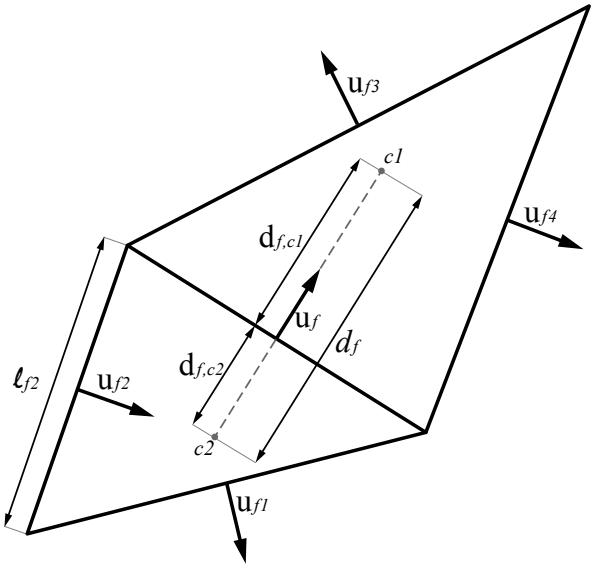

Figure 3.2: Unstructured grid velocity variable placement and grid notations.

should be zero. The unit face tangent vector $\mathbf{t}_f$ is defined in such a way that $\mathbf{n}_f \times \mathbf{t}_f = 1$.

However, in the case of variable bottom topography the original 2D Perot reconstruction (3.3)-(3.4) fails to ensure no energy production due to the Coriolis term. There are two easy ways to modify the 2D Perot reconstruction.

The first way is straightforward and is proposed by Ham et al. (2007). Leave Equation (3.3) as it is, but modify Equation (3.4) as follows

$$\mathbf{u}_c = \sum_f \delta_{f,c} d_{f,c} \frac{l_f}{A_c} u_f \mathbf{n}_f \tag{3.6}$$

$$\mathbf{u}_f = \sum_c \delta_{f,c} \frac{d_{f,c}}{d_f} \frac{h_c}{h_f} \mathbf{u}_c \tag{3.7}$$

Here the velocities are additionally weighted with depth, with h_c being the depth at the cell circumcenter. This is referred to as Method 1 hereafter.

The second method that presented here is, in fact, a generalization of the method proposed by Espelid et al. (2000) for structured C-grids. This is referred to as Method 2. The essence is to modify both steps of the Perot recon-

struction in a symmetric way:

$$\mathbf{u}_c = \sum_f \delta_{f,c} d_{f,c} \frac{l_f \sqrt{h_f}}{A_c \sqrt{h_c}} u_f \mathbf{n}_f \tag{3.8}$$

$$\mathbf{u}_f = \sum_c \delta_{f,c} \frac{d_{f,c}}{d_f} \frac{\sqrt{h_c}}{\sqrt{h_f}} \mathbf{u}_c \tag{3.9}$$

It is worth noting that the new method proposed here, Method 2, is not the same as the tangential velocity interpolation for unstructured C-grids presented in Espelid and Berntsen (2007). In Kleptsova et al. (2009) it is shown that their velocity interpolation does not fulfill a very basic consistency requirement.

If one revisits, the original Perot reconstruction (3.3) is derived for the Navier-Stokes equations and is essentially based on the following variant of Gauss' Divergence Theorem (see Perot (2000), Section 5.4 for details):

$$\int_\Omega \omega dV + \int_\Omega \mathbf{r}(\nabla \cdot \omega) dV = \int_{\partial\Omega} (\omega \cdot \mathbf{N}) \mathbf{r} dA \tag{3.10}$$

The equation (3.10) is exact for any volume Ω with piecewise smooth boundary $\partial\Omega$, any continuously differentiable vector field ω and a position vector $\mathbf{r} = \mathbf{x} - \mathbf{x_0}$ with an arbitrary origin $\mathbf{x_0}$. Here $\mathbf{N}$ is the outward pointing unit normal field of the boundary $\partial\Omega$.

To derive the cell velocity interpolation Equation (3.3) the identity (3.10) is used under the assumption that $\nabla \cdot \omega = 0$ which is nothing else than the continuity equation for the full velocity vector. However, it is neither valid for the depth averaged velocity $\bar{\mathbf{u}}$ nor for $\sqrt{h}\bar{\mathbf{u}}$ field. For that reason, both the reconstructions (3.6)-(3.7) and (3.8)-(3.9) will distort the Coriolis term even though they preserve skew-symmetry.

In the following section a method which improves the accuracy of the tangential velocity interpolation is presented. The method is generally applicable for grids consisting of cyclic polygons.

3.1.1 Depth integrated method

Our aim is to improve the accuracy of the tangential velocity interpolation to minimize the distortion of the Coriolis term. In order to do this the identity (3.10) needs to be rewritten in a way that takes into account the depth integrated continuity equation (2.12).

The cell is assumed to be a prism with a polygon base Ω^2. Integrating the identity (3.10) over the vertical and using the kinematic boundary conditions one obtains:

$$\int_{\Omega^2} (h\bar{\mathbf{u}})\, dA = \int_{\partial\Omega^2} \mathbf{r}(h\bar{\mathbf{u}} \cdot \mathbf{n}) dl + \frac{\partial}{\partial t} \int_{\Omega^2} \mathbf{r}\eta\, dA \tag{3.11}$$

Further, local coordinates with the origin in the cell circumcenter are chosen.

$$h_c \mathbf{u}_c A_c = \sum_f (h_f \mathbf{u}_f \cdot \mathbf{N}_{f,c}) l_f \mathbf{r}_f + \frac{\partial \eta_c}{\partial t} A_c \mathbf{r}_c \tag{3.12}$$

where $\mathbf{r}_f$ and $\mathbf{r}_c$ are the vectors pointing to the face and cell centers respectively.

Since

$$\mathbf{r}_f = \mathbf{x}_f - \mathbf{x}_c = s_{f,c} d_{f,c} \mathbf{n}_f \tag{3.13}$$

and

$$\mathbf{u}_f \cdot \mathbf{N}_{f,c} = s_{f,c} u_f \tag{3.14}$$

one arrives at the following velocity reconstruction procedure, referred to as Method 3 hereafter:

$$\mathbf{u}_c = \sum_f \delta_{f,c} d_{f,c} \frac{l_f}{A_c} \frac{h_f}{h_c} u_f \mathbf{n}_f \tag{3.15}$$

$$\mathbf{u}_f = \sum_c \delta_{f,c} \frac{d_{f,c}}{d_f} \mathbf{u}_c \tag{3.16}$$

Taking the Coriolis energy production sum one can write

$$\sum_f l_f d_f h_f u_f v_f = \sum_c \frac{1}{A_c h_c} \sum_f \sum_{f'} \delta_{f,c} l_f u_f h_f \cdot \delta_{f',c} l_{f'} u_{f'} h_{f'} (\mathbf{n}_{f'} \cdot \mathbf{t}_f) =$$

$$= \sum_c \frac{1}{A_c h_c} \sum_f \sum_{f'<f} \delta_{f,c} l_f u_f h_f \cdot \delta_{f',c} l_{f'} u_{f'} h_{f'} (\mathbf{n}_{f'} \cdot \mathbf{t}_f + \mathbf{n}_f \cdot \mathbf{t}_{f'}) = 0.$$

The result is zero for the same reason as for the original Perot reconstruction: if $f = f'$, the vectors $\mathbf{n}$ and $\mathbf{t}$ are orthogonal; in other cases the result is anti-symmetric since $(\mathbf{n}_{f'} \cdot \mathbf{t}_f) = -(\mathbf{n}_f \cdot \mathbf{t}_{f'})$

It is important to note that the identity (3.10) is valid for any cyclic polygon, thus the tangential velocity interpolation procedure (3.15)-(3.16) may also be

used for Cartesian grids. Indeed, for the rectangular grid shown in Figure 3.1 the reconstruction procedure (3.15)-(3.16) reduces to

$$v_{i,j-\frac{1}{2}} = \frac{1}{4}\left[\frac{h_{i-\frac{1}{2},j}}{h_{i,j}}v_{i-\frac{1}{2},j} + \frac{h_{i+\frac{1}{2},j}}{h_{i,j}}v_{i+\frac{1}{2},j} + \frac{h_{i-\frac{1}{2},j-1}}{h_{i,j-1}}v_{i-\frac{1}{2},j-1} + \frac{h_{i+\frac{1}{2},j-1}}{h_{i,j-1}}v_{i+\frac{1}{2},j-1}\right] \tag{3.17}$$

Note that in equation (3.17) u denotes the velocity component in x direction, not the velocity component normal to a face.

3.2 Test cases

A number of test cases have been included to highlight the differences arising from the choice of spatial interpolation.

3.2.1 Kelvin wave test case

The first test case is the flat bed test case described in Ham et al. (2005) and used to compare the skew symmetric interpolation with one violating this condition. Here it is used to compare the velocity interpolation procedures (3.6)-(3.16) in the flat bottom case. The initial state chosen was (see Figure 3.3):

$$\begin{aligned} \eta(r,\theta) &= 0.05e^{(r-r_0)/L_D}\cos\theta \\ u_\theta(r,\theta) &= 0.05\sqrt{g/h}e^{(r-r_0)/L_D}\cos\theta \\ u_r(r,\theta) &= 0 \end{aligned} \tag{3.18}$$

where L_D is the Rossby radius, in this case approximately $68km$, and $r_0 = 250km$ is the basin radius. The basin was given a uniform depth of $5m$. Figure 3.4 shows the grid used.

The shallow water equations with friction and advection terms disregarded (2.16) were solved using all of the velocity interpolation procedures (3.6)-(3.16) described above.

The simulations were conducted at a specified latitude of $45°$ North with θ in (2.16) set to 0.5. Time step of 20 minutes was chosen. All of the simulations were found to be stable and energy conserving for more than 10 years. The time evolution of the total system energy is shown in Figure 3.5

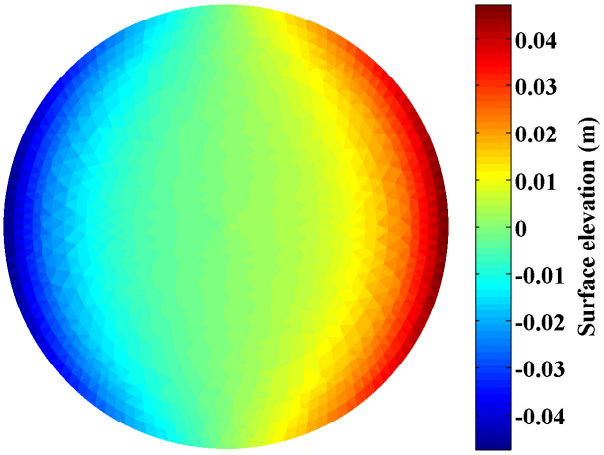

Figure 3.3: The initial surface elevation for the Kelvin wave test case.

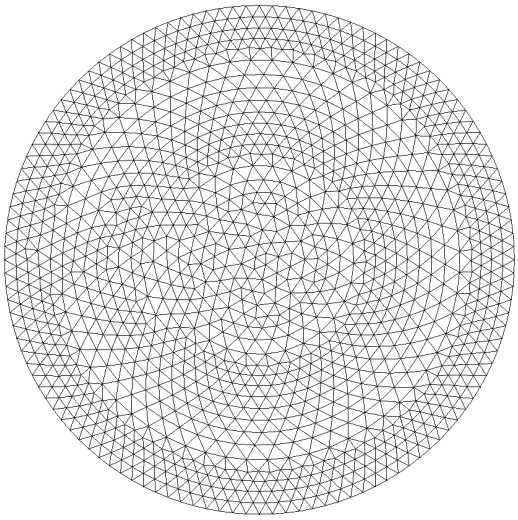

Figure 3.4: The mesh used for the Kelvin wave test case. The basin radius is $250km$ and the nominal triangle edge length is $14km$.

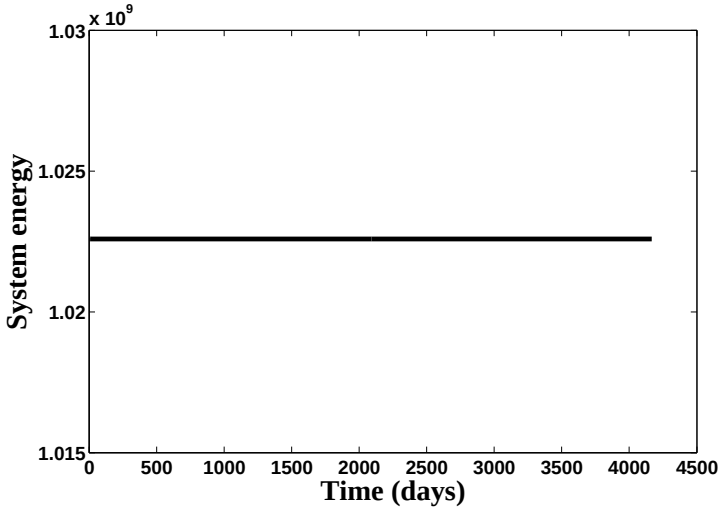

Figure 3.5: Time evolution (days) of total system energy for Kelvin wave in a circular basin with uniform depth of $5m$. Water depth in continuity equation is constant in time.

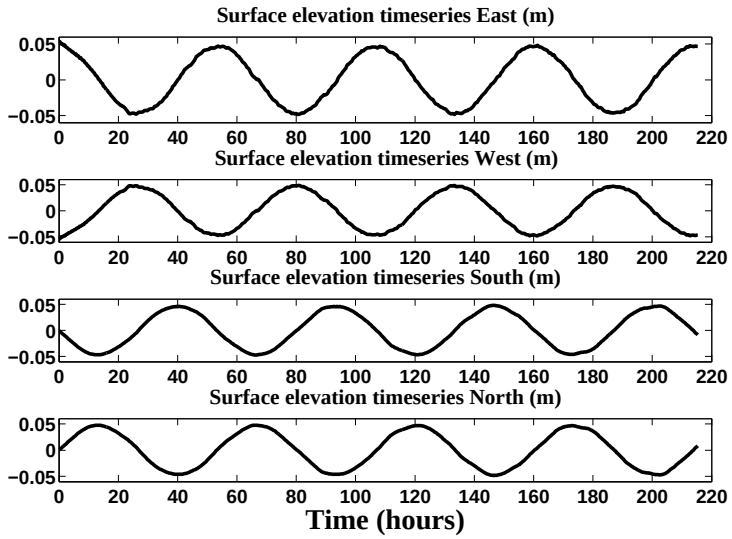

Figure 3.6: The surface elevation time series for Kelvin wave in a circular basin with uniform depth of $5m$.

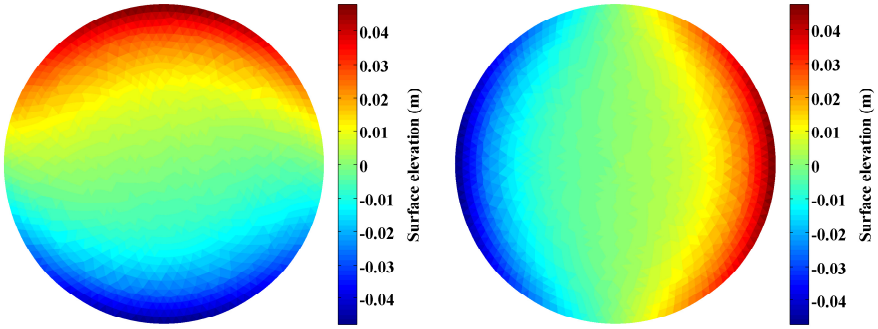

Figure 3.7: Sea surface elevation after 600 (left) and after 1666,6 (right) hours.

As expected all the described tangential velocity reconstruction methods give identical results in the flat bottom case. The surface elevation time series of the first few rotations for the extreme East, West, North and South points of the domain are shown in Figure 3.6. Snapshots of the sea level are shown in Figure 3.7.

3.2.2 Coriolis tilt test case

Consider a simple test case referred to as the Tilting experiment, for which an exact geostrophic balance between the Coriolis force and the pressure gradient should be maintained. It has a simple analytic solution. Figure 3.8 shows the spatial domain and grid used. The bottom profile is constant in the x direction and has a cosinusoidal bottom profile in the y direction, see Figure 3.9. The length of the domain in the x-direction is $500km$ and the width in the y-direction is $300km$. The grid used has a total of 2970 triangles. At inflow a constant velocity of $u = 0.1$ m/s is given. This gives a Rossby number of 0.002. At outflow a linearized Riemann invariant is given by:

$$u - \sqrt{\frac{g}{h}}\eta = 0.1 + \sqrt{\frac{g}{h}}\frac{fy}{g}0.1 \; (ms^{-1})$$

Therefore the steady state solution is given by

$$u(x,y) = 0.1 \; (ms^{-1}), \; v(x,y) = 0 \; (ms^{-1}), \; \eta(x,y) = -\frac{fy}{g}u \; (m) \quad (3.19)$$

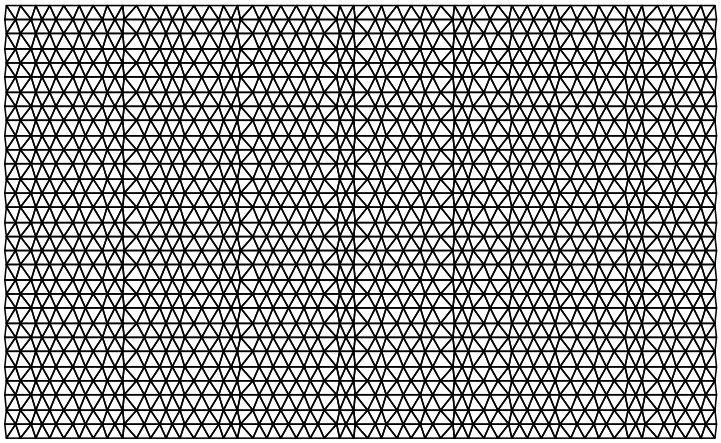

Figure 3.8: The mesh used for the Coriolis tilting test case.

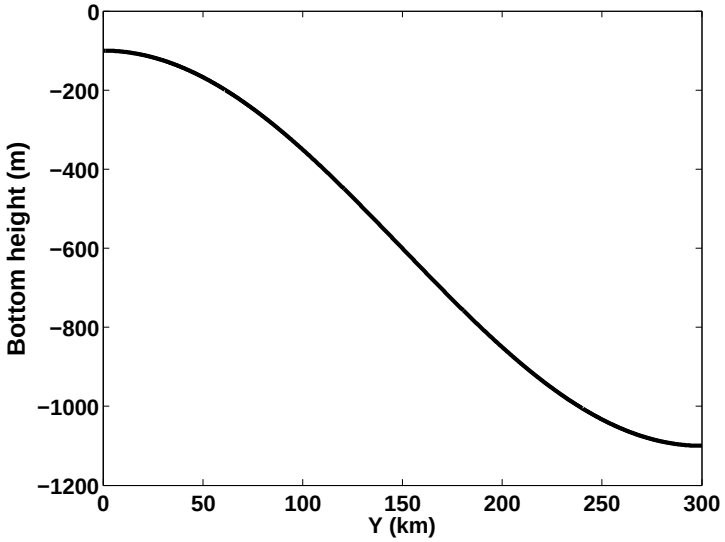

Figure 3.9: The bathymetry profile used for the Coriolis tilting test case.

The initial state chosen was $\eta = 0$ and $u = 0$ everywhere except boundaries. These initial conditions allow us to assess the ability of the model to reproduce the geostrophic adjustment process.

The simulations were performed at a specified latitude 45° North. Here $\theta = 0.5$ and a time step of 30 seconds was chosen. After all the methods have reached the steady state as a result of the transient wave propapation out of open boundaries, the surface elevation and velocities computed using different velocity reconstruction procedures were compared to the analytical solution (3.19). As before the methods given by (3.6) - (3.16) are referred as Method 1, Method 2 and Method 3. The surface elevation computed using the Method 3, as the tangential velocity reconstruction procedure, is shown in Figure 3.10.

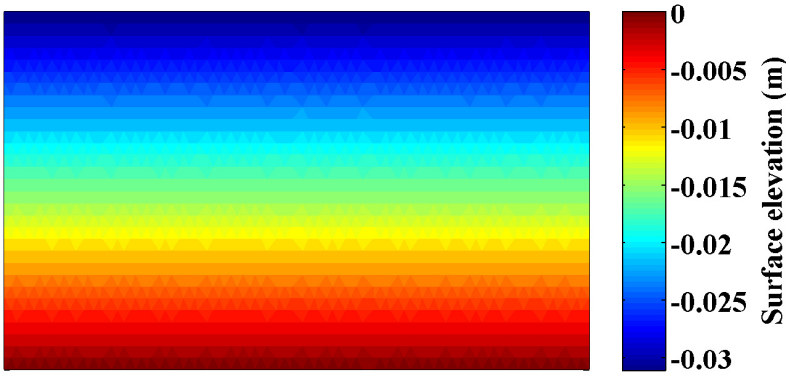

Figure 3.10: The numerical solution for the water levels obtained using the tangential velocity interpolation method (3.15)-(3.16).

As can be seen from Figure 3.11 Method 3 has the best agreement with the analytical solution in the shallowest part of the domain, whereas in the deep part of the channel all of the methods are in the good agreement. However, the difference between the methods becomes apparent if one compares the velocity norm averaged across the domain shown in Figure 3.12. The velocity norm of the Method 3 remained constant up to visible precision for the entire duration of the simulation, about 1500 days. Whereas the Methods 1 and 2 demonstrate a considerable increase in the velocity norm. Similar behaviour of the system kinetic energy is observed.

The tilting test case shows us that while a number of choices for the weighting in the case of variable bathymetry can be made, the optimal one appears to be

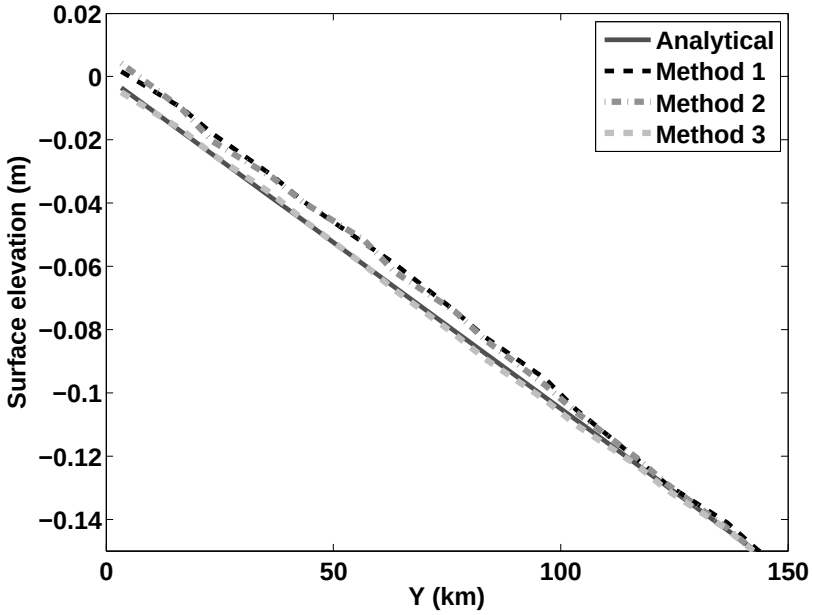

Figure 3.11: Part of computed surface elevation in the cross channel direction compared to the analytical solution.

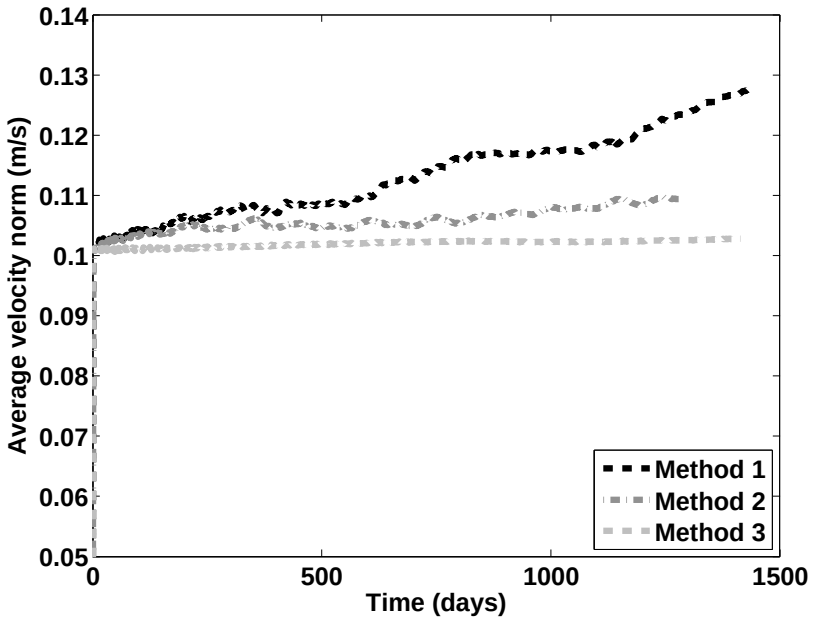

Figure 3.12: The time evolution of average velocity norm.

the Method 3, (Equation (3.15)-(3.16)).

3.3 Tangential velocity interpolation in 3D case

In the previous sections the velocity reconstruction for the depth integrated continuity equation is considered. Here the velocity reconstruction in the multiple layer case is considered.

Once again start with the following variant of Gauss' Divergence Theorem (see Perot (2000), Section 5.4 for details):

$$\int_{\Omega} \omega dV + \int_{\Omega} \mathbf{r}(\nabla \cdot \omega) dV = \int_{\partial\Omega_f} (\omega \cdot \mathbf{N}) \mathbf{r} dA \tag{3.20}$$

The equation (3.20) is exact for any volume Ω with piecewise smooth boundary $\partial\Omega$, any continuously differentiable vector field ω and a position vector $\mathbf{r} = \mathbf{x} - \mathbf{x_0}$ with an arbitrary origin $\mathbf{x_0}$. Here $\mathbf{N}$ is the outward pointing unit normal field of the boundary $\partial\Omega$.

Thus using the mean value theorem and noting that

$$(\mathbf{u}_{f,k} \cdot \mathbf{N}_{f,c}) = s_{f,c} u_{f,k} \quad \text{and} \quad (\mathbf{u}_{c,k\pm\frac{1}{2}} \cdot \mathbf{N}_{c,k\pm\frac{1}{2}}) = \pm u_{c,k\pm\frac{1}{2}} \tag{3.21}$$

the velocity vector in the interior of a prismatic cell can be interpolated as

$$\begin{aligned} V_{c,k} \mathbf{u}_{c,k} &= \sum_{f_k} s_{f,c} A_{f,k} u_{f,k} \mathbf{r}_{f,k} + \\ &+ A_c \left(u_{c,k+\frac{1}{2}} \mathbf{r}_{c,k+\frac{1}{2}} - u_{c,k-\frac{1}{2}} \mathbf{r}_{c,k-\frac{1}{2}} \right) \end{aligned} \tag{3.22}$$

Here the first summation in the right hand side goes over the vertical faces of the cell, the second summation refers to the contribution from the top and bottom faces of the cell. The vectors $\mathbf{r}_{f,k}$ and $\mathbf{r}_{c,i}$ with $i = \{k \pm \frac{1}{2}\}$ are the vectors pointing to the respective face centers. The origin of the position vector is allowed to be the cell center.

As before the velocity vector at the face is approximated as the following linear combination of the two neighboring cell velocity vectors.

$$\mathbf{u}_{f,k} = \sum_{c} \delta_{f,c} \frac{d_{f,c}}{d_f} \mathbf{u}_{c,k} \tag{3.23}$$

Tangent velocity component is then obtained by projecting the velocity vector $\mathbf{u}_{f,k}$ in the direction $\mathbf{t}_f$. That is

$$(\mathbf{u}_{f,k} \cdot \mathbf{t}_f) = \sum_{c_k} \delta_{f,c} \frac{d_{f,c}}{d_f} \left[\sum_{f'_k} s_{f',c} \frac{A_{f',k}}{V_{c,k}} u_{f',k} (\mathbf{r}_{f',k} \cdot \mathbf{t}_f) + \right. \\ \left. + \frac{A_c}{V_{c,k}} \left(u_{c,k+\frac{1}{2}} (\mathbf{r}_{c,k+\frac{1}{2}} \cdot \mathbf{t}_f) - u_{c,k-\frac{1}{2}} (\mathbf{r}_{c,k-\frac{1}{2}} \cdot \mathbf{t}_f) \right) \right] \tag{3.24}$$

Note, that vectors $\mathbf{t}_f$ tangential to the vertical face of the grid are assumed to lie in the horizontal plane.

The centers of the vertical rectangular faces are located at the intersection of diagonals. This point is both the geometric center (centroid) of the rectangle and the center of the circumscribed circle (circumcenter). There are however several possibilities for placement of the "horizontal" faces and cell centers:

- Face centers are located in the respective centroids, cell center is located half way between the centroids of the top and bottom faces, Figure 3.13.

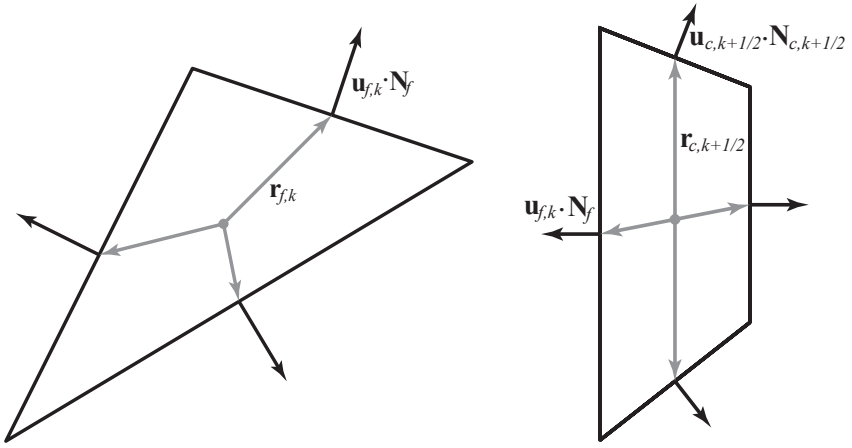

Figure 3.13: Cell and face centers placement: Face center is located in the respective centroid (left), cell center is located half way between the centers of the top and bottom faces (right).

In this case the dot product $(\mathbf{r}_{f,k} \cdot \mathbf{t}_f)$ is not equal to zero, that is the velocity component normal to a face contributes to the tangential velocity

component of that face. Thus the skew-symmetry of the system matrix is not preserved and the numerical scheme will become unstable due to the Coriolis term.

- Face centers are located in the face circumcenters, cell center is located half way between the circumcenters of the top and bottom faces. Circumcenters are assumed to lie inside of the face.

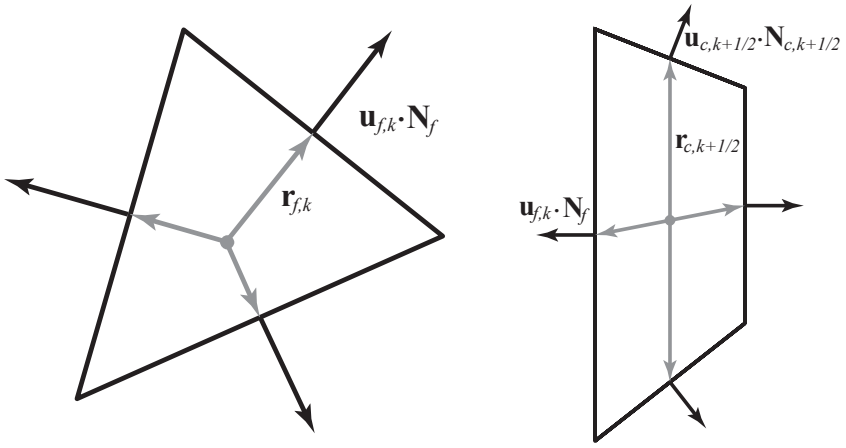

Figure 3.14: Cell and face centers placement: Face center is located in the respective circumcenter (left), cell center is located half way between the circumcenters of the top and bottom faces (right).

In this case the vectors $\mathbf{r}_{f,k}$ and $\mathbf{r}_{c,k\pm1/2}$ pointing from the cell center to the centers of the cell faces can be written as

$$\begin{aligned} \mathbf{r}_{f,k} &= s_{f,c} d_{f,c} \mathbf{n}_f + \frac{h_{f,k} - h_{c,k}}{2}\mathbf{z} \\ \mathbf{r}_{c,k\pm\frac{1}{2}} &= \pm\frac{h_{c,k}}{2}\mathbf{z} \end{aligned} \tag{3.25}$$

where $\mathbf{z} = [0, 0, 1]$ is a unit vector pointing in the positive $z-$axis direction.

Since the vectors $\mathbf{r}_{c,k\pm1/2}$ are strictly vertical, velocity normal to the top and bottom faces of a cell (whose horizontal components are generally not zero) does not contribute to the horizontal components $\mathbf{u}^{xy}_{c,k}$ of the

cell velocity vector $\mathbf{u}_{c,k}$. That is with the above definitions $\mathbf{u}^{xy}_{c,k}$ can be written as

$$\mathbf{u}^{xy}_{c,k} = \sum_{f_k} \delta_{f,c} d_{f,c} \frac{h_{f,k} l_f}{h_{c,k} A_c} u_{f,k} \mathbf{n}_f \tag{3.26}$$

Observe that in the case of one layer $(k = 1)$ the Equation (3.26) reduces to the reconstruction of the depth integrated velocity (3.15)-(3.16) derived in Kleptsova et al. (2009).

However since the vector $\mathbf{r}_{f,k}$ joining the face f_k and cell c_k centers is in general not horizontal the velocity component normal to the vertical faces of a cell contribute to both horizontal and vertical components of the cell velocity vector $\mathbf{u}_{c,k}$. Therefore, vertical component $w_{c,k}$ of the cell velocity vector can be written as

$$\begin{aligned} w_{c,k} &= \frac{1}{2}(u_{c,k+\frac{1}{2}} + u_{c,k-\frac{1}{2}}) + \\ &+ \sum_{f_k} s_{f,c} d_{f,c} \frac{h_{f,k}(h_{f,k} - h_{c,k}) l_f}{2 h_{c,k} A_c} u_{f,k} \end{aligned} \tag{3.27}$$

This is the ideal case which guarantees the skew-symmetry of the semi-discrete system matrix and thus prevents growth of energy due to the Coriolis term, given a stable time integration scheme.

The requirement that the circumcenters must lie inside of the cells can be quite restrictive with respect to the class of polygons allowed in the grid and make the grid generation more complex. Next examine a possibility to violate the orthogonality conditions, as is done in for example Fringer et al. (2006). Placement of a face center outside of the face seems quite irrational, therefore, consider the following possibility

- Face centers are located in the respective centroids, cell center is located half way between the circumcenters of the top and bottom faces, possibly outside the cell.

  In this case the vectors $\mathbf{r}_{f,k}$ remain the same as in the previous case (see Equation (3.25)). The vectors $\mathbf{r}_{c,k\pm 1/2}$ pointing from the cell center to the centers of the top and bottom faces of the cell can now be expressed as

$$\mathbf{r}_{c,k\pm\frac{1}{2}} = \mathbf{r}_{cc} \pm \frac{h_{c,k}}{2} \mathbf{z} \tag{3.28}$$

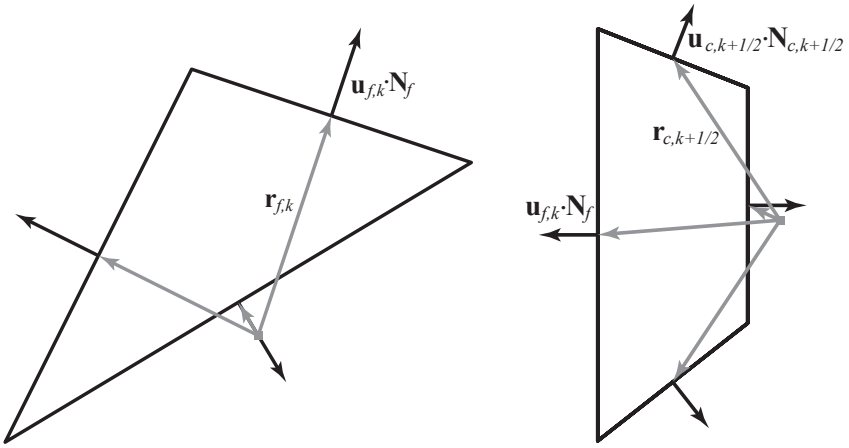

Figure 3.15: Cell and face centers placement: Face center is located in the respective centroid (left), cell center is located half way between the circumcenters of the top and bottom faces (right), possibly outside the cell.

where $\mathbf{r}_{cc}$ is the horizontal vector pointing from the circumcenter of the (triangular) base of the cell to its centroid. As can be easily seen in this case the vectors $\mathbf{r}_{c,k\pm1/2}$ are not in general vertical. Therefore, unlike the previous cases, the velocity components normal to the top and bottom faces of a cell contribute to the velocity components tangential to the vertical faces. The horizontal components of the cell velocity vectors can now be expressed as

$$\mathbf{u}^{xy}_{c,k} = \sum_{f_k} \delta_{f,c} d_{f,c} \frac{h_{f,k} l_f}{h_{c,k} A_c} u_{f,k} \mathbf{n}_f + \frac{1}{h_{c,k}} (u_{c,k+\frac{1}{2}} - u_{c,k-\frac{1}{2}}) \mathbf{r}_{cc} \quad (3.29)$$

The difference between the velocity components normal to the top and bottom faces of the cell can be approximated from the continuity equation $\nabla \cdot \mathbf{u} = 0$ using the Gauss's divergence theorem as follows

$$u_{c,k+1/2} - u_{c,k-1/2} = -\frac{1}{A_c} \sum_{f_k} s_{f,c} A_{f,k} u_{f,k} \quad (3.30)$$

Therefore

$$\mathbf{u}^{xy}_{c,k} = \sum_{f_k} s_{f,c} \frac{h_{f,k} l_f}{h_{c,k} A_c} u_{f,k} (s_{f,c} d_{f,c} \mathbf{n}_f - \mathbf{r}_{cc}) \quad (3.31)$$

Thus this configuration makes the system matrix not skew-symmetric, at least if velocities normal the top and bottom faces are interpolated using (3.30) and not solved for.

3.4 Discussion

C-grid based flow models use velocity components normal to the cell faces as their primary unknowns. In order to evaluate the Coriolis term it is necessary to interpolate the velocity components tangent to the cell faces. Frequently the full velocity vectors are reconstructed first from the staggered in space normal components and then projected in the respective tangent directions. For that purpose a linear reconstruction procedure is typically employed.

A linear reconstruction of the full velocity vector out of normal velocity components must fulfill a very basic consistency requirement. Suppose the face normal components around a cell u_i are derived from the projection of a constant vector $\mathbf{u}$ in each respective normal direction. Consequently for all the face normal components $u_i = \mathbf{u} \cdot \mathbf{n}_i$, where $\mathbf{n_i}$ is the normal vector at face i. Then the consistency condition requires that the vector reconstructed out of these components must be equal to the original vector $\mathbf{u}$. This condition ensures that the reconstructed velocity vectors give a consistent lowest order approximation of the velocity field in each cell. It can be shown that there exists a unique consistent reconstruction of the full velocity vector for each cell e. This reconstruction is given by the polynomial approximation from the lowest order Raviart-Thomas space evaluated in a point of the triangle. Examples of such reconstructions are given in Bonaventura and Ringler (2005); Perot (2000). It is shown in Perot et al. (2006) that the method of Shashkov et al. (1998) is also fully identical to the lowest order FE approach. However, it returns the vector quantity at the corners of the elements, reconstructed using the immediately neighboring face unknowns. To obtain the vector value at the cell center a simple average of the node velocities is suggested.

Projecting the reconstructed velocity in a face tangent direction we typically obtain two values for the tangent velocity component. The final interpolated velocity component is a weighted average of these two values. Although the reconstructions of Bonaventura and Ringler (2005) and Perot (2000) for the cell value are identical, the weights used to average the tangential velocity components obtained from the two adjacent cells differ, they are $\frac{1}{2}$ and $\frac{d_{f,c}}{d_f}$ respectively.

Orthogonal meshes allow us to develop discretisation operators that closely mimic the behavior of invariant differential operators such as divergence, gradient, and curl, see for example Hyman and Shashkov (1999) and Perot (2000). The discrete operators are required to satisfy discrete analogs of the fundamental theorems of vector calculus that hold for their continuous counterparts. This approach permits us to create numerical schemes that preserve solution symmetries and conservation laws, with conservation of kinetic energy being perhaps the most important. It is well known that for purely hyperbolic problems, such as the shallow water equations, the propagation matrices of the semi-discretized partial differential equations should have only purely imaginary eigenvalues, that is they must be similar to skew-symmetric. Espelid et al. (2000) showed that growing and damping computational modes arise if the velocity reconstruction procedure used to calculate the Coriolis term is such that the propagation matrices also acquire a symmetric part. Therefore, the velocity reconstruction procedure must also be mimetic. For the hyperbolic problems this means that the normal velocity of a face should not contribute to its own tangential velocity.

For the flat bottom case it is easy to see that the reconstruction by Perot (2000) (Equation (3.3)-(3.4)) is mimetic, whereas the reconstruction by Bonaventura and Ringler (2005) preserves skew-symmetry of the propagation matrix only for uniform meshes.

In Section 3.1 it is shown that the weights for a linear velocity reconstruction procedure should not be chosen arbitrary from purely mathematical consistency considerations (see Bonaventura and Ringler (2005); Shashkov et al. (1998)) or underlying symmetry preservation requirements, which do not give a unique answer (see Ham et al. (2007); Espelid and Berntsen (2007)), but should be consistent with the way in which the SWE's are solved.

In Section 3.3 we consider a reconstruction of the 3D velocity vector out of its spatially distributed normal components, as typically required in the C-grid models. The method is valid for any choice the vertical coordinates. It is based on the approach proposed by Perot (2000) for 2D Navier-Stokes equations which is widely used, see for instance Kleptsova et al. (2009), Kramer and Stelling (2008), Fringer et al. (2006), Stuhne and Peltier (2009). The method guaranties the reconstructed velocity field to satisfy the continuity equation. The distinctive feature of this approach is that it is valid for both structured and unstructured grids consisting of any cyclic polygons. The circumcentre of the polygon is only required to exist and is not assumed to lie inside of the polygon.

If, however, the circumcentre falls outside of the polygon, the velocity components normal to the top and bottom faces of the cell and located in the face centroids does contribute to the velocity components tangent to the vertical faces of the cell, see Equation (3.31). Therefore, a model which approximates the velocity component normal to the top and bottom faces of a cell from the continuity equation may exhibit growth of energy due to the Coriols term.

Velocity components normal to the vertical faces of the cell contribute both to the horizontal and vertical compnents of the velocity vector located at the cell circumcentre, see Equation (3.27). This fact is usually overlooked then evaluating the vertical velocity component w.

The inaccuracy introduced by the tangential velocity interpolation may not always be apparent. In more realistic simulations which include the effects of bottom friction, advection and diffusion the instability may well be suppressed. Indeed a small amount of friction may be all that is required in some cases to stabilize the system matrix. However, while this might be enough to hide the fact that the tangential velocities are inaccurately calculated, it can lead to errors in the calculation of the Coriolis force.

The accurate reproduction of the geostrophic balance is crucial to the correct evolution of shelf and basin scale flows. The simple geostrophic balance experiment performed here, clearly demonstrates that an incorrect tangential velocity interpolation method, may erroneously generate flow in the no flow direction and hence can corrupt the numerical solution. In a more realistic simulation one might not even be aware of this error, yet as shown here, it can decrease the magnitude of the geostrophic flow in the dominant along-axis direction and erroneously generate a flow in the cross-axis direction. This is also true for structured grid models; yet this problem is hardly ever addressed, the exception being the paper by Espelid et al. (2000).

Note, that the discrete kinetic energy conservation considered here provides necessary, but not sufficient condition of the model stability. Another important aspect to be considered is the stability of a time integration scheme used for discretisation of the Coriolis term. The semi-implicit approach used in this Chapter removes stability constraints. It, however, requires sparse velocity matrix to be inverted and, therefore, is inefficient for large models. A variety of explicit methods for the discretisation of the Coriolis term and their stabilty is considered in Walters et al. (2009).

4

Treatment of the advection term on a C-grid discretisation

Note. The content of this chapter is based on the the following paper: *Kleptsova et al. (2010), An accurate momentum advection scheme for a $z-$level coordinate models.*

The schemes of Casulli and Walters (2000) and Ham et al. (2005) combine a semi-implicit time integration of the equations with a semi-Lagrangian approach for the advection term. While this is stable at any flow Courant number, this approach is unable to provide momentum conservation. Thus, it is not suitable for the modeling of rapidly varied shallow water flows as typically found in flooding situations, for example dam break problems or tsunamis. Stelling and Duinmeijer (2003) show how conservation can be achieved. They combine a semi-implicit time integration scheme with an Eulerian advection scheme with a special choice for the discretisation of the advective velocity. While imposing a restriction on the time-step, this scheme conserves momentum.

4.1 Advection discretisation

In this section two Eulerian advection schemes are considered. The first scheme was proposed by Perot (2000) for Navier-Stokes equations. The second scheme based on the scheme by Perot (2000) was derived by Kramer and Stelling (2008) for the depth-integrated and depth-averaged shallow water equations.

4.1.1 Advection discretisation by Perot (2000)

Following Perot (2000) first a finite volume discretisation $\mathbf{a}_{c,k}$ of the cell based advection term is derived by integrating the vector $\vec{\nabla}\cdot(\mathbf{uu}) = \mathbf{u}\cdot[\nabla u, \nabla v, \nabla w]$ over a cell using the Gauss' theorem

$$\int_{\Omega^3} \vec{\nabla}\cdot(\mathbf{uu})dV = \int_{\partial\Omega} \mathbf{u}(\mathbf{u}\cdot\mathbf{N})dS \tag{4.1}$$

Assuming a prismatic cell with the base area A_c and height $h_{c,k}$, this yields

$$\begin{aligned} A_c h_{c,k}\mathbf{a}_{c,k} &= \sum_{f_k} s_{f,c} h_{f,k} l_f u_{f,k}\mathbf{u}_{f,k} + \\ &+ A_c\left(\mathbf{u}_{c,k+\frac{1}{2}} u_{c,k+\frac{1}{2}} - \mathbf{u}_{c,k-\frac{1}{2}} u_{c,k-\frac{1}{2}}\right) \end{aligned} \tag{4.2}$$

The face velocity vectors $\mathbf{u}_{f,k}$ are interpolated as given in Equations (3.23) and (3.26)-(3.27). The velocity vectors $\mathbf{u}_{c,k\pm\frac{1}{2}}$ attached at the centers of the "horizontal" faces of the cell are interpolated as following:

$$\begin{aligned} \mathbf{u}_{c,k-\frac{1}{2}} &= \frac{h_{c,k-1}}{h_{c,k-1}+h_{c,k}}\mathbf{u}_{c,k-1} + \frac{h_{c,k}}{h_{c,k-1}+h_{c,k}}\mathbf{u}_{c,k} \\ \mathbf{u}_{c,k+\frac{1}{2}} &= \frac{h_{c,k}}{h_{c,k}+h_{c,k+1}}\mathbf{u}_{c,k} + \frac{h_{c,k+1}}{h_{c,k}+h_{c,k+1}}\mathbf{u}_{c,k+1} \end{aligned} \tag{4.3}$$

Observe, that the velocity component $u_{c,k\pm\frac{1}{2}}$ normal to the "horizontal" faces of a cell is not, in general, equal to the vertical velocity component w, as can be seen from Figure 4.1.

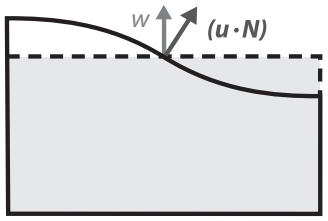

Figure 4.1: A water column top cell together with vertical and normal to the surface velocities.

Integrating the 3D continuity equation in vertical from bottom to a vertical level $z_{k+\frac{1}{2}}$ and applying kinematic boundary condition (2.9) at the bed one arrives at the following expression for the velocity normal to the "horizontal" faces of a cell

$$u_{c,k+\frac{1}{2}} = -\frac{1}{A_c}\sum_{f_i}\sum_{i=k_b}^{k} s_{f,c} h_{f,i} l_f u_{f,i} \tag{4.4}$$

where k_b is the index of the column's bottom layer.

Next the face normal component of the advection term is reconstructed out of a given set of the cell based vectors $\mathbf{a}_c$, by taking the following linear combination:

$$a_{f,k} = \sum_{c_k} \delta_{f_k,c_k} \alpha_{f,c} (\mathbf{a}_{c,k} \cdot \mathbf{n}_f) \tag{4.5}$$

The weighting coefficients $\alpha_{f,c}$ are defined by Perot (2000) as

$$\alpha_{f,c} = \frac{d_{f,c}}{d_f} \tag{4.6}$$

Other definitions of the weighting factors are possible, see for example Wenneker et al. (2002). Influence of the weighting factors on the performance of the depth integrated scheme is examined in Kramer and Stelling (2008).

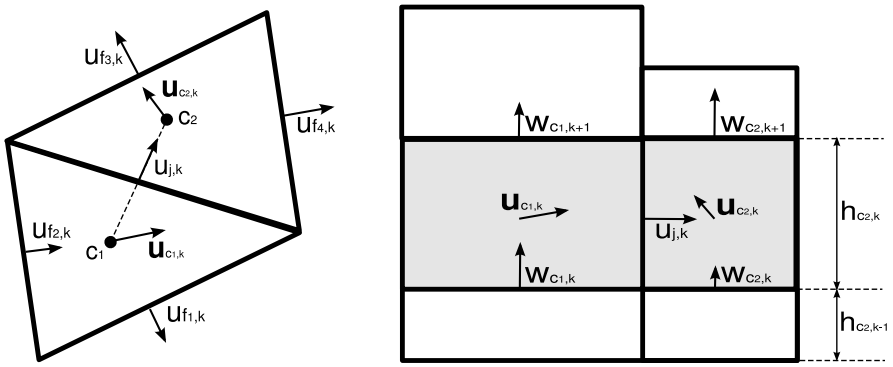

Figure 4.2: The control volume (shaded area) used to discretise the horizontal momentum equation at face j, showing the plan form (left) and side (right) views.

Thus, the advection component normal to the face j_k shown in Figure 4.2 can be written as

$$a_{j,k} = \sum_{c_k} \delta_{j_k,c_k} \alpha_{j,c} \frac{1}{A_c h_{c,k}} \sum_{f_k} \Bigg[s_{f,c} h_{f,k} l_f u_{f,k} (\mathbf{u}_{f,k} \cdot \mathbf{n}_j) - \\ - \left(\mathbf{u}_{c,k+\frac{1}{2}} \sum_{i=k_b}^{k} s_{f,c} h_{f,i} l_f u_{f,i} - \mathbf{u}_{c,k-\frac{1}{2}} \sum_{i=k_b}^{k-1} s_{f,c} h_{f,i} l_f u_{f,i} \right) \cdot \mathbf{n}_j \Bigg] \tag{4.7}$$

Observe that only the horizontal components of the velocity vectors $\mathbf{u}_{c,k}$ and $\mathbf{u}_{f,k}$ are to be interpolated.

In single layer case ($k = 1$) the horizontal velocity field is assumed to be constant in the vertical. In this case, cells c_1 and faces f_1 correspond to columns c and column sides f. Therefore height of the cells and faces become equal to the water depth at the respective columns and column sides. Thus, the Equation (4.7) reduces to

$$a_j = \sum_c \delta_{j,c} \alpha_{j,c} \sum_f s_{f,c} \frac{h_f l_f}{A_c h_c} u_f (\mathbf{u}_f - \mathbf{u}_c) \cdot \mathbf{n}_j \tag{4.8}$$

To avoid division by zero if a column c is dry, the water depth h_c of such column is set to the threshold value h_{min} used for flooding.

4.1.2 Advection discretisation by Kramer (2008)

In Kramer and Stelling (2008) another discretisation of the advection term a_j for the depth-averaged equations (i.e. for one layer case) is presented. This scheme is a combination of the unstructured grid variant of the advection scheme by Stelling and Duinmeijer (2003) with the advection scheme by Perot (2000) described above.

$$a_j = \sum_c \delta_{j,c} \alpha_{j,c} \sum_f s_{f,c} \frac{h_f l_f}{A_c \bar{h}_j} u_f (\mathbf{u}_f^* \cdot \mathbf{n}_j - u_j) \tag{4.9}$$

The water depth $\bar{h}_j$ at the column side (face) j defined as

$$\bar{h}_j = \sum_c \alpha_{j,c} h_c \tag{4.10}$$

The vector $\mathbf{u}_f^*$ is the full velocity vector at the column side (face) f reconstructed out of the velocity components from the column (cell) c^* upwind of column side (face) f as given in Equation (3.26), that is

$$\mathbf{u}_f^* = \mathbf{u}_{c*} \tag{4.11}$$

Note, that the upwind column is always wet, that is division by zero in Equation (3.26) will never occur.

If the upwind column (cell) is the one containing the column side (face) j, $\mathbf{u}_f^* \cdot \mathbf{n}_j$ is approximated as u_j. Thus the fluxes going out of the column (cell) can be omitted without changing of momentum.

This scheme was originally derived applying the Perot (2000) scheme to the depth–integrated velocities $h\mathbf{u}$ and rewriting it for the depth–averaged velocities. This was done using the equivalence between the depth–integrated and the depth–averaged momentum equations and the fact that time derivative of $h\mathbf{u}$ can be split into a contribution from the change in water volume and a contribution from the change in velocity.

In the case of multiple layers the contribution from the change in velocity corresponds to the contribution from the vertical faces of the cell, the contribution from the change in water volume corresponds to the contribution from the "horizontal" faces. Thus, to obtain a multilayer version of scheme by Kramer and Stelling (2008), one can use the following cell based advection vector $\mathbf{a}_{c,k}(j_k)$ calculated for a face j_k of the cell c_k (the analogue of Equation (4.2))

$$\begin{aligned} A_c \bar{h}_{j,k} \mathbf{a}_{c,k}(j_k) = \sum_{f_k} s_{f,c} h_{f,k} l_f u_{f,k} \mathbf{u}^*_{f,k} + \\ + A_c \left(\mathbf{u}_{j,k+\frac{1}{2}} u_{c,k+\frac{1}{2}} - \mathbf{u}_{j,k-\frac{1}{2}} u_{c,k-\frac{1}{2}} \right) \end{aligned} \tag{4.12}$$

with

$$\begin{aligned} \mathbf{u}_{j,k-\frac{1}{2}} &= \frac{\bar{h}_{j,k-1}}{\bar{h}_{j,k-1} + \bar{h}_{j,k}} \mathbf{u}_{j,k-1} + \frac{\bar{h}_{j,k}}{\bar{h}_{j,k-1} + \bar{h}_{j,k}} \mathbf{u}_{j,k} \\ \mathbf{u}_{j,k+\frac{1}{2}} &= \frac{\bar{h}_{j,k}}{\bar{h}_{j,k} + \bar{h}_{j,k+1}} \mathbf{u}_{j,k} + \frac{\bar{h}_{j,k+1}}{\bar{h}_{j,k} + \bar{h}_{j,k+1}} \mathbf{u}_{j,k+1} \end{aligned} \tag{4.13}$$

Thus, the multilayer version of the advection scheme (4.9) can be written as following:

$$\begin{aligned} a_{j,k} = \sum_{c_k} \delta_{j_k,c_k} \alpha_{j,c} \sum_{f_k} s_{f,c} \frac{1}{A_c \bar{h}_{j,k}} \Bigg[h_{f,k} l_f u_{f,k} (\mathbf{u}^*_{f,k} \cdot \mathbf{n}_j) - \\ - \left(u_{j,k+\frac{1}{2}} \sum_{i=k_b}^{k} h_{f,i} l_f u_{f,i} - u_{j,k-\frac{1}{2}} \sum_{i=k_b}^{k-1} h_{f,i} l_f u_{f,i} \right) \Bigg] \end{aligned} \tag{4.14}$$

with k_b being the index of the column's bottom layer.

The advection schemes described above will be compared using a number of two-dimensional test cases in the following section.

4.2 Test cases

All of the simulations described in this section are performed with one layer in vertical, that is the advection term is discretised according to Equations (4.8) and (4.9). Simulations of dam break and tsunami run-up on a plane beach were also simulated using the semi-Lagrangian advection scheme by Ham et al. (2005).

4.2.1 Kelvin wave test case

If the water depth is (locally) close to uniform, then the water depth at a column side (height of a face) is approximately equal to that a the neighboring columns (cells). Similarly, a cell (column) based velocity vector projected in the direction normal to a face of the cell (normal to a side of the column) is approximately equal to the face (column side) normal velocity component, if the flow velocity is (locally) close to uniform. Thus, the advection schemes described above will behave similarly in the test cases with no sudden changes in water depth and flow velocity.

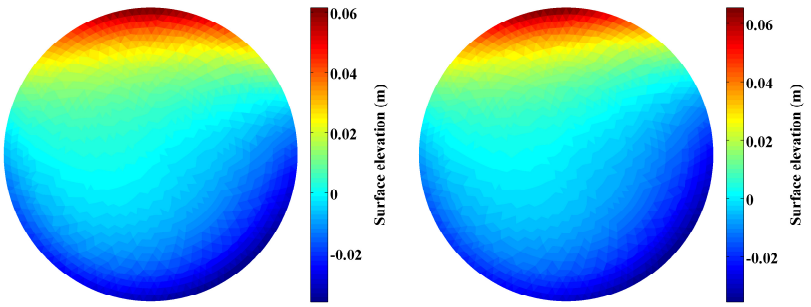

Figure 4.3: Kelvin wave in a circular basin: the sea surface elevation after 1666.6 hours calculated using the advection scheme by Perot (2000) (left) and Kramer and Stelling (2008) (right).

To illustrate this a Kelvin wave in a shallow circular basin test case, described

in Ham et al. (2005), is used. The basin was given a uniform depth of $5m$. The initial state chosen was:

$$\begin{gathered}\eta(r,\theta) = 0.05e^{(r-r_0)/L_D}\cos\theta \\ u_\theta(r,\theta) = 0.05\sqrt{g/h}e^{(r-r_0)/L_D}\cos\theta \\ u_r(r,\theta) = 0\end{gathered} \tag{4.15}$$

where L_D is the Rossby radius, in this case approximately $68km$, and $r_0 = 250km$ is the basin radius. In the limiting case of an infinitely large basin, this is the expression for a Kelvin wave of amplitude $5cm$.

The simulation was performed at a specified latitude of $45°$. Figure 4.3 shows the sea surface elevation after 1666.6 hours. As expected, the results obtained using different advection schemes are identical up to visible precision.

4.2.2 Dam break test case

A dam break is calculated in a $100m$ long and $10m$ wide channel. At $t = 0$ the shock starts at $x = 50m$ with zero initial velocity and the upstream water level of $1m$. For the dam break over wet bed case the water level downstream is $0.1m$. The nominal triangle edge length of the grid used is 2 m. The time step of $0.01s$ was used for the simulation of the dam break over wet bed. The numerical solutions at the time of $5s$ compared to the analytical solution are shown in Figure 4.4.

For the simulation of the dam break over dry bed the time step was set to $0.001s$. Threshold value h_{min} used to mask columns as dry was set to $2.5mm$. Comparison of the numerical solution at the time of $5s$ to the analytical solution is shown in Figure 4.5.

In both cases the results obtained using the advection scheme similar to Kramer and Stelling (2008) given by Equations (4.9) and (4.14) show better agreement with the analytical solution than the schemes by Ham et al. (2005) and Perot (2000) given by Equations (4.7) and (4.8). Besides that, the advection scheme by Kramer and Stelling (2008) leads to a smoother solution due to the first order upwinding.

4.2.3 Tsunami run-up on a plane beach

Here run-up and run-down motion of a tsunami-type transient wave onto a plane sloping beach with slope $s = 1/10$ is examined.

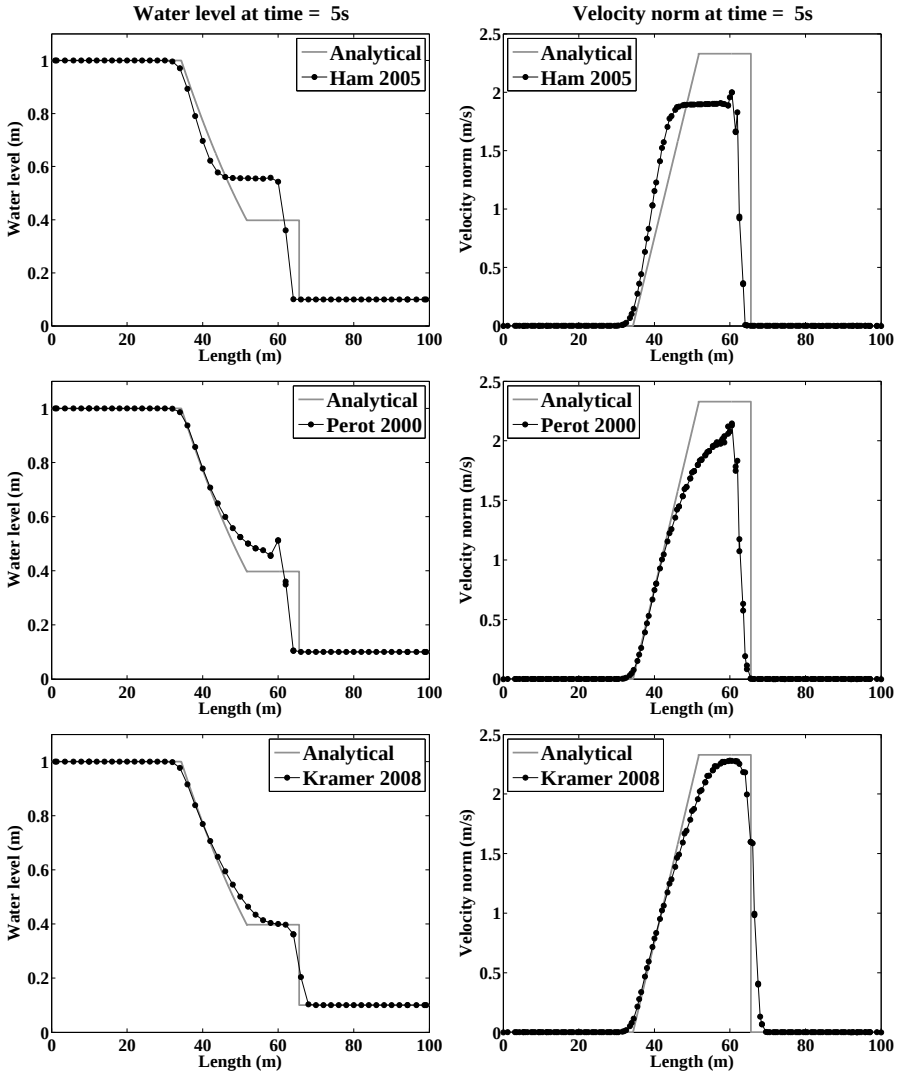

Figure 4.4: Dam break over wet bed: surface elevation and velocity calculated using the semi-Lagrangian advection by Ham et al. (2005) (top row) and the Eulerian advection schemes given by Equation (4.8) (middle row) and Equation (4.9) (bottom row) compared with the analytical solution (grey line).

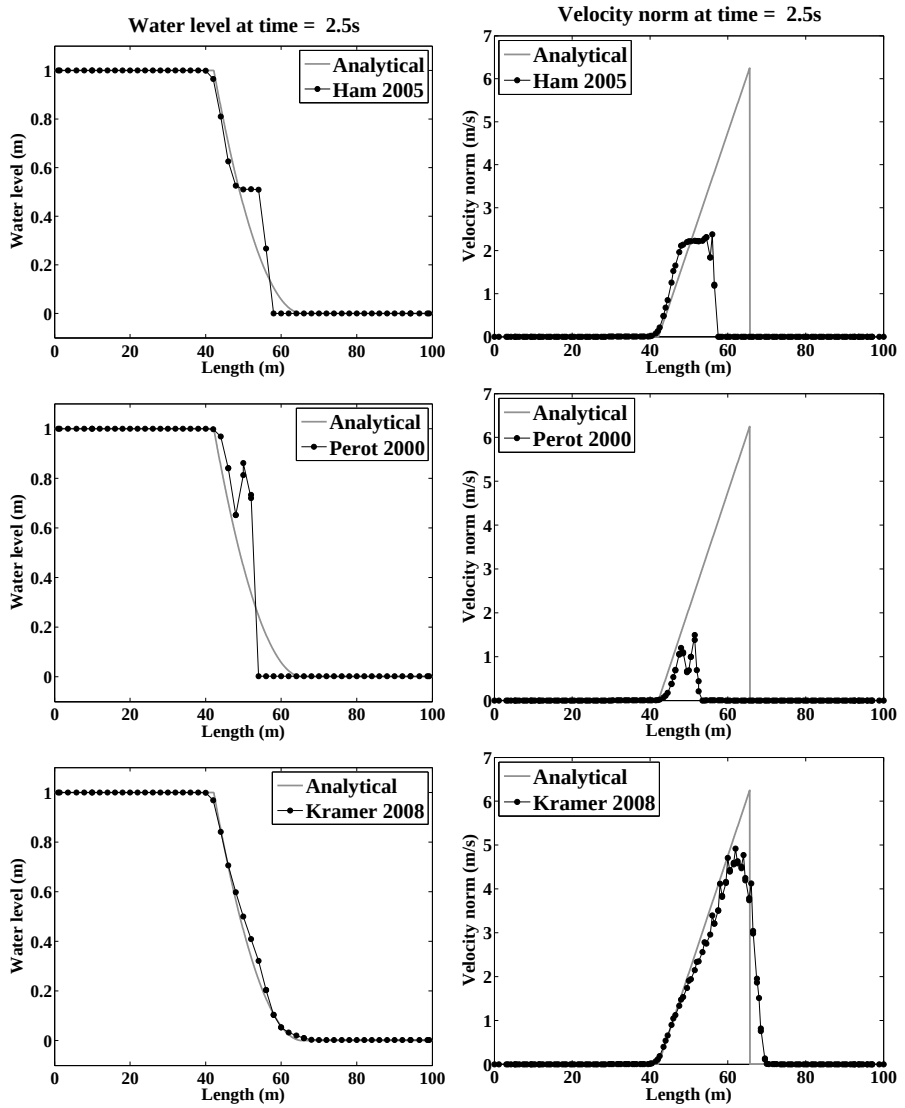

Figure 4.5: Dam break over dry bed: surface elevation and velocity calculated using the semi-Lagrangian advection by Ham et al. (2005) (top row) and the Eulerian advection schemes given by Equation (4.8) (middle row) and Equation (4.9) (bottom row) compared with the analytical solution (grey line).

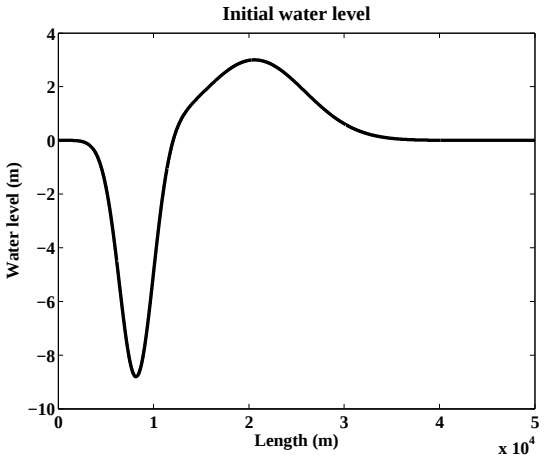

Figure 4.6: Tsunami run-up on a plane beach: a portion of the initial surface elevation given by Equation (4.16) used in the tsunami run-up simulation.

The initial free surface shown in Figure 4.6 is specified according to

$$\eta = 500(0.006e^{-0.4444(\frac{x}{5000}-4.1209)^2} - 0.018e^{-4.0(\frac{x}{5000}-1.6384)^2}) \qquad (4.16)$$

which corresponds to the leading depression N-wave shape, typically caused by an offshore submarine landslide. This case corresponds to the case D in Carrier et al. (2003), who derived a general semi-analytic solution for such events based on nonlinear shallow water equations.

Upon the release of the initial wave form, tsunami-type waves propagate in both landward and offshore directions, though only the landward traveling wave runs up the beach. At the offshore boundary a closed boundary condition is imposed. Since the computational domain is sufficiently long ($50km$) this does not affect the run-up process on the other side of the domain.

Simulation was performed on a 8681 node grid, with resolution varying from $8m$ in the shallow region to $318m$ in the deep water. The time step was set to 1 second. The columns were masked as dry if their water depth was less then $h_{min} = 1cm$. The initial velocity is set to zero everywhere. The Figure 4.7 shows the comparison of the computed surface elevation against the analytical solution for $t = 160, 175, 220$ seconds.

Once again, the results obtained using the advection scheme similar to Kramer and Stelling (2008) given by Equations (4.9), (4.14) agree with the analytical solution better than the ones obtained using the schemes by Perot (2000) and Ham et al. (2005). During the run-up period the schemes by Perot (2000) and

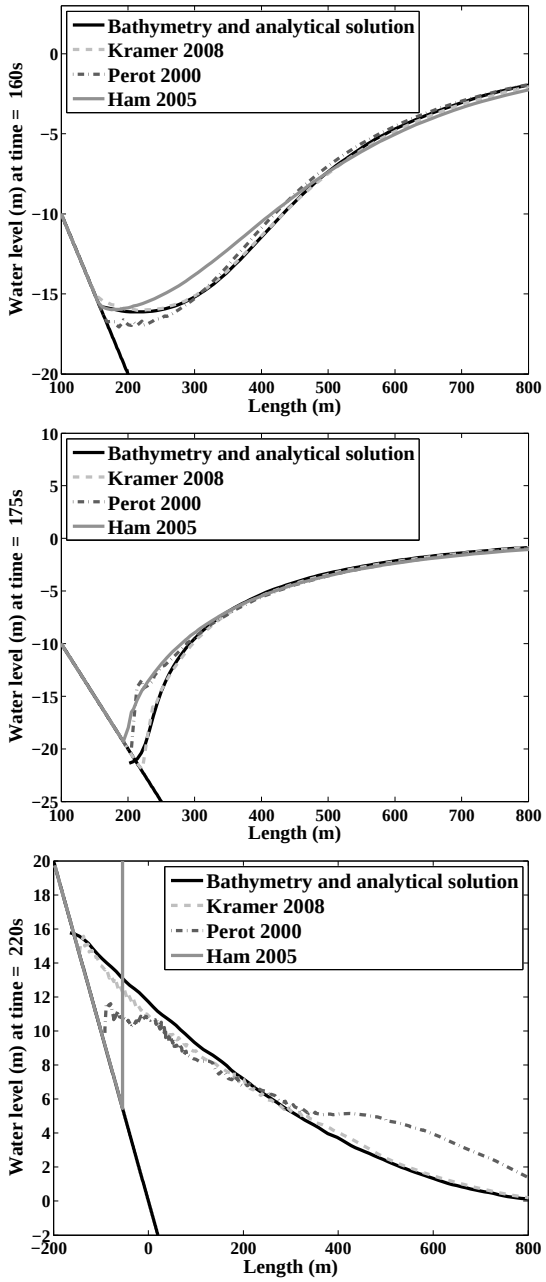

Figure 4.7: Tsunami run-up on a plane beach: comparison of the computed surface elevation profiles against the analytical prediction for $t = 160s$ (top), $t = 175s$ (middle) and $t = 220s$ (bottom).

Ham et al. (2005) show similar results. The semi-Lagrangian advection sheme by Ham et al. (2005), however, became unstable during the run-down of the tsunami wave.

4.2.4 Parabolic flood wave

A water mass with a parabolic shape given by

$$\eta_0 = h_0 \left(1 - \frac{x^2 + y^2}{R_0^2}\right) \tag{4.17}$$

is released on a flat bed without friction. Here $R_0 = 50km$ and $h_0 = 2km$ are the initial radius and the initial height of the water mass respectively. The analytical solution of the test is given by (see Thacker (1981))

$$\eta = h_0 \left[\frac{T^2}{t^2 + T^2} - \frac{x^2 + y^2}{R_0^2}\left(\frac{T^2}{t^2 + T^2}\right)^2\right] \tag{4.18}$$

Here

$$T = \frac{R_0}{\sqrt{2gh_0}} = 250s \tag{4.19}$$

is the time after which the initial height h_0 has been halved. Initially the water mass is set at rest. The time step used is $\Delta t = 2s$. The numerical solution for the cross section $y = 0$ compared with the analytical solution Equation (4.18) for $t = 200, 600$ and 1000 seconds is shown in Figure 4.8

In this case, the advection schemes by Perot (2000) and Kramer and Stelling (2008) give similar results which are in a good agreement with the analytical solution for the time $t = 200$ seconds. For the time $t = 600$ and 1000 seconds results obtained using the scheme by Kramer and Stelling (2008) are much better than that of the scheme by Perot (2000). Moreover, for this test case using of the advection scheme by Perot (2000) led to the model instability. Reducing the time step by the factor of 10 did not solve the stability problem. The results shown here were obtained with h_c substituted by $\bar{h}_j$ in the denominator of Equation (4.8). Some other experiments also show that substitution of $\bar{h}_j$ in place of h_c in Equation (4.9) leads to increased stability and slightly better results.

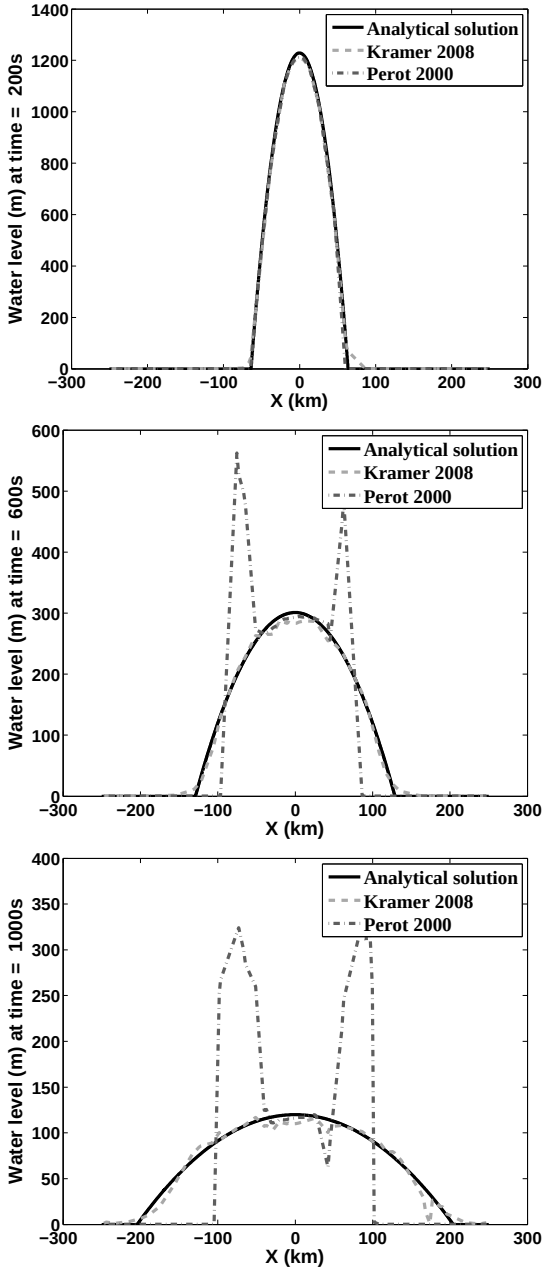

Figure 4.8: Parabolic flood wave: comparison of the computed (dots) surface elevation profile against the analytical prediction (solid line) for $t = 200, 600$ and 1000 seconds.

4.3 Discussion

Many shallow water models for large scale simulations are based upon the application of staggered C-grids. They provide efficient and accurate solutions for sub-critical, geostrophic flows, in particular in combination with semi-implicit time integration. The unstructured finite volume scheme of Casulli and Walters (2000) combines a semi-implicit time integration of the equations with a semi-Lagrangian approach for the advection term. Such a scheme can be shown to be stable at any flow Courant number. This approach was also adopted in Delfin, Ham et al. (2005). The drawback of such schemes is that most implementations do not provide conservation of momentum and, hence, are not suitable for simulation of such phenomena as flooding and drying. Accurate simulations of flooding and drying are important for dam break problems and tsunami simulations.

Here two Eulerian advection schemes based on the scheme of Perot (2000), namely the schemes of Fringer et al. (2006) and Kramer and Stelling (2008) are compared. It is shown that the scheme of Kramer and Stelling (2008) gives better results for dam break problems. While imposing a restriction on the time-step, this scheme conserves momentum.

5

On techniques for z-layer implementation

Note. The content of this chapter is based on the the following paper: *Kleptsova et al. (2010), An accurate momentum advection scheme for a $z-$level coordinate models.*

An important aspect in three dimensional ocean modeling is the choice of the vertical coordinate system. Three distinct types of vertical coordinates are in general use, geopotential $z-$level coordinates, terrain following σcoordinates and isopycnal coordinates. There is no single coordinate system that is suitable for all applications, as each of these coordinate systems has its own advantages and disadvantages. Here the main interest lies in coastal ocean modeling, and in particular in accurately simulating flows in the shallow near shore region, including flooding and drying problems. It is in this region that exchange between the land and ocean occurs, it is a region of increasing importance to oceanographers.

Isopycnal coordinates have been successfully used in large scale ocean models, such as MICOM, Bleck et al. (1992) and HIM, Hallberg (1997). These are capable of retaining sharp interfaces and fronts. In the coastal regions, however, the layers of predefined constant density must be able to collapse into one layer under well-mixed conditions and to inflate into a number of layers under stratified conditions. Together with weak ability to simulate surface and bottom boundary layers this limits use of isopycnal coordinates in coastal models.

The main advantage of the $\sigma-$coordinate system is the fact that it is fitted to both the moving free surface and bottom topography. This allows one to accurately approximate the vertical flow distribution without a large number of vertical grid points. The terrain following coordinates allow an efficient grid

refinement near the free surface and the bed, which makes it easy to resolve the boundary layers. However, a systematic error in the calculation of the baroclinic pressure gradient terms can arise in regions with steep topography and sharp density gradients when using $\sigma-$coordinates. A number of methods exist to reduce the pressure gradient error, some of them are summarized in Stelling and Van Kester (1994) and Kliem and Pietrzak (1999).

Efforts are now underway to create generalized and hybrid coordinate models, such as HYCOM, Bleck (2002) and Burchard and Petersen (1997), that can employ appropriate coordinates in different regions. Alternative vertical coordinate systems are also being explored. Adcroft and Campin (2004) propose a rescaled height coordinate system which is essentially height based but shares some similarity with $\sigma-$coordinates. Halyer and Lermusiaux (2010) employ time dependent, terrain-following coordinates. They first define a set of terrain-following depths for the mean sea level, and then a set of time variable model depths such that the change in cell thickness is proportional to the relative thickness of the original (undisturbed) cell.

Geopotential $z-$level coordinates do not suffer from the pressure-gradient error associated with $\sigma-$coordinates. The main problem with $z-$level models are connected with flow along a sloping bottom and surface. In this case the stepwise discontinuous representation of the topography and free surface can generate false flow structures, which is referred to here as the staircase problem. The treatment of the bottom topography can be improved by using a finite volume discretisation which allows one to use variable bottom layer thickness (partial cells) or shaped volumes (”shaved” cells) as proposed by Adcroft et al. (1997). However, as shown here this is not the complete solution.

The $z-$coordinates are referenced to a time mean water level. The free-surface displacement moves relative to this coordinates system and is to be implemented as a moving boundary. In Griffies et al. (2001) and Campin et al. (2004) this is done by allowing the top model layer to vary in thickness. The free-surface variation, however, must be smaller than that of the top layer thickness. This becomes a serious limitation with increasing vertical resolution and in shallow regions where extensive flooding and drying can take place. A model can be coded to allow the top layer to vanish as it is done in Delfin, Ham et al. (2005), or to become dry as in SUNTANS, Fringer et al. (2006). The second layer then takes on the role of the surface layer with variable thickness. The major difficulty here is to make the transition of a vanishing layer smooth enough to avoid the staircase problem which leads to the generation of false currents, stability and conservation problems.

In a large scale hydrodynamic model a vertical structure of the flow must be created only due to physical mechanisms such as shear stress or complex bottom profiles yielding flow separation. Without that the results of two- and three-dimensional models should be identical. Therefore, special attention is required for the discretisation of the momentum equation in the 3D- case.

The staircase problem can be avoided by using a semi-Lagrangian advection scheme, such as the schemes by Casulli and Walters (2000) and Ham et al. (2005). This approach is, however, unable to provide momentum conservation and, thus, it is not suitable for the modeling of rapidly varied shallow water flows as typically found in flooding situations, for example dam break problems or tsunamis. Other schemes, such as the schemes of Fringer et al. (2006) and Stuhne and Peltier (2009) both employing the Eulerian advection scheme by Perot (2000) have the staircase problem. Indeed, the model of Fringer et al. (2006) does not conserve momentum in the cells that contain the free surface. SUNTANS is, however, mainly used for internal gravity wave simulations and the free surface dynamics are not their main concern. Stuhne and Peltier (2009) in their 3D global M_2 tide simulation note deterioration of results in the coastal regions compared to their 2D simulation.

In this chapter it shown how one can design an Eulerian advective approximation which solves the staircase problem and prevents the model from creating an artificial vertical structure. To show the strength of this approach it is even applied it to dam break problems. Although, the staircase problem is not related to the choice of the horizontal discretisation as such, in the C-grid class of models an artificial vertical structure can also be created due to the Coriolis force, since in this class of models a tangential velocity reconstruction has to be used.

5.1 Discretisation of advection and Coriolis terms in the multilayer case

The advection scheme by Perot (2000) has been used successfully in a number of unstructured grid models, see, for example, Stuhne and Peltier (2009) and Fringer et al. (2006). However, Stuhne and Peltier (2009) noticed that the results of their multi-layer simulation of the global M_2 tide were much worse in the coastal region, than the same results but from a 2D simulation. Whereas the deep ocean amphidromic patterns are similarly resolved in both the 2D and 3D cases. Fringer et al. (2006) successfully use the advection scheme by Perot (2000) for internal wave simulations. They, however, claim that the

advection scheme does not conserve momentum in the cells containing the free surfaces. This is quite a surprising statement given the good deep ocean results of Stuhne and Peltier (2009). A possible reason for the lack of conservation could be the use of the vertical velocity w in place of the velocity normal to the "horizontal" faces, see Figure 4.1. If that is so, the deterioration of the results should not be seen in the case of multiple layer simulation, since the normal velocity interpolation is used.

To assess this use a two layer simulation of the dam break over a wet bed as described in Section 4.2. Simulations were performed using both the momentum advection schemes (4.7) and (4.14), however, only the results for the scheme (4.14) are shown. Figure 5.1 shows the surface elevation and the face velocity norm for the two layers with at $z_1 = 0.08m$ and $z_2 = 1.0m$ above the bed. Both the free surface and velocity are represented much worse here than in the

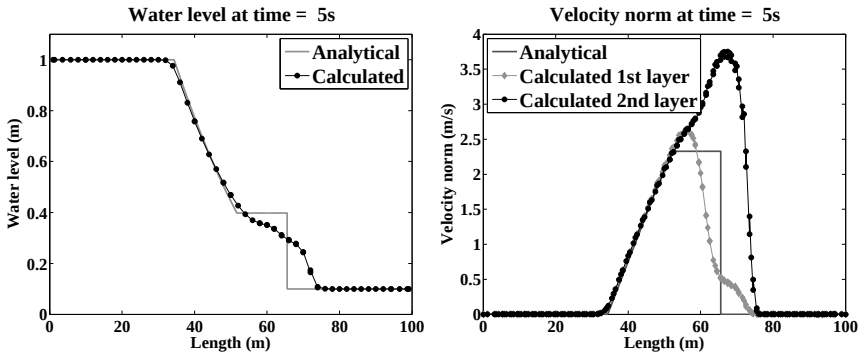

Figure 5.1: Dam break over wet bed: surface elevation and velocity norm for the two layer calculation compared with the analytical solution.

one layer simulation, shown in Figure 4.4. Moreover, the calculated flow velocity differs across the layers, whereas it should be uniform. As can be seen difference in the velocity norm between the layers for the faces on one column side is as high as $3.31m/s$.

In C-grid models the discretisation of Coriolis term may suffer from the similar problem when multiple $z-$layers are used. To demonstrate this use one of the test cases described in Section 5.3.1, namely the periodic flow with an initially tilted planar free surface. As can be seen from Figure 5.2 the model becomes unstable when multiple $z-$layers are used.

Our conjecture is that the poor free surface representation and stability problem is caused by the artificial vertical structure in the flow, which is created solely due to the presence of vertical $z-$layers. For the $z-$layer models, the face

heights are usually defined as $h_{f,k} = h_{c,k}$ and all of the cell heights $h_{c,k}$ are equal to each other everywhere except for the cells containing the free surface (and bed). Due to this, the contribution to the change of momentum from the change of velocity (contribution from the vertical faces in Equations (4.2) and (4.12) for the internal layers is not the same as for the top and bottom layer. Similarly, the velocity reconstruction procedure (3.22) for the internal layers is different from that for the top and bottom layer.

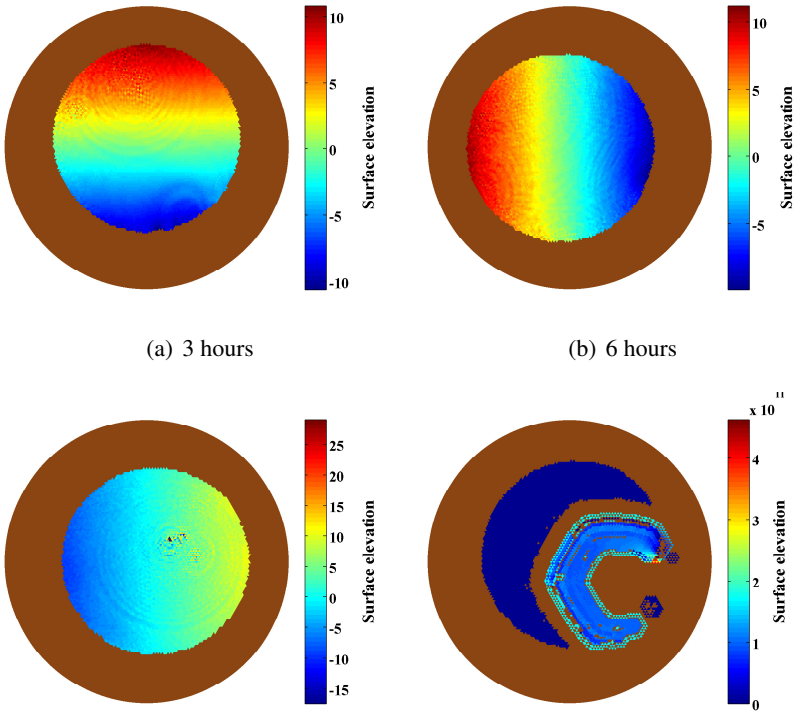

(a) 3 hours (b) 6 hours

(c) 12 hours (d) 13.5 hours

Figure 5.2: Surface elevation of the periodic flow with an initially tilted planar free surface.

In the Section 5.2, using the momentum advection scheme (4.14) as an example, it is shown how one can prevent the model from creating artificial vertical structure in the flow.

5.2 Improved $z-$layer implementation

In absence of bottom friction the flow velocity should be constant in depth. That is the momentum equation (2.16) should be identical for all of the layers. This means that advection and Coriolis operators for a particular layer should be the same as for the whole water column. This is possible if the ratio of a cell height to the height of its face is the same as the ratio of the respective column water depth to the column side water depth this face belong to. That is, the identity

$$\frac{h_{f,k}}{h_{c,k}} = \frac{h_f}{h_c} \tag{5.1}$$

should be valid for all cells and faces.

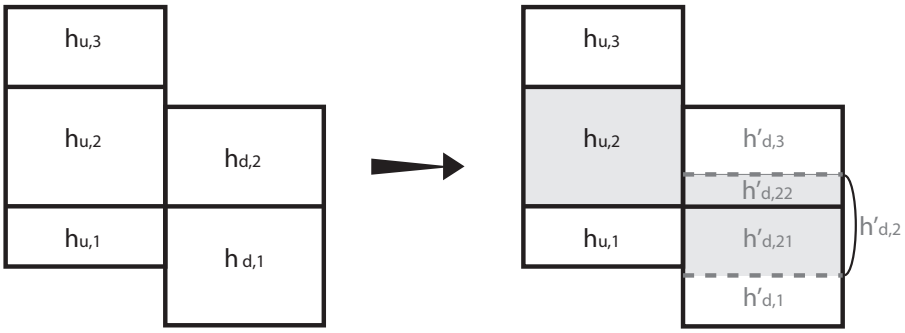

Figure 5.3: The side view of the control volume (shaded area) used to discretise the horizontal momentum equation at a face.

Assume the situation shown in the left panel of Figure 5.3: the column upwind of the column side j has three layers with heights $h_{u,k}$, whereas the downwind column has only two layers with heights $h_{d,k}$. Define for the downwind column adjacent to the column side j exactly three sub–layers whose thickness $h'_{d,k}$ is determined by

$$h'_{d,k} = \frac{h_{j,k}}{h_j} h_d \tag{5.2}$$

Since the water depth at the column side j is equal to that of the upwind column and $h_{j,k} = h_{u,k}$, the relation (5.1) holds automatically for the column side j and the upwind column. The heights of the other faces need to be redefined according to Equation (5.1) for both of the columns.

With the above definition the advection term $a_{j,k'}$ given by Equation (4.14)

becomes

$$a_{j,k'} = \sum_{c'_k} \delta_{j_{k'},c_{k'}} \alpha_{j,c} \sum_{f'_k} s_{f,c} \frac{1}{A_c \bar{h}_j} \Big[h_f l_f u_{f,k'} (\mathbf{u}^*_{f,k'} \cdot \mathbf{n}_j) - \\ - \left(u_{j,k'+\frac{1}{2}} \sum_{i=k'_b}^{k'} h_f l_f u_{f,i} - u_{j,k'-\frac{1}{2}} \sum_{i=k'_b}^{k'-1} h_f l_f u_{f,i} \right) \Big] \tag{5.3}$$

and the velocity reconstruction procedure (3.22) reads as

$$\mathbf{u}_{c,k'} = \sum_f \delta_{f,c} d^c_f \frac{h_f l_f}{A_c h_c} u_{f,k'} \mathbf{n}_f \tag{5.4}$$

Here k' refers to the index of the sub–layer, not the actual layer.

Note that the sublayer 2 crosses two actual layers in the downwind column. In that case, the normal velocity component $u_{f,k'}$ is approximated as

$$u_{f,2'} = \frac{h'_{d,21}}{h'_{d,2}} u_{f,1} + \frac{h'_{d,22}}{h'_{d,2}} u_{f,2} \tag{5.5}$$

where $h'_{d,21}$ and $h'_{d,22}$ are the heights of the parts of the sub–layer 2 belonging to the actual layers 1 and 2 respectively, see Figure 5.3. Moreover, the same principle should be applied to the velocity reconstruction procedure (3.22)-(3.23) also used in the discretisation of the Coriolis term.

The two layer simulation of the dam break over wet bed described above was repeated using the advection discretisation given by Equation (5.3), the results are shown in Figure 5.4. As can be seen, the free surface elevation is represented at least as well as in the one layer case shown in Figure 4.4. The difference in the velocity norm between the two layers for the faces on one column side is exactly zero.

Simulation of a dam break over a dry bed as described in Section 4.2 was repeated using ten vertical layers located at $z = 0.1, 0.2, 0.3, ..., 0.9$ and $1.0m$ above the bed. The resulting surface elevation and velocity norm for the bottom layer (shown in Figure 5.5) are identical to that of the one layer simulation (Figure 4.5). The velocity norm for the other layers are equal to the velocity norm of the bottom layer in the locations where they are defined.

All the other experiments from Section 4.2 were also repeated with multiple layers using the advection scheme (5.3). The results are not shown here since they are, as expected, identical to the one layer case.

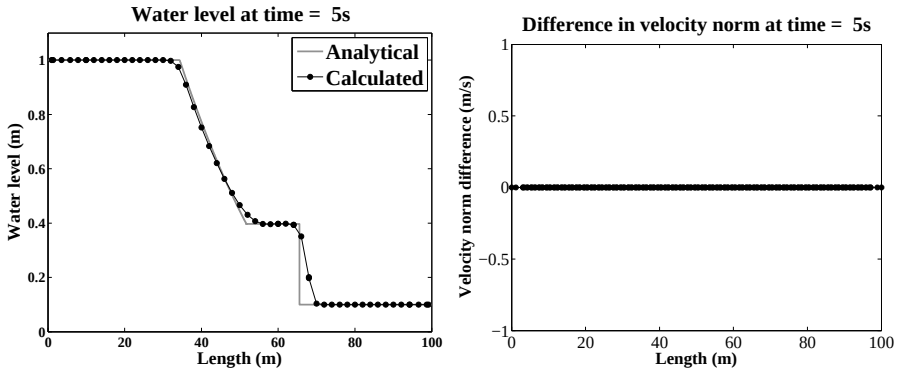

Figure 5.4: Dam break over wet bed: surface elevation (left) compared with the analytical solution (grey line) and the difference in velocity norm between the two layers.

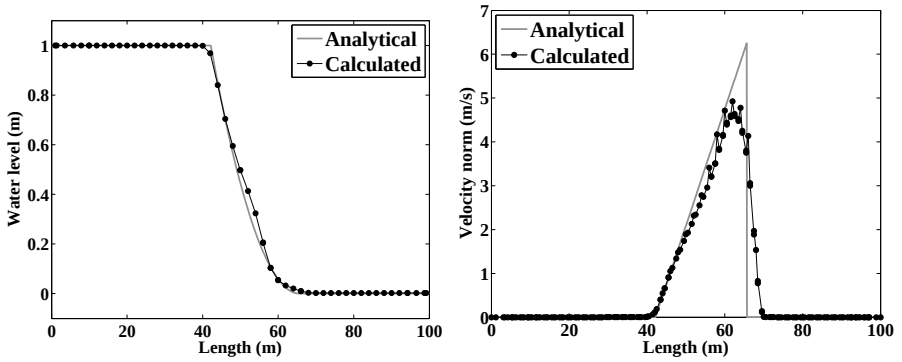

Figure 5.5: Dam break over dry bed: surface elevation (left) and the velocity norm for the bottom layer (right) compared with the analytical solution (grey line).

5.3 Test cases

5.3.1 Rotating basin with parabolic bathymetry profile and planar surface

Consider two dimensional flow in a circular basin with bathymetry profile described by a paraboloid of revolution given by

$$b = -b_0 \left(1 - \frac{x^2 + y^2}{L^2}\right) \tag{5.6}$$

where b_0 is the maximum depth of the basin. L is the radius of the equilibrium shoreline determined by the condition $b = 0$.

In such a basin a periodic flow with initially tilted planar free-surface is described as, see Thacker (1981)

$$\begin{aligned} u &= -\psi\omega \sin \omega t \\ v &= \psi\omega \cos \omega t \\ \eta &= \psi \tfrac{b_0}{L^2}(2x \cos \omega t + 2y \sin \omega t - \psi) \end{aligned} \tag{5.7}$$

where ψ and ω are the motion amplitude and frequency respectively. For a specified frequency $\omega > |f|$ the radius of the equilibrium shoreline is given by

$$L = \sqrt{\frac{2gb_0}{\omega(\omega + f)}} \tag{5.8}$$

with f being the Coriolis parameter.

Note that since u and v are independent of x and y the analytical solution (5.7) satisfies the linearized shallow water equations with the horizontal advection terms neglected.

The parameters b_0, f, ω and ψ are chosen to correspond to typical environmental flows. Namely, setting $b_0 = 50$m, a latitude of 45° North and $\omega = 2\pi/(12 \times 36)$ results in the wave period T of 12 hours and the equilibrium shore line $L = 164.735km$. The parameter $\psi = L/10$ is chosen. A crossection of the domain at $y = 0$ and $t = 0$ is shown in Figure 5.6.

The unstructured grid used for the simulation contains 17813 columns and 26874 column sides with edge lengths varying between approximately 4 and 6 kilometers. Note, that the chosen grid may influence the resulting numerical accuracy (see, for example Casulli and Walters (2000); Casulli and Zanolli (2005)). In contrast to Casulli and Zanolli (2007) the grid used here does not

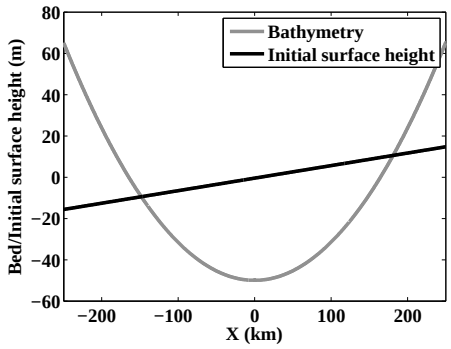

Figure 5.6: Slice through the domain at $Y = 0$.

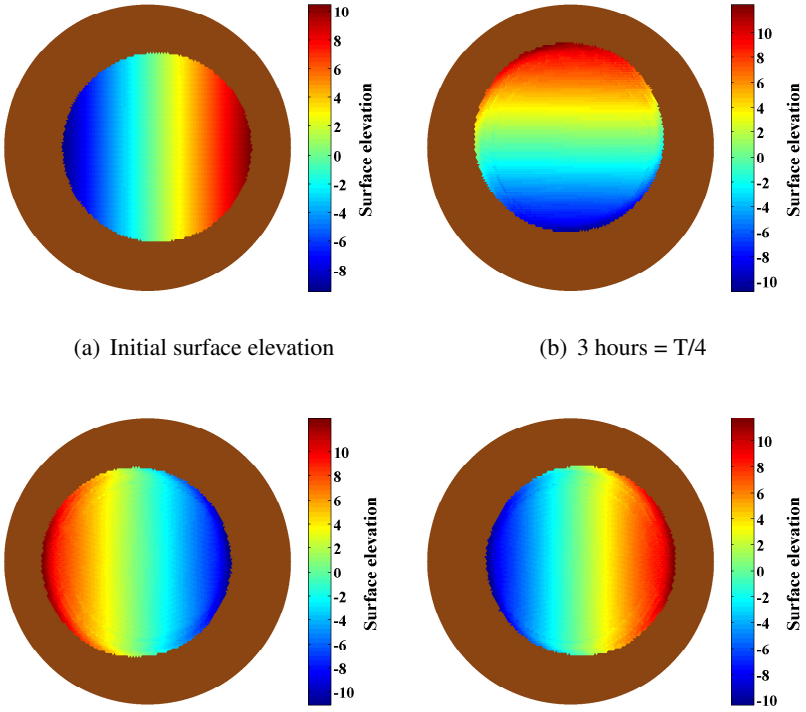

(a) Initial surface elevation

(b) 3 hours = T/4

(c) 6 hours = T/2

(d) 48 hours = 4T

Figure 5.7: Surface elevation of the periodic flow with an initially tilted planar free surface obtained using the layer remapping procedure.

account for the given bottom topography and for the expected flow field and, thus, makes the accurate solution more difficult to obtain.

The simulation was performed with a time step of 30 seconds using 5 layers with altitudes -15, -5, 0, 5 and $15m$. Figure 5.7 show the simulated surface elevation obtained using the layer remapping procedure by Kleptsova et al. (2010).

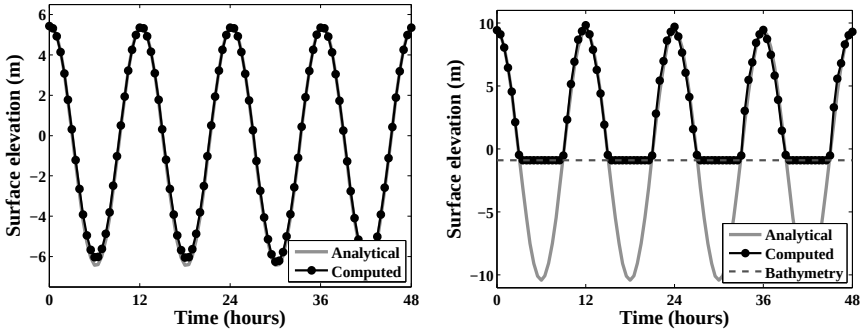

(a) $x \approx 100km$ (b) $x \approx L$

Figure 5.8: Comparison of analytical and simulated surface elevation time series at locations $x \approx 100km$ (left) and $x \approx L$.

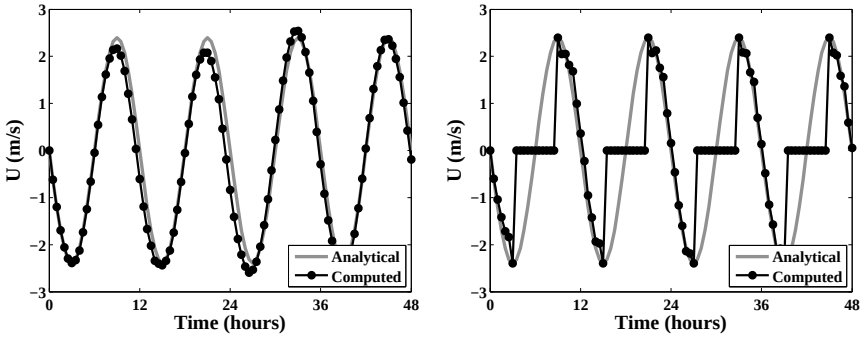

(a) $x \approx 100km$ (b) $x \approx L$

Figure 5.9: Comparison of analytical and simulated velocity time series at locations $x \approx 100km$ (left) and $x \approx L$.

Figure 5.8 shows surface elevation time series at x approximately equal to $100km$ and L compared to analytical solution. Time series for the $u-$component of velocity at the same locations are shown in Figure 5.9. Note,

that the location $x = L$ becomes dry during half period. The computed velocities and the total water depth is zero at this point since the model does not perform any calculations for the dry cells.

The analytical solution (5.7) does not, in fact, account for flooding and drying in the sense that it is assumes the surface elevation and velocity given by Equation (5.7) for the dry period as well. During the flooding phase the numerical solution is to be initialized with the analytical velocity field in order to obtain agreement with the analytical solution. If the newly flooded faces are initialized with zero velocities a slightly different period of oscillations is obtained as shown in Figure 5.10.

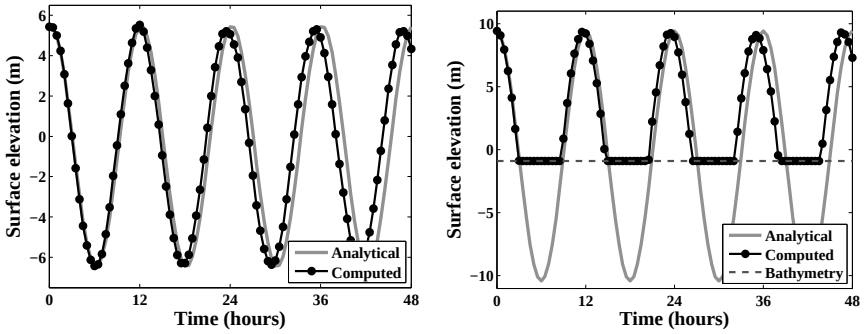

(a) $x \approx 100km$ (b) $x \approx L$

Figure 5.10: Comparison of analytical and simulated surface elevation time series at locations $x \approx 100km$ (left) and $x \approx L$ obtained while initializing the newly flooded faces with zero velocities.

The analytical solution given by Equation (5.7) represents a severe test case. The major difficulty arises from the absence of bottom friction and horizontal viscosity which have a stabilizing effect on the numerical solution when properly discretized. It demonstrates that the model is able to correctly handle Coriolis force in the multiple $z-$layer case.

5.3.2 Solitary wave run-up on a conical island

The laboratory experiment was performed by the Coastal and Hydraulics Laboratory of the USACE. The physical model of the conical island was constructed in the center of a $30m$ wide by $25m$ long flat-bottom basin, schematically shown in Figure 5.11. The island had the shape of a truncated, right circular cone with the diameters of $7.2m$ at the toe and $2.2m$ at the crest.

The height of the island was $62.5cm$. The water depth in the basin was set to $32cm$. A wave maker was installed along the $x-$axis. Twenty-seven wave gauges were used to measure surface wave elevation. The data series for seven of these gauges (1-4, 6, 9, 16, 22) are freely available. The first four gauges measuring incident wave conditions were located parallel to the wave maker at a distance of a half-a-wavelength from the toe of the island. The data series for the gauge 4 was used to calibrate an analytical solution of a solitary wave which acted as the boundary condition.

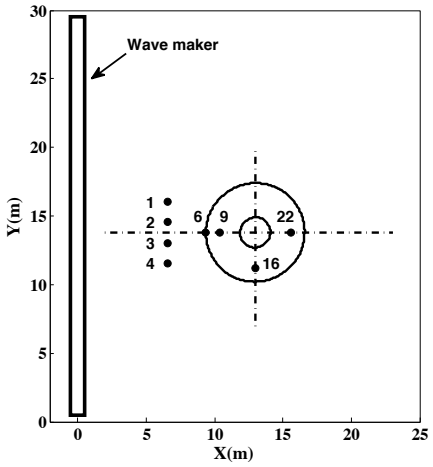

Figure 5.11: Solitary wave run-up on a conical island: top view of the wave basin with the island and the locations of the wave gauges.

The unstructured grid used for the simulation has 55338 columns and 83367 column sides with lengths varying from $24cm$ at the boundary of the domain to $4cm$ at the crest of the island. The simulation was performed using the time step of 0.001 second. Figure 5.12 shows the numerical solution obtained using 4 layers in the vertical at time $t = 7.5$, $t = 8.5$, $t = 10$ and $t = 12.5$ seconds. When approaching the island the solitary wave shoals (see Figure 5.12(a)) and bends around the island due to refraction and diffraction (Figure 5.12(b)). The partial reflection of the wave causes a depression at the front of the island, Figure 5.12(c). The two bent sides of the wave meet at the back of the island (see Figure 5.12(d)) where a larger run up is induced.

Figure 5.13 shows the measurement at gauges 6, 9, 16 and 22 compared to the numerical results. The model represents the arrival time and the height of the incoming wave quite well. The computed surface elevations are actually somewhat larger than were measured. This discrepancy is very likely due to

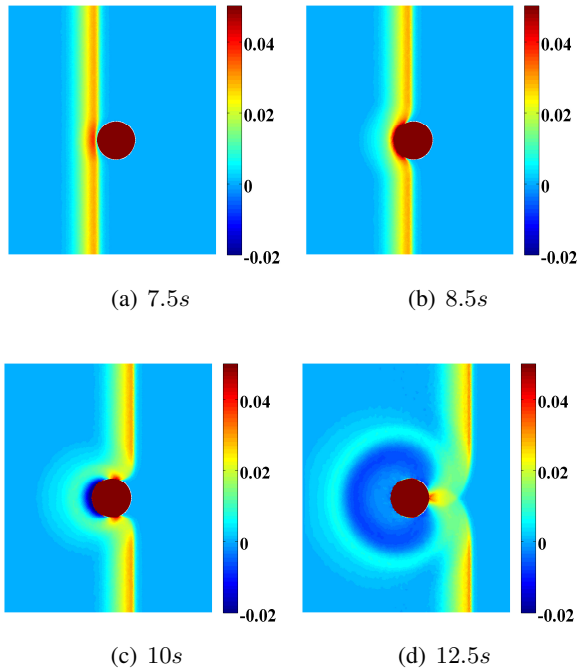

(a) $7.5s$ (b) $8.5s$

(c) $10s$ (d) $12.5s$

Figure 5.12: Solitary wave run-up on a conical island: numerical solution at time (a) $t = 7.5$, (b) $t = 8.5$, (c) $t = 10$ and (d) $t = 12.5$ seconds.

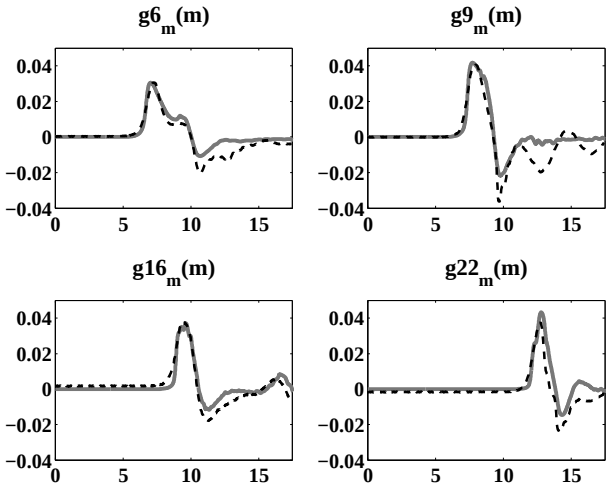

Figure 5.13: Solitary wave run-up on a conical island: measured (dashed line) and numerical (solid line) surface elevation time series at the indicated wave gauges against time (s).

dissipative effects, which are not accounted for in the model. The results can be improved by using a non-hydrostatic model, see for example Cui et al. (2012).

The reflected wave and the wave interactions are not well predicted, as can be seen the trough is shallower than indicated by the measurements. This is, however, consistent with other runup model tests Chen et al. (2000); Lynett et al. (2002); Fuhrman and Madsen (2008). According to Kanoglu and Synolakis (1998), a possible reason for than is that the front surfaces of the experimental solitary wave profiles were generated more accurately than the rear, which also included a spurious tail.

5.3.3 Outflow from a basin with a reservoir

A basin $13800m$ long and $1200m$ wide was assumed to have a uniformly sloping bed with a depth of 5 m at the open boundary and zero at the other end, where it is closed. A reservoir formed by a local maximum of the bottom level at $x = 9000m$, see Figure 5.14. The initial surface elevation is set to the level of 2.0 meters. The basin is emptied in 100 hours by effect of the cosinusoidal depletion $\eta = 2\cos(\frac{\pi}{360000}t)$ of the downstream water level. The simulation was performed using four layers with altitudes $z = -3, -1.5, -0.5$ and $2.5m$

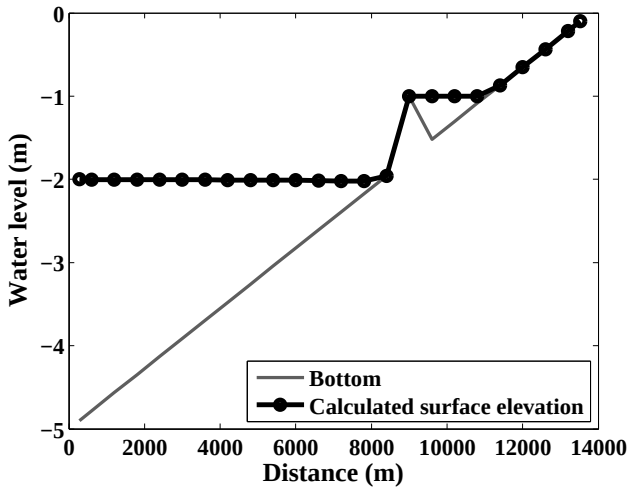

Figure 5.14: Simulation of the outflow from a basin with reservoir.

If the model conserves mass during the drying process, then the water level in the reservoir should asymptotically reach the local maximum bottom elevation. As is shown by Balzano (1998) this simple test case can be quite problematic

for some flooding and drying algorithms. Depending on the definition of the water depth at a side between two cells the reservoir fill level can be quite lower or even unrealistically higher than the local bathymetry maximum. Figure 5.14 shows that the reservoir fill level is precisely equal to the local maximum bottom elevation. That is, a model with the layer definition given in Section 5.2 is capable of conserving the mass of a wet area enclosed by the dry area.

5.4 Discussion

It is shown here that special attention is required to the discretisation of the momentum equation in the presence of multiple $z-$layers. It is a common practice to vary only the thickness of the top and bottom layers to represent the free surface and bathymetry variation. The thickness of the internal layers which do not contain the free surface and bed are kept constant. The heights of the faces for these layers are usually defined to be equal to the heights of the layers, thus replicating the flat bed case. This, however, generates a staircase problem which leads to inaccurate solutions and may erroneously introduce vertical structure in the flow.

A model must not create a vertical structure in the flow if there is no physical reason for that. Therefore the discretised momentum equation for a particular layer should be identical to that of any other layer, if phenomena such as bottom friction, viscosity, diffusion are disregarded. This means that heights of any two cells sharing a face should have the same ratio as the respective column heights. In addition, the ratio of the cells' face heights should be the same as the ratio of the heights of the column sides. Here is is proposed to locally redefine/remap cells and faces in such a way that the above mentioned conditions are fulfilled. The remapping procedure allows us to always have equal number of (sub)cells to the left and to the right of a particular column side, thus removing the discontinuities associated with the representation of the free surface and bathymetry as a series of steps. It also allows us to simulate flooding and drying phenomena in the presence of multiple $z-$layers.

In C-grid models a discretisation of the Coriolis force becomes an additional source for the staircase problem (see Figure 5.2), since this class of models only solves for the component of velocity normal to a face and the tangential component is interpolated. Therefore, the same layer remapping procedure should be applied while reconstructing the tangential velocity in order to prevent the model from the creating artificial vertical structure due to the discretisation of the Coriolis term in the presence of multiple $z-$layers.

6

Tides in the North Sea

Development of an accurate coastal shelf model is not only an important but also challenging problem. Such a model should be able to describe hydrodynamics both of the deep ocean and the shelf region. It should also capture the physics of the shelf break region: complex bathymetry, intensification of tidal currents near the shelf edge, nonlinear interactions with the steep bathymetry etc. This requires a very high spacial resolution in the shelf break region. However, using a very fine grid in regions whose detailed structure is of less interest is a highly inefficient use of computational resources. To be able to resolve the coast accurately while modeling the sea at acceptable cost, it is therefore necessary to vary the grid resolution in space.

It is a common approach to employ a hierarchy of nested grids with increased resolution in the area of interest. This is only partially satisfactory since the dynamics of the shelf break region and, consequently, the exchange between the shelf and the deep ocean is generally not properly represented.

Alternatively it is possible to use unstructured meshes which allow for a smooth transition from a very high to very low resolution within the same grid. In addition, since coastal flows are strongly influenced by the shape of the coastline, it is important that flow artifacts introduced by the presence of grid corners on the coast be avoided.

The results presented here are the first steps towards creation of a fine resolution European continental shelf model. Here the tidal motion in the North Sea which is the dominant feature in the dynamics of that area is focused on.

6.1 Dynamics of the North Sea

The dominant feature in the dynamics of the North Sea is the tidal motion, Otto et al. (1990). Tidal data are available from many locations along the coasts, some of them from the beginning of the 19th century. On the basis of these observations tidal predictions are made for a great number of stations. Open-sea measurements of adequate quality and duration are of more resent years.

The harmonic method of tide prediction that is widely in use is based on the linear superposition of different tidal components. Each of the components generated by the dynamic response of the sea area to external forcing at the specific, astronomically determined, periods.

The first co-tidal M2 map of the North Sea, based solely on observations, was published by Proudman and Doodson (1924). The chart shows three amphidromic points: one at 56N, at the eastern tip of the Dogger Bank, one near the entry of the Southern Bight and one, probably degenerate, at the Southern tip of Norway.

The M2 tide in the North Sea is generated by the co-oscillation of this (sub)basin with the Atlantic Ocean, and further amplified internally. The conceptual behavior of such a coastally trapped wave was first theoretically explained by Taylor (1922) who approximated the North Sea, with exception of the Southern Bight, by a semi-closed rectangular channel. Taylor (1922) shows that the incoming Kelvin wave propagates in opposite direction along the other side of the channel and thus, by interfering with the incoming wave, created a series of amphidromic points with the elevation amplitude increasing exponentially to the coast.

The predominant semi-diurnal lunar tide M2 gives a good first approximation of the tidal motion in the North Sea. It is however important to consider the interaction between tide and topography which occur at many places in the North Sea at all length scales, Houbolt (1968). Linear sand ridges in certain areas of the Southern Bight create separate areas of ebb- or flood dominated flow (residual currents). Together with residual currents higher harmonics (overtides) in the current velocity field are generated, Zimmerman (1981); Robinson (1983). M4 constituent, which is usually the most important, can create a significant asymmetry in the ebb- and flood stages of the tidal current so that the peak ebbspeed may differ from the peak flood speed. Enhancing any asymmetry which may already be present due to the residuals this creates a situation that is favorable for net sediment transport.

The temperature variation in the North Sea is primarily determined by the heat flux through the sea surface and the vertical exchange of heat in the water column underneath. During periods of heating stratification may develop in some regions and only the upper layer is warmed up, whereas in other regions the temperature remains homogeneous form surface to bottom.

The determining factor of occurrence or absence of stratification is the balance between potential energy gain and kinetic energy loss by mixing in the presence of buoyancy flux. It was indicated that stratification depends on the cube of the tidal current velocity amplitude $|u|^3$ and the bottom depth h. More precisely the dependence is on the ratio $h/|u|^3$, as indicated by Simpson and Hunter (1974). For conditions where $h/|u^3|$ is high, stratification may develop at certain values of the heat flux, and where $h/|u|^3$ is below a given value, mixing occur up to the surface. So for shallow depths and strong tidal currents, typical for most coastal regions and for the southern North Sea complete mixing may be expected.

6.2 Model parameters and boundary settings

The simulations were performed using two orthogonal grids of different resolution having common open boundaries. The coarse grid, shown in Figure 6.1, consists of about 131000 triangular elements and is the orthogonal variant of the grid used by Ham (2006) The longest mesh sides present in the mesh are approximately $20km$ long. The resolution increases as a function of distance from the coast so that much of the coastal zone is resolved with a resolution of approximately $5km$ and the coastal resolution is approximately $1km$. The fine grid consists of almost 400 thousands nodes with 80% of the nodes located in the area contained within the dark grey rectangle shown in Figure 6.1. The number of element for the fine grid is just under 690000. The minimum resolution in the Dutch coastal zone is approximately $10m$. Figure 6.2 shows the part of the grids contained in the light grey rectangle from Figure 6.1. The part of the fine grid around Rotterdam harbor area (grey rectangle in Figure 6.2) is shown in Figure 6.3.

The simulation is driven solely by the surface elevation on the Atlantic boundaries. The data used was that used in DCSM98. There are 27 ”tidal” points along the boundary for which the tidal spectrum is specified. Then for the boundary points $\mathbf{x}$ between the two ”tidal” points with coordinate vectors $\mathbf{x}_1$

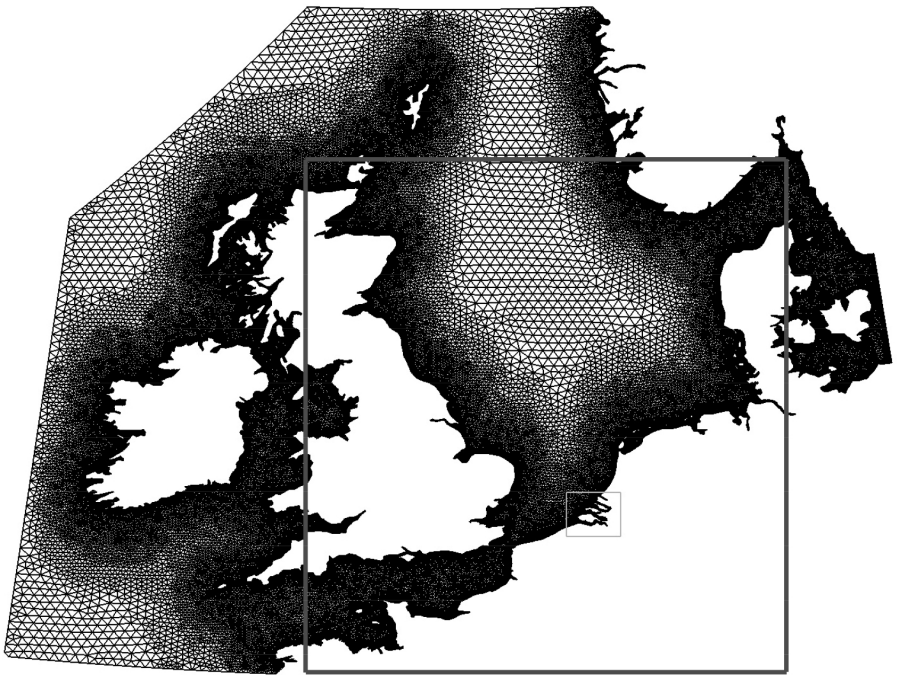

Figure 6.1: The unstructured grid used in the simulations. The mesh resolution varies from $20km$ to $1km$.

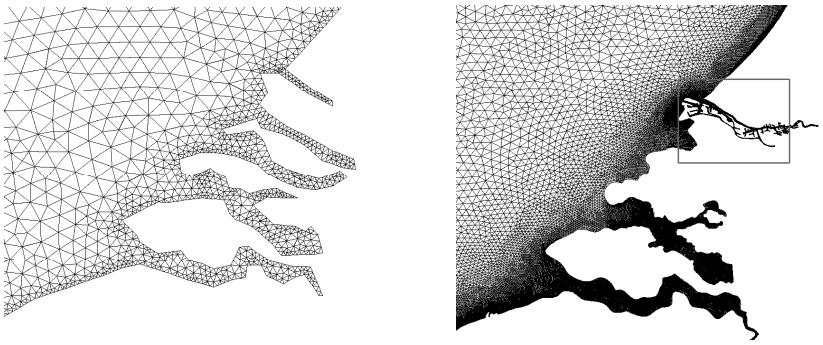

Figure 6.2: Part of the coarse (left) and fine (right) grids.

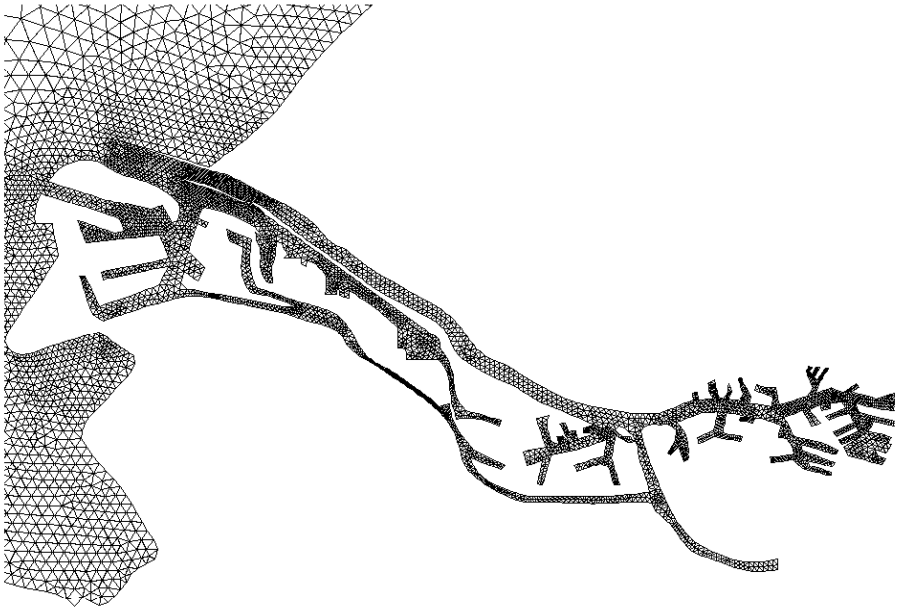

Figure 6.3: Part of the fine unstructured grid used in the simulations. The mesh resolution varies from $20km$ to $10m$.

and $\mathbf{x}_2$ the spectrum $\mathbf{s}(\mathbf{x}) = \{h_i(\mathbf{x}), \alpha_i(\mathbf{x})\}$ is specified as

$$\mathbf{s}(\mathbf{x}) = \frac{(\bar{\mathbf{x}}_2 - \bar{\mathbf{x}}) \cdot (\bar{\mathbf{x}}_2 - \bar{\mathbf{x}}_1)}{||\bar{\mathbf{x}}_1 - \bar{\mathbf{x}}_2||^2}\mathbf{s}(\mathbf{x}_1) + \frac{(\bar{\mathbf{x}} - \bar{\mathbf{x}}_1) \cdot (\bar{\mathbf{x}}_2 - \bar{\mathbf{x}}_1)}{||\bar{\mathbf{x}}_1 - \bar{\mathbf{x}}_2||^2}\mathbf{s}(\mathbf{x}_2) \tag{6.1}$$

Then the surface elevation is calculated as

$$\eta(\mathbf{x}) = \sum_i h_i(\mathbf{x}) \cdot cos\left(\frac{2 * \pi}{T}t - \alpha_i(\mathbf{x})\right) \tag{6.2}$$

The bathymetry used was that of the existing DCSN98 structured mesh. This has the drawback that the bathymetry was already downsampled to the $8km$ resolution. This is particularly an issue in the coastal region where the additional coastal features resolved by the model may be recorded as dry or with bathymetries with a very large relative error. On the other hand, the publicly available bathymetry data also has limitations. In addition, the bathymetry used has been heavily tuned to the DCSM8 model including to correct for the poor resolution of the Straits of Dover Gebraad and Philippart (1998).

Since modification of the bottom friction parameters is not available in Delfin, a single relatively low roughness length of $1cm$ was specified for the entire domain. The implicitness parameter θ was set to 0.55 and a time step of $10min$ for the coarse grid and $5min$ for the fine grid was chosen. At almost 75 time steps (150 for the fine grid) per tidal cycle, the M2 tide is thus well resolved in time. The latitude used in the calculation of the Coriolis parameter was set to 55° which is a reasonable value for the Southern North Sea although a variable value would clearly be preferable. The simulation was conducted with a single layer in the vertical.

6.3 Results

6.3.1 Estimation of M2 tide characteristics

For this initial simulation only the diurnal lunar (M2) component of the tide was specified along the open boundary. This component of the tide is one for which observations are available.

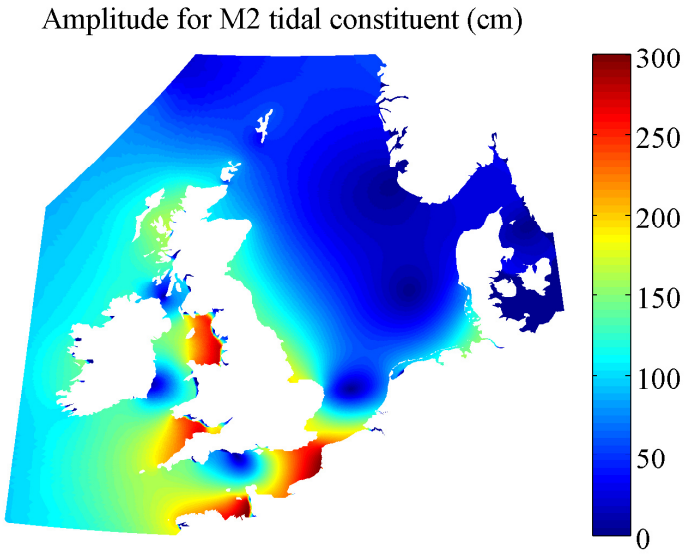

Figure 6.4: Amplitude (cm) of M2 tidal constituent calculated using the fine grid.

The basic characteristics of the tidal wave are that it is driven by a periodic surface displacement in the North Atlantic which progresses from South to

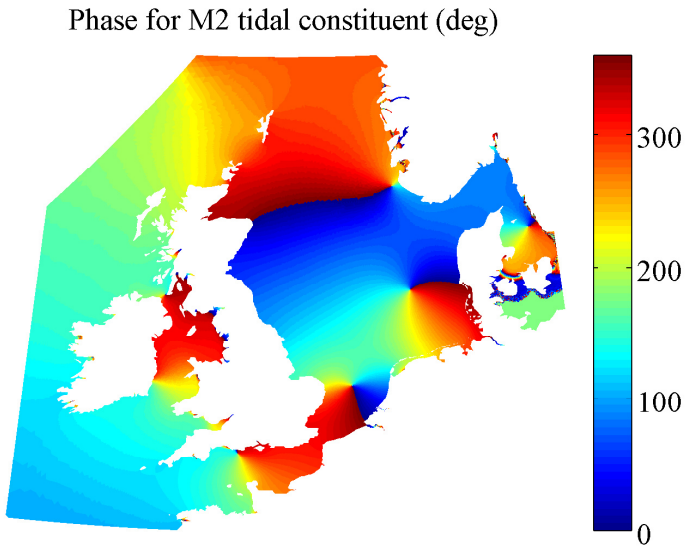

Figure 6.5: Phase (degrees) of M2 tidal constituent calculated using the fine grid.

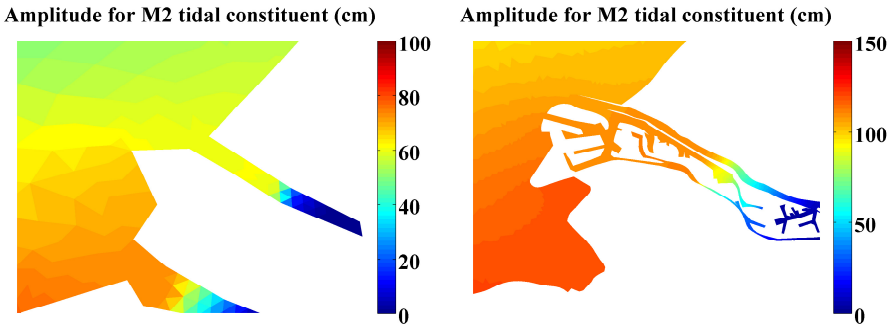

Figure 6.6: Amplitude (cm) of M2 tidal constituent in the Rotterdam harbor area calculated using the coarse grid (left) and fine grid (right).

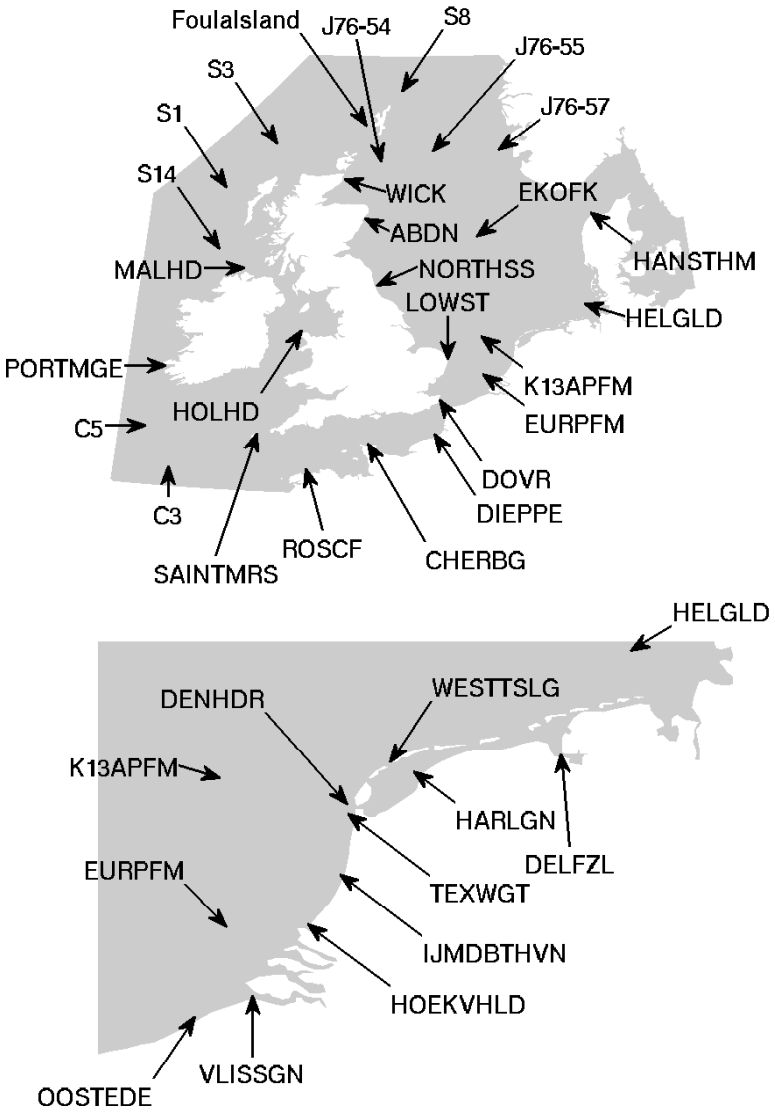

Figure 6.7: Approximate locations of the stations at which tidal observations were available for comparison.

North along the domain boundary. Inside the domain, this causes a wave to progress up the English Channel and back each tidal cycle. More significantly, a Kelvin wave is generated which passes in an anticlockwise direction down the British coast and along the Dutch coast towards the Denmark. Figure 6.4 and 6.5 show a visual representation of the tidal phase and amplitude in the entire domain. Figure 6.6 shows a detailed view of the M2 tide amplitude in the Rotterdam harbor area calculated using both coarse and fine grid.

To evaluate the outcome of the simulation conducted, part of the data presented in Gebraad and Philippart (1998) is used. The observed M2 tide at the points shown in figure 6.7 is compared with the available results of the model. Tables 6.1 and 6.2 show the observed and computed data for each of the data sources together with the relative error. For 75% of the stations the calculated amplitide is within $20cm$ difference from the observed one. The maximum amplitude error of $40cm$ for the coarse grid and $56cm$ for the fine grid is encountered at CHERBOURG and ROSCOFF stations respectively. The phase error is less than 10 degrees for 58% (21 out of 36) stations. The maximum phase error of 52 and 56 degrees for the coarse and the fine grid respectively is encountered for DELFZIJL station.

As can be seen, the degree of inaccuracy varies in space. Generally, away form the North Sea coast, both the phase and amplitude of the Delfin results close to the observations. There is a structural lagging phase error evident in the Delfin results, which, at least in the deeper areas, is a little surprising since the M2 tidal wave should be well resolved in space and time by the given parameters. As the tidal wave passes down the East coast of the United Kingdom there is an immediate amplitude loss which generally increases as the wave progresses.

The loss of amplitude and phase occurs largely in the shallowest areas traversed by the tidal wave. This suggests that the effective dissipation in these areas is excessive, hence some combination of tuning the bed friction parameters and better bathymetry and coastal data might produce substantially better results.

On the other hand, the high Courant numbers with maximum of about 30 in the shallowest areas could also give rise to the inaccuracies, see Ham et al. (2005).

6.3.2 Estimation of M4, M6 overtide characteristics

The model was forced with eight major tidal constituents, namely with semidiurnal tides M2, S2, K2 and N2 and diurnal tides K1, O1, P1, Q1 in order to take account of spring-neap variations. The shallow water tides M4, M6 were

Station name	Observed amplitude	Amplitude (cm)	
		coarse grid	fine grid
J76-57	24.5	15,82	18,24
J76-55	50	32,84	34,56
J76-54	66.6	52,3	54,53
WICK	101.1	83,77	85,65
ABERDEEN	131.1	101,57	102,58
NORTHSHIELDS	158.1	126,1	126,26
LOWESTOFT	70.36	69,11	63,08
DOVER	225.32	191,73	179,94
CHERBOURG	187	146,73	139,66
DIEPPE	313	284,14	276,46
OOSTENDE	179.56	163,48	165,24
HOEK VAN HOLLAND	77.97	78,84	81,19
IJMUIDEN	67.5	67,95	66,72
DEN HELDER	65.08	71,93	68,36
HELGOLAND	108.6	97,93	85,86
FOULA ISLAND	54.3	47,52	47,79
PORT-MAGEE	117.5	117,22	116,62
EKOFISK	28	28,12	25,36
WESTGAT	65.43	71,13	57,00
S3	92.7	83,03	83,28
S1	108	101,56	100,15
S8	55.3	48,76	49,35
S14	112.4	113,67	114,16
C3	115.7	112,94	113,29
C5	111.6	106,16	106,34
SAINT MARYS	176.5	162,66	163,24
MALINHEAD	107.5	124,77	124,09
HANSTHOLM	12.2	29	20,99
STATION K13A	53.23	52,65	47,47
STATION EURO 0	72.94	66,04	67,77
ROSCOFF	269	229,17	213,05
HOLYHEAD	181	171,22	171,78
HARLINGEN	82.98	89,34	83,03
DELFZIJL	134.72	111,55	98,13
VLISSINGEN	174.21	145,7	143,89
WEST-TERSCHELLING	79.8	82,33	74,88

Table 6.1: M2 tidal amplitude observed at stations around the North Sea and calculated using Delfin.

Station name	Observed phase	Phase (degrees)	
		coarse grid	fine grid
J76-57	286.00	281,14	283,13
J76-55	318.00	319,01	315,07
J76-54	323.00	322,55	320,16
WICK	322.20	330,5	327,97
ABERDEEN	25.10	26,42	24,67
NORTHSHIELDS	89.00	85,69	86,60
LOWESTOFT	259.90	237,08	238,22
DOVER	331.90	313,98	317,18
CHERBOURG	230.00	230,76	231,49
DIEPPE	310.00	301,32	299,51
OOSTENDE	5.30	342,86	345,75
HOEK VAN HOLLAND	56.40	41,31	40,08
IJMUIDEN	100.30	77,99	75,25
DEN HELDER	162.40	137,77	135,60
HELGOLAND	312.00	281,71	290,62
FOULA ISLAND	264.00	256,92	257,58
PORT-MAGEE	123.00	122,52	123,06
EKOFISK	85.00	75,86	74,85
WESTGAT	148.60	130,38	149,17
S3	205.00	202,93	203,04
S1	179.00	176,92	178,23
S8	283.00	280,54	280,91
S14	163.00	161,42	161,68
C3	107.00	107,41	107,64
C5	116.00	115,13	115,06
SAINT MARYS	130.10	130,87	128,44
MALINHEAD	177.70	166,12	166,78
HANSTHOLM	105.00	69,77	68,73
STATION K13A	176.60	160,93	161,55
STATION EURO 0	25.70	5,58	8,24
ROSCOFF	142.00	135,98	135,48
HOLYHEAD	291.00	291,63	291,24
HARLINGEN	249.00	200,75	206,10
DELFZIJL	305.00	252,85	248,53
VLISSINGEN	30.50	357,85	20,30
WEST-TERSCHELLING	219.10	186,75	181,24

Table 6.2: M2 tidal phase observed at stations around the North Sea and calculated with Delfin.

generated on the shelf.

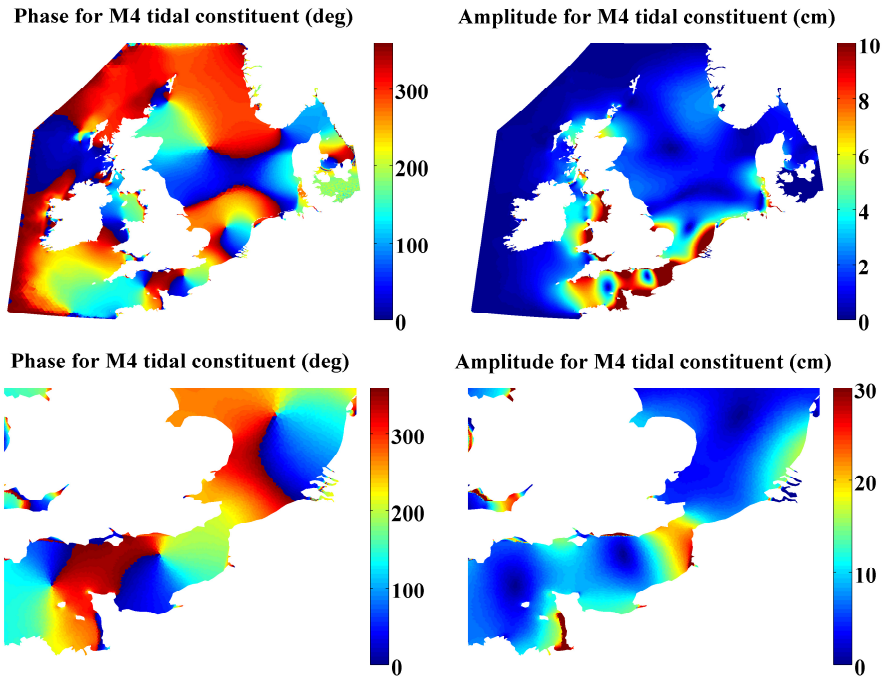

Figure 6.8: Phase (left) and amplitude (right) of M4 tide in the whole domain (top) and the detailed view in the English channel (bottom) calculated using the coarse grid.

Figure 6.8 show a visual representation of the tidal phase and amplitude in the entire domain for M4 tidal constituent together with the detailed view in the English Channel. M4 is clearly generated within the shelf seas and its amplitude decreases rapidly at the shelf edge. Maximum amplitude of about $0.4m$ are observed in the Severn Estuary, Wash and Gulf of Saint-Malo. Amplitude up to $0.3m$ occur in the Dover Strait where there is an anti-amphidrome. Over the rest of the shelf seas the amplitude is less then $0.1m$. Amphidromes occur off southeast Ireland, in the Southern North Sea and twice in the English Channel.

Tidal amplitude and phase of the M6 constituent for the whole domain and the detailed view in the English Channel is depicted in Figure 6.9. The results show two amphidromes in the Southern North Sea and two in the English Channel. The computed M6 cotidal chart Figure 6.9 shows a rapid increase in tidal amplitude in shallow water due to an increase in bottom friction and reaches its maximum in the Strait of Dover. The M6 amplitude seem to be

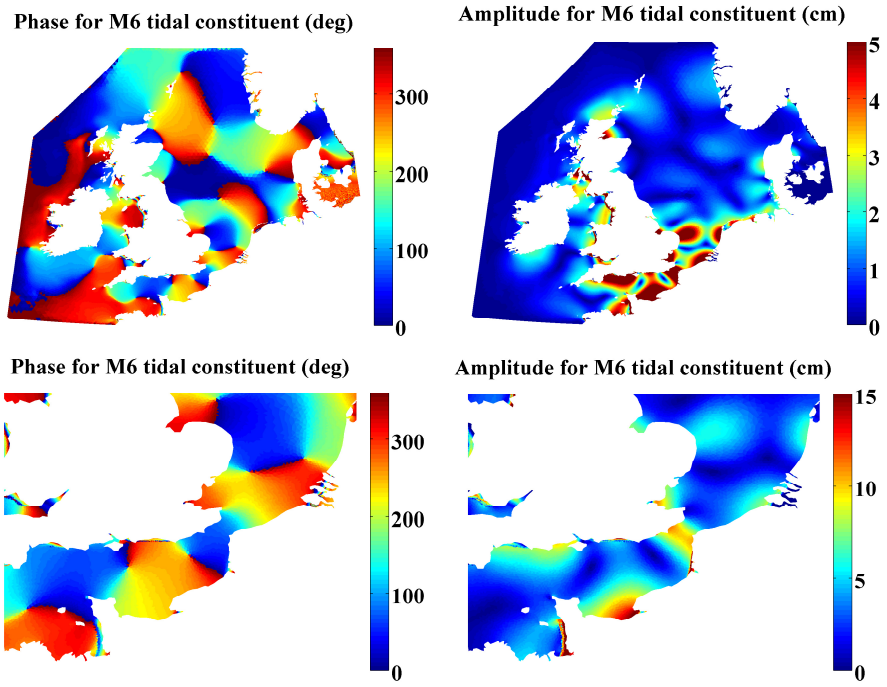

Figure 6.9: Phase (left) and amplitude (right) of M6 tide in the whole domain (top) and the detailed view in the English channel (bottom) calculated using the coarse grid.

overestimated by the model, the possible reason for that could be the purely resolved bathymetry.

The water level driven by the eight tidal constituents is presented in Figure 6.10 and Figure 6.11 for the Harlingen station. The Figure 6.10 clearly shows spring-neap variation of the water level. As can be seen form Figure 6.11 the rising water period is shorter than the falling water period for the station. The tidal asymmetry is the result of the interaction of the M2 and M4 tidal components.

6.3.3 Estimation of stratification parameter

It is well known that tidal currents play an important role in determining the amount of stratification in coastal seas. Simpson and Hunter (1974) proposed a simple criterion for the separation of well-mixed and stratified regions. The separation occurs for a particular value of the ratio of the potential energy required for perfect vertical mixing to the rate of dissipation of energy by the

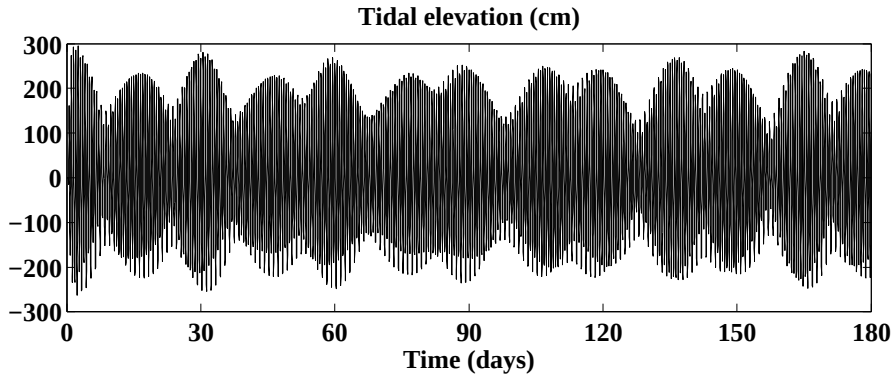

Figure 6.10: Modeled tidal elevation at Harlingen station.

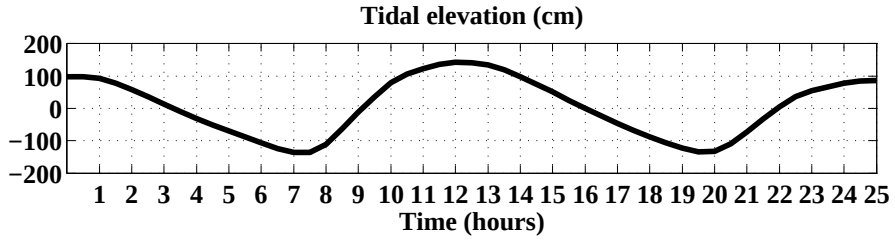

Figure 6.11: Flood-ebb asymmetry at Harlingen station.

tidal currents. Therefore the relevant parameter for the separation of mixed and stratified regions is $h/|u_s|^3$, where h denotes the water depth and u_s is the depth averaged tidal stream velocity amplitude.

An important factor to be considered is the variability of frontal positions due to tidal advection and spring-neap adjustment. The simulated velocity field was used to estimate the stratification parameter S as defined by Pingree and Griffiths (1978)

$$S = \log_{10}\left(\frac{h}{C_d|u_s|^3 10^4}\right) \tag{6.3}$$

with the bottom drag coefficient C_d set to 0.0025. Factor 10^4 is added to convert to cgs units.

The resulting value of the stratification parameter for spring and neap tides is shown in Figure 6.12. The well mixed areas with corresponding $S < 1$ are shown in black. Seasonally stratified regions with $S > 2$ are plotted in grey. Different shades of red correspond to the transitional areas for which values of

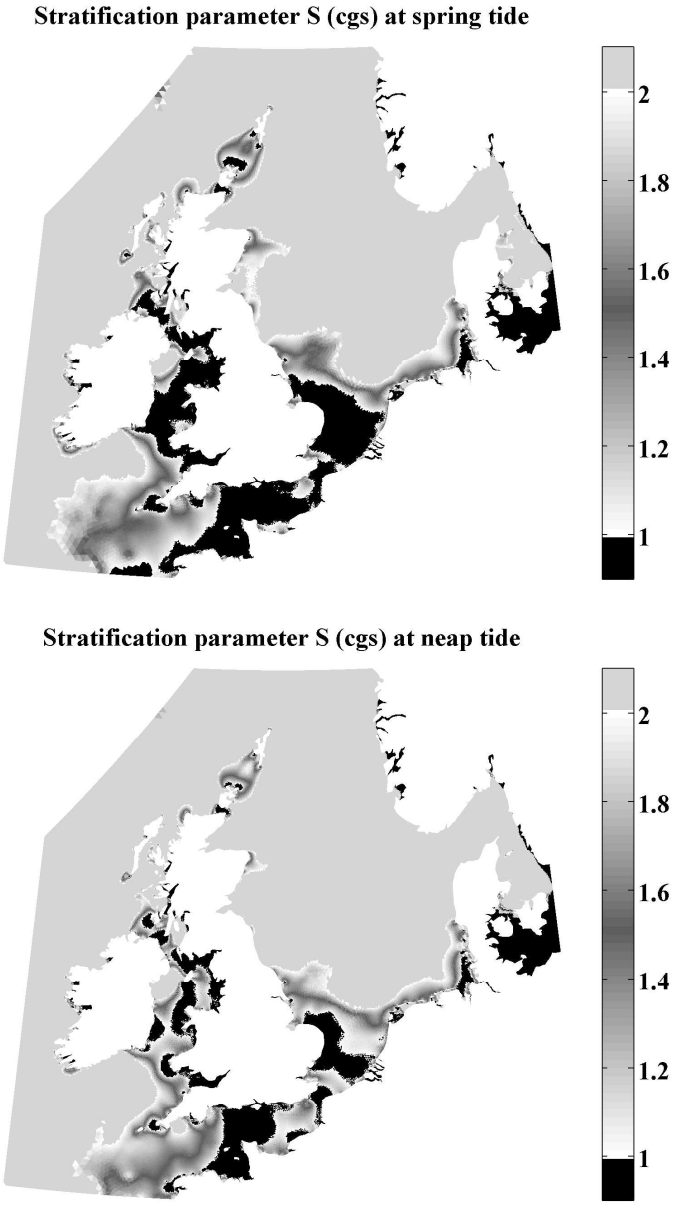

Figure 6.12: Predicted position of frontal boundaries at spring tide (top) and neap tide (bottom). Stratified condition ($S > 2$) are shown in medium grey, region that are well mixed ($S < 1$) are shown in black. Transitional areas ($1 \geq S \leq 2$) are represented by shades of grey.

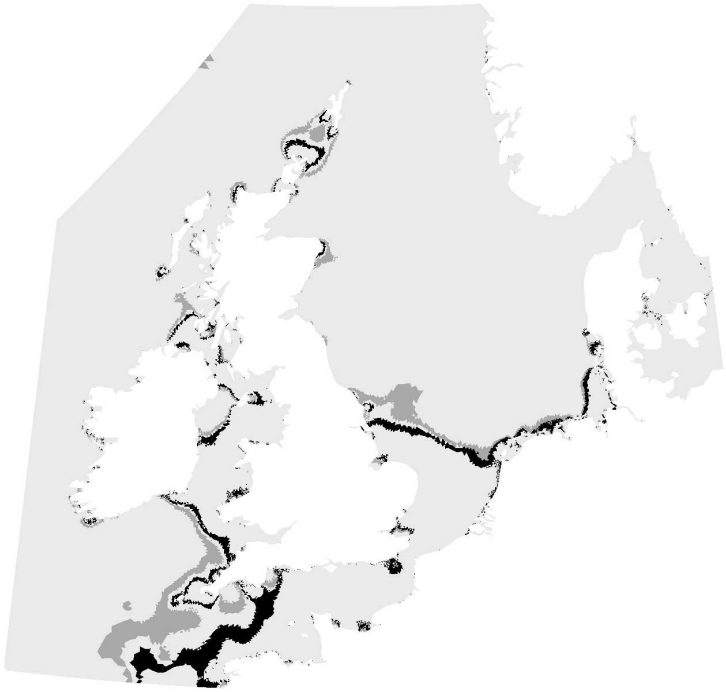

Figure 6.13: Predicted position of frontal boundaries at spring tide (grey) and neap tide (black).

S vary between 1 and 2 cgs units with the critical value of $S = 1.5$ being the darkest. The Figure 6.13 shows the predicted positions of frontal boundaries at spring tide (shown in grey) and at neap tide (shown in black).

6.4 Discussion

The development of operational numerical models has contributed considerably to the understanding of the circulation of the North Sea. Using unstructured grids suggest a number of advantages to numerical ocean circulation modeling. In particular, they are geometrically flexible and allow for continuous coastline and variable resolution. This allowed inclusion of river estuaries which play an important role in freshwater and sediment transport in the southern North Sea.

In coastal regions the tidal range is generally larger than in the open ocean, and

the tidal waves are considerably more complex. Shallow-water constituents are caused by the nonlinear interaction of the astronomical semidiurnal and/or diurnal constituents when the tidal wave propagates over the shelf. Therefore, important considerations in the numerical modeling of tidal dynamics are the capture of nonlinear interactions.

Fully calibrating a continental shelf model requires extensive tuning preferably using data assimilation techniques. Results presented here are preliminary results which are the first steps towards development of a 3D multiconstituent high resolution model for the southern North Sea. Although the model is completely uncalibrated it was able to correctly capture the essential characteristics of the M2 tide, which gives a good first approximation of the tidal motion in the North Sea, and of the most important nonlinear shallow water overtides M4 and M6 which have double and triple the frequency of M2. The simulated velocity field is used to evaluate the Simpson-Hunter stratification criterion and the spacial variation of the frontal boundaries due to spring-neap adjustment.

7

The Indian Ocean Tsunami

Note. The content of this chapter is based on the the following paper: *Kleptsova et al. (2012)*, *On a momentum conservative z-layer unstructured C-grid ocean model with flooding* .

Recent studies show that four of the ten most deadly earthquakes and tsunami events since 1701 occurred in the last decade, Dunbar et al. (2010). The 2004 Sumatra earthquake and tsunami killed approximately 228 thousand people across 14 countries. The fifth largest earthquake was recorded in Chile in February 2010 and generated a drastic tsunami. The 2011 Tohoku earthquake, the most powerful known earthquake to hit Japan and one of the five most powerful earthquakes ever recorded, generated a devastating tsunami which in addition to more than 16 thousand deaths, caused a number of nuclear accidents. These tragic events show the importance of understanding earthquake and tsunami hazards in all regions of the world.

Along the coast, storm surge is often the greatest threats to life and property, NOAA (2010). This rise in water level can cause extreme flooding in coastal areas particularly when storm surges coincide with normal high tide, resulting in storm tides. The 1953 North Sea storm surge killed more that 2000 people in the Netherlands, England and Belgium. Hurricane Katrina (2005) is another example of the damage and devastation that can be caused by storm surge, at least 1500 persons lost their lives and many of those deaths occurred directly as a result of the storm surge.

With the increasing population density in coastal regions more people are placed at risk due to the size and nature of cities. Therefore, an essential aspect of disaster risk reduction is to have detailed inundation and flooding maps for a particular area.

The major difficulty with tsunami modeling lies in determining of a precise fault mechanism. A number of studies on the rupture process of the 2004 Sumatra-Andaman earthquake has been done using GPS and seismic data. The co-seismic displacement data are then validated using the results of tsunami models which are compared to a number of independent data sources. In Tanioka et al. (2006) the rupture process has been estimated by tsunami wave forms at tide gauges. In Pietrzak et al. (2007) and Hoechner et al. (2008) the satellite altimetry data has been used to improve the estimates of the slip along a thrust-fault earthquake. However, non of the approaches resulted in consistent agreement of the modeling results to all of the available data sources. Flooding provides another measure with which to assess the rupture models. However, this requires accurate runup and inundation models.

To accurately model processes in the coastal ocean, and in particular to simulate flows in the shallow near shore region, including flooding and drying problems, it is important to employ a high resolution grid. By using unstructured grids it is possible to achieve highly variable resolution in complex geometries and thus to resolve accurately a particular regions of interest, while modeling other regions at an acceptable cost.

Tsunamis are long surface gravity waves generated by rapid displacement of the sea surface. The Indian Ocean Tsunami of 26 December 2004 was driven by a massive earthquake along a fault stretching from Sumatra through the Nicobar Islands to the Andaman Islands.

Two oceanographic satellites, Jason-1 and TOPEX/Poseidon, passed over the propagating tsunami approximately two hours after the earthquake. These satellites follow almost identical orbits and repeat their tracks every 10 days (Menard et al. (2003)). The satellite data which is relevant to us is the sea surface anomaly. These data provide a cross section through the propagating tsunami including both direct and reflected waves in deep water.

The arrival times of one or more tsunami peaks were recorded by tide gauges at various points around the Indian Ocean. The advantage of this data is that it is available at a wider geographic range than is the satellite data, see Figure 7.1. However, the wave height observed at gauges on the coast is strongly influenced by relatively small scale bathymetric and coastal features which may be underresolved by the computational mesh or poorly represented in the bathymetry and coastline data. Where the sea adjacent to the measurement point is shallow, inaccuracies in the bathymetry representation can also affect the arrival times. In addition, data recorded at the tide gauge after the initial incident wave is unlikely to be modeled correctly since inaccurate local

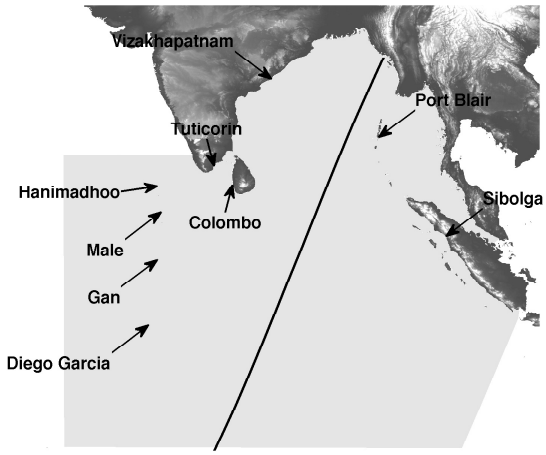

Figure 7.1: The Bay of Bengal and part of the Indian Ocean showing the path followed by the satellite Jason-1 and the gauge locations at which the arrival time of the tsunami is known.

bathymetry data can influence the representation of the local wave reflections.

7.1 The mesh

The shape of the coastlines and the bathymetry around the island chain where the tsunami was generated influence the reflections and the steering of the waves. It is therefore important to concentrate the highest resolution in coastal areas close to the tsunami source to be able to accurately represent the islands. The grid resolution in the deep ocean can be reduced since the length scale of wave features will be larger as the tsunami spreads out, than near the coast and in the shallow regions.

For grid generation GridGen geometrically based, automatic gridgenerator (Henry and Walters (1993)) which assumes that the element areas should be approximately proportional to local mean water depth was used. This means that the Courant number and hence the computational efficiency of model calculations is roughly uniform throughout the grid. The bathymetry shown in Figure 7.2 was drawn from the General Bathymetric Chart of the Oceans (GEBCO (2003)). This resource is, however, not entirely satisfactory, the bathymetry measurements are known to be sparse over much of the globe and the GEBCO data set relies extensively on interpolation.

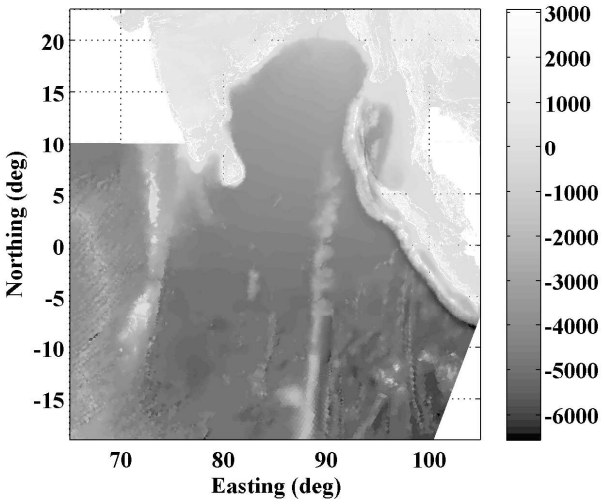

Figure 7.2: The bathymetry of the Indian Ocean based on the GEBCO data set.

For the unstructured mesh used by Pietrzak et al. (2007) the coastline was sampled at 500m resolution in areas of particular interest such as the Andaman and Nicobar Islands and at $1km$ on the Sumatran coast and parts of Thailand. Through $10km$ around Sri Lanka the resolution gradually decreases to $20km$ on Northern parts of the Indian coast. The seaward boundaries of the domain to the South and West were sampled at $40km$. The coastlines were based on the World Vector Shoreline produced by the US National Imagery and Mapping agency and published in GEBCO (2003). The grid was used as a base for generation of the bathymetry following grid, which was later adjusted to obtain smoother transitions close to the boundaries of the domain and orthogonalized. Additionally, the area close to the satellite track was meshed at about $5km$ resolution and the areas between the Nicobar Islands and the track was refined in order to obtain gradual changes in resolution. In total the grid has 550344 cells and 832532 edges. A part of the grid around the Andaman Islands is shown in Figure 7.3.

7.2 Model parameters and boundary settings

Inclusion of the large low resolution region in the South and West of the domain ensured that the water boundaries are removed from the area of interest of the simulation. For this reason it was considered appropriate to treat the

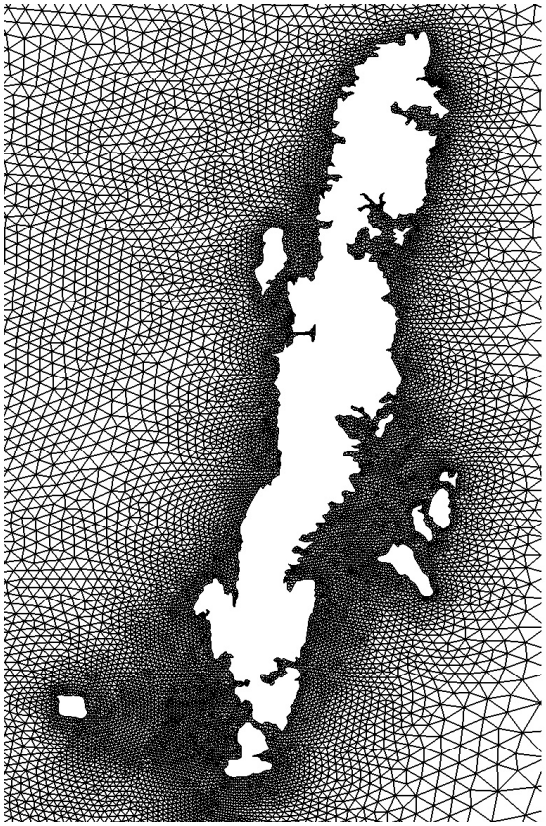

Figure 7.3: The mesh around the Andaman Islands.

boundaries as closed. Wind effects are ignored since they are unlikely to be observable on the time and length scales of the tsunami. Since the simulation is performed in the equatorial region, the Coriolis acceleration is also uniformly set to 0. The simulation was conducted with a single layer, since only the long wave propagation is of interest. The bed roughness length was set uniformly to $5cm$. The time step was set to $3s$; this value was chosen to adequately resolve the time scale of the initial rupture and subsequent wave propagation rather than by any stability limitations. To avoid artificial damping of the tsunami wave, the simulations were conducted with an implicitness parameter θ set to 0.5.

7.3 Initial conditions

The initial sea surface displacement is caused by the deformation of the sea floor. Here the sea bed kept unchanged while the sea surface was displaced using the two different uplift fields.

The first uplift field is from the GPS inversion Hoechner et al. (2008). The initial field "Sp2 60" presented there is shown in Figure 7.4(a) and referred here as Model 1. Slip starts at $94.7°E$, $3.1°N$ with a rupture velocity of $3.7km/s$ for the first $200km$ and then slowing down to $2km/s$, Vigny et al. (2005). The total rupture time is about 10min. The total sea floor deformation is shown in Figure 7.4(a).

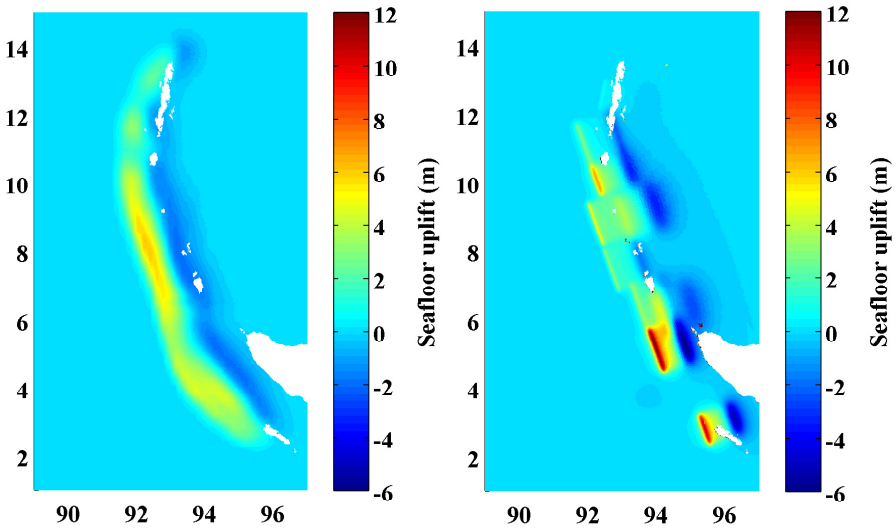

(a) Model 1 (b) Model 2

Figure 7.4: The initial conditions used for the simulation of the tsunami propagation: Model 1 (a) and Model 2 (b) total sea floor deformation.

The second sea floor uplift field is estimated by Tanioka et al. (2006) using coastal coseismic vertical deformations and wave forms at tide gauges. The same initial field was also used by Harig et al. (2008); Cui et al. (2010). The source area is divided into 12 subfaults and the whole Sumatra-Andaman earthquake is assumed to take 12 minutes at a rupture speed of approximately $1.7km/s$. The total sea floor deformation is shown in Figure 7.4(b). As the ini-

tial condition the sea surface elevation and velocity at the end of the earthquake as simulated by Harig et al. (2008) was used.

Both of the models have two separate patches of high slip. They are, however, in different locations. For Model 1 the separation is located at about 5°N, whereas Model 2 has maximum slip in approximately that location. The slip separation for Model 2 is located approximated 1° further south. Besides that maximum amplitude of the slip is approximately twice as large for Model 2 compared to Model 1.

7.4 Results

7.4.1 Tsunami propagation results

Figure 7.5 shows snapshots of the propagating tsunami wave at 30, 60 and 120 minutes after 0159 GMT simulated using both of the initial conditions shown in Figure 7.4. As can be seen, the tsunami wave simulated using the initial condition given by Model 1 propagates in the south-west direction significantly faster than that of the Model 2. The difference is caused by the longer southern patch of slip in Model 1 compared to Model 2 and speed of rupture.

Figure 7.6 shows a comparison of the recorded sea surface elevation along the Jason-1 satellite track with the modeled sea surface displacements. The model results were interpolated both in time and in space to the positions captured by the satellite. The results of Model 1 agree with the observed data quite well. It is able to reproduce the splitting of the first tsunami wave, which is due to the two separated slip maxima, one offshore Aceh and one around the Nicobar Islands. The amplitude of the first peak is correctly captured, the amplitude of the second one and the trough between the double peaks is, however, underestimated. The trough at $\approx 2250km$ is also well represented. The results obtained using initial fields given by Model 1 compare very well with the results from TUNAMI-N2, shown by Hoechner et al. (2008).

Figure 7.7 shows the instantaneous snapshot of the sea surface elevation along the satellite track after two hours of integration using Model 2 as initial condition. The figure shows a reasonable agreement with the results obtained by Harig et al. (2008). Accounting for the fact that it took about 10 minutes for the satellite to cross the tsunami gives quite a different result shown in Figure 7.6. Namely, late arrival and amplitude underestimation of the leading tsunami wave is observed.

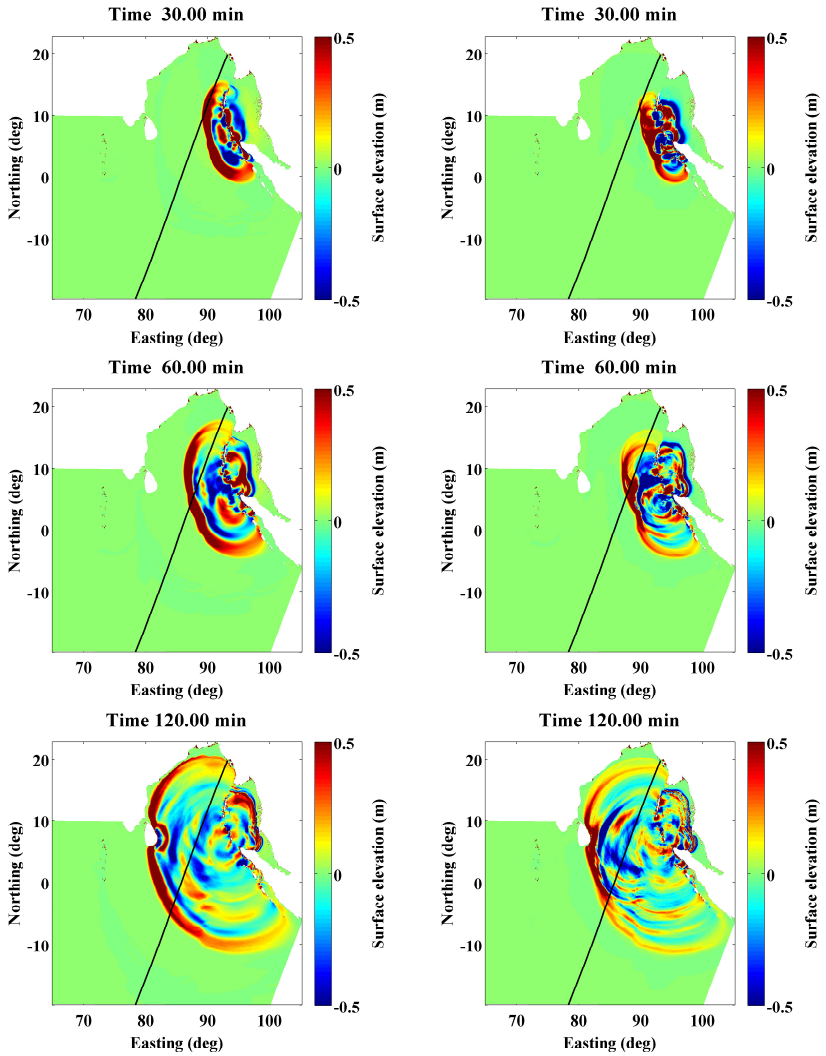

Figure 7.5: Snapshots of the evolution of the sea surface elevation the first 2 hours of the Indian Ocean Tsunami simulated using the sea floor uplift fields given by Model 1 (left) and Model 2 (right).

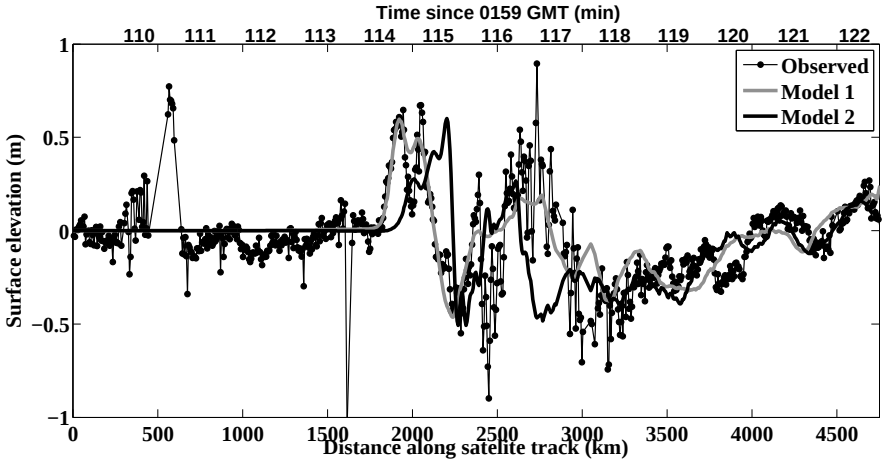

Figure 7.6: Comparison of modeled against observed sea surface elevation anomaly. The satellites altimeter data are shown in black.

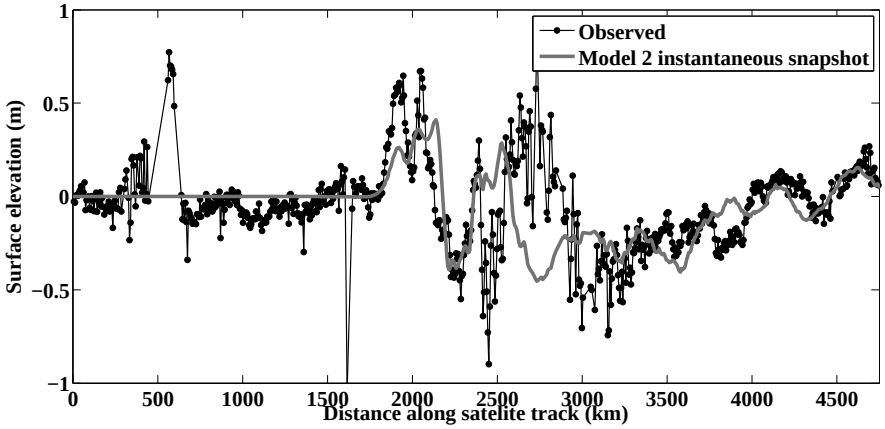

Figure 7.7: Comparison of the instantaneous snapshot of the sea surface elevation after 2 hours 12 minutes of simulation using the initial condition given by Model 2 to the observed sea surface anomaly. The satellites altimeter data are shown in black.

In order to better understand the features of the profile, simulations using variations of Model 1 were performed. Namely, only the Southern or the Northern part of the rupture as shown in Figure 7.8 was used as the initial condition. The comparison of the resulting surface elevations along the satellite track is shown in Figure 7.9. The first peak of the double peak feature recorded by Jason-1 is

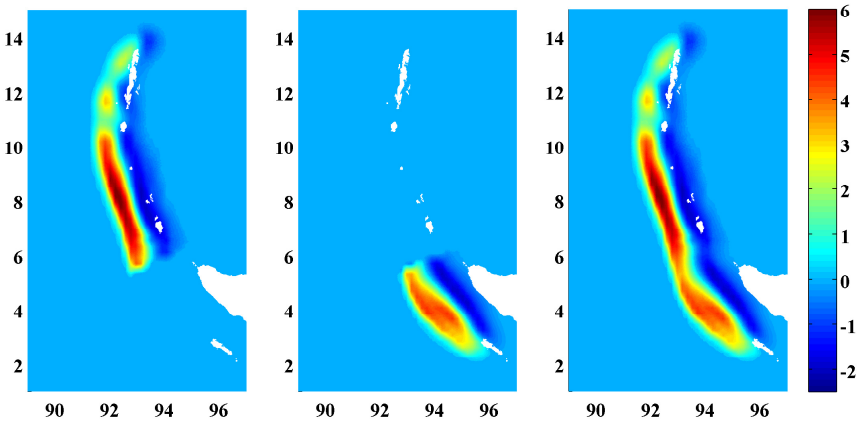

(a) Northern part (b) Southern part (c) Full rupture

Figure 7.8: Seafloor uplift field - Model 1.

an incident wave propagating in the south-west direction caused solely by the southern patch of slip located at $3 - 5^{\circ}N$. Whereas, the second peak is due to the combination of the incident waves originating from both the northern and southern patches of slip.

As can be seen from Figure 7.4(b) Model 2 assumes no slip at the above mentioned location, its Southern slip patch is much shorter and located further south-west. The incident waves caused by Model 2 required more time to propagate to the location where the double peak feature was recorded by the satellite. This explains the fact that the simulation driven by the Model 2 does not capture the double peak.

As mentioned before the amplitude of the second peak is underestimated by Model 1. To evaluate whether the peak can be better represented a simulation driven by the initial rupture given by Model 1 with doubled amplitude of the northern patch of slip was performed. The factor two was chosen since the maximum amplitude of the sea bed uplift field of Model 1 is approximately two times smaller than that of Model 2. Figure 7.10 shows the obtained sea

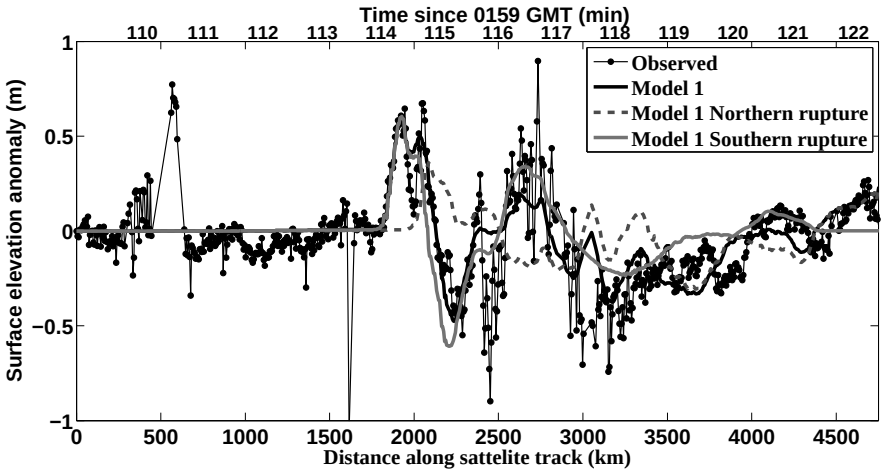

Figure 7.9: Comparison of modeled using Model 1 against observed sea surface elevation anomaly. The satellite altimeter data are shown in black.

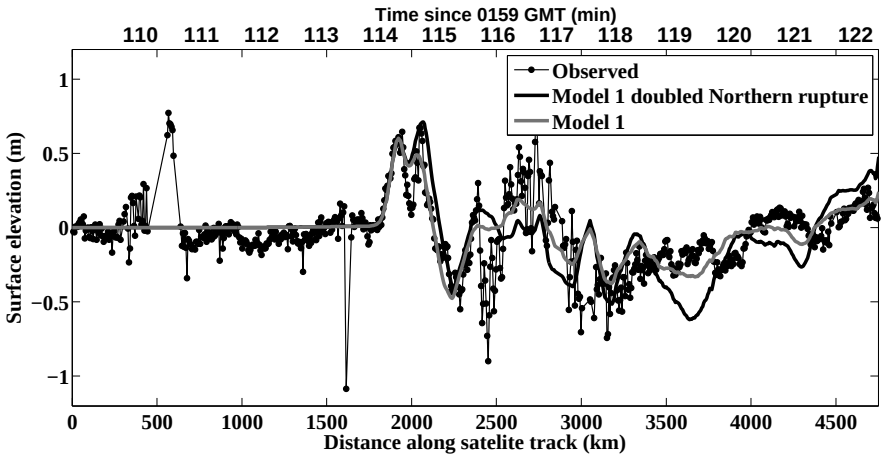

Figure 7.10: Comparison of the sea surface elevation anomaly modeled using two variants of Model 1. The satellites altimeter data are shown in black.

surface elevation along the satellite track together with the results of the original Model 1 and observations. As can be seen the amplitude of the second peak of the double peak feature is now correctly represented, a slight phase shift is however observed. The results also show slightly better representation of the amplitude of the third peak.

7.4.2 Arrival times comparison

Tsunami arrival times in minutes after the start of the earthquake recorded at a number of the tide gauges together with the gauge's sampling interval are listed in Table 7.1. Note that the tide gauge data are known to within 3-6 minutes. The tide gauge data are based on the extensive analysis conducted by Rabinovich and Thomson (2007). If there was a significant increase or decrease in water level between two observation points, they assumed that the actual arrival time was midway between the adjacent points at which the change occurred.

Table 7.1: Observed and modeled tsunami arrival times.

Site	Coordinates	Sampling interval of tide gauge (min)	Arrival times of the leading incident tsunami waves (in minutes since the earthquake started)		
			Tide gauge	Model 1 error	Model 2 error
Sibolga, Indonesia	01.75° N; 98.75° E	3	107	-24	-27
Tuticorin, India	08.75° N; 78.20° E	6	205	8	15
Vizakhapatnam, India	17.65° N; 83.28° E	5	156	-15	-11
Colombo, Sri Lanka	06.93° N; 79.83° E	2	170	-9	-2
Male, Maldives	04.18° N; 73.52° E	4	195	-5	1
Diego Garcia, UK	07.30° S; 72.38° E	6	226	-16	-8
Hanimadhoo, Maldives	06.77° N; 73.18° E	2	211	-15	-9
Gan, Maldives	00.68° S; 73.17° E	4	197	-7	3
Port Blair, India	11.68° N; 92.77° E	2	15	8	-

The modeled arrival times differ significantly between the simulations with different initial conditions, however they are accurate to within about 15 minutes for both of the models. The wave arrival time for Port Blair is not listed for Model 2, since the simulation started at 12 minutes after the beginning the earthquake and as indicated by the initial water level at that location after the arrival.

7.4.3 Simulation of flooding in the Banda Aceh

For this simulation the grid described above was extended to accommodate the land area of Banda Aceh, which was meshed at a resolution of about $100m$. The extended grid has in total 627788 cells with 208710 cells being dry originally. Part of the grid around Banda Aceh is shown in Figure 7.11. The

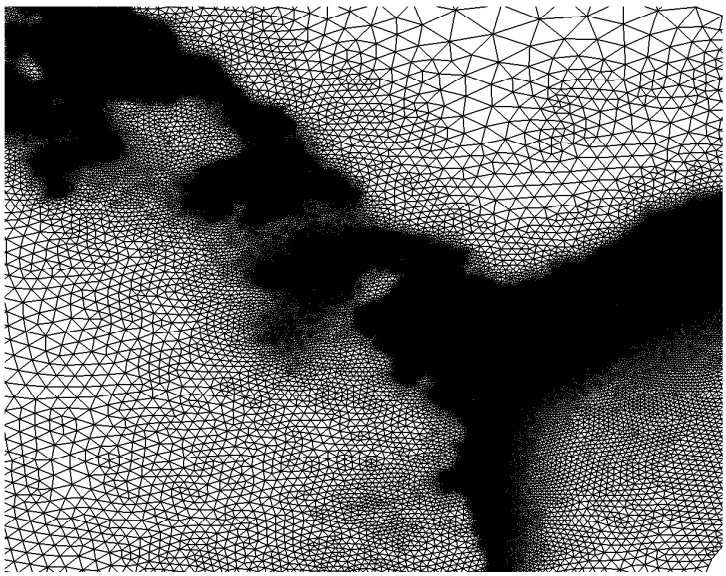

Figure 7.11: Part of the grid used for simulation of flooding in the Banda Aceh area.

simulation was performed for 2 hours with time step set to 0.25 seconds. The satellite image of the inundated regions is shown in Figure 7.12. Snapshots of the sea surface elevation in the Banda Aceh region during the flooding are shown in Figure 7.13.

As can be seen from Figure 7.13, Model 1 shows late arrival and low amplitude of the tsunami waves at the coast of Banda Aceh. As a result the flooded area is much smaller both compared to observations shown in Figure 7.12 and the results of Model 2. The late arrival of the tsunami waves can probably be explained by the fact that Model 1 assumes the rupture to be located farther to the west from the coast of Banda Aceh than Model 2.

Analyzing Model 2 initial field shown in Figure 7.4(b) one can conclude that flooding of the Banda Aceh area is mostly caused by the subfault located at $1^{\circ}S$. Model 1 uplift field has the slip separation at approximately that latitude, that is the rupture amplitude of Model 1 is about 3 times smaller there com-

Figure 7.12: The satellite image of the Tsunami affected areas acquired on December 29, 2004 by the Centre for Remote Imaging, Sensing and Processing at the National University of Singapore.

pared with Model 2. Therefore, increasing the rupture amplitude around 1° should improve the inundation results.

To check the conjecture a simulation driven by the previously used variant of the Model 1 initial field was performed. Namely, the amplitude of the rupture was increased by a factor of two for the Northern patch of slip. Figure 7.14 shows the inundation results compared to the results of the original Model 1. As can be seen the inundation results are improved especially on the east coast of Banda Aceh, however, they are still worse than that of Model 2.

7.4.4 Influence of the inundation process on the long wave propagation

Here the influence of the inundation process on the tsunami wave propagation is examined. Figure 7.15 shows comparison of the modeled sea surface elevation anomaly along the satellite track simulated incorporating the flooding process against that without flooding.

For both models only slight changes in the simulated sea surface elevation anomaly is observed. In both cases the changes in the sea surface elevation are observed between 2600 and $3500km$ along the satellite track. This is, how-

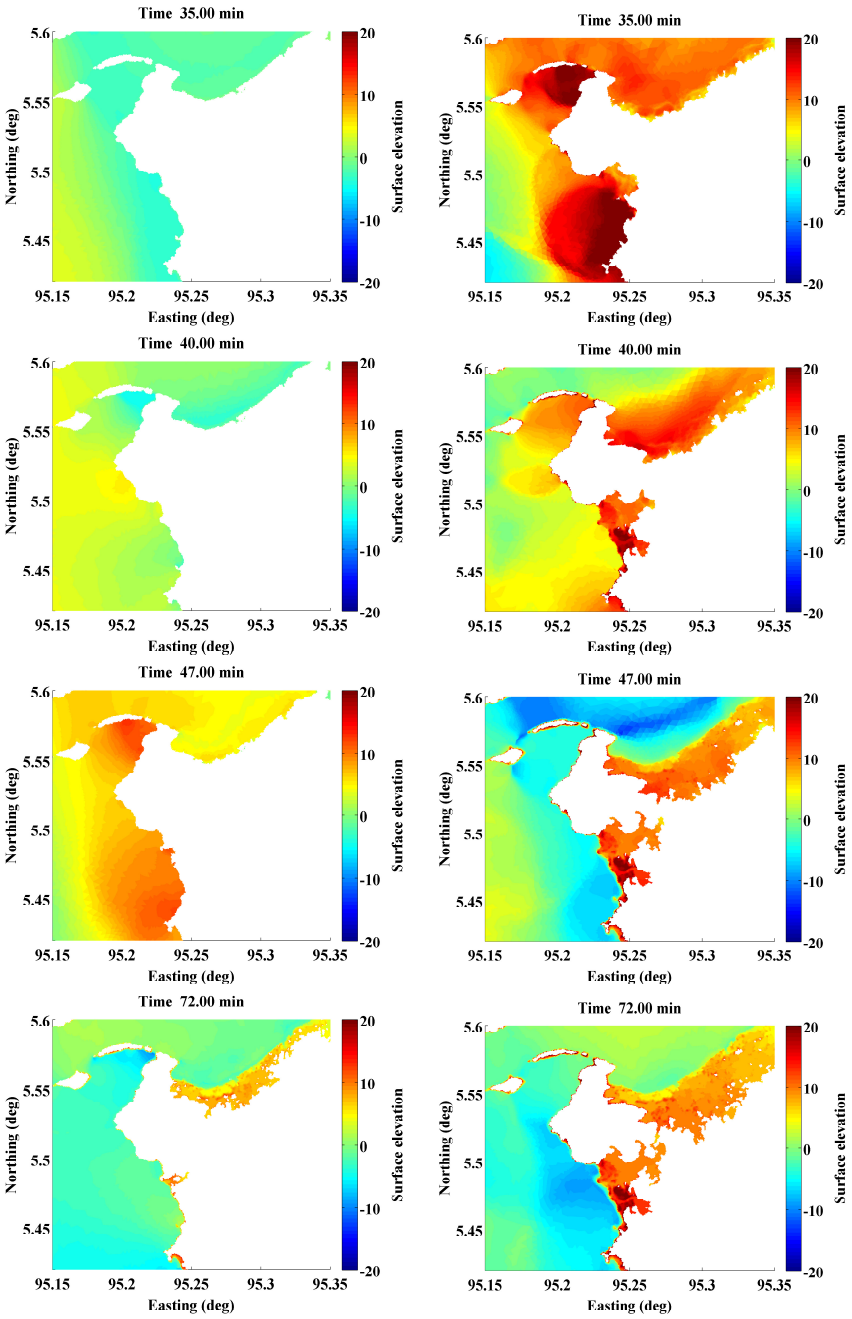

Figure 7.13: Snapshots of the sea surface elevation in the Banda Aceh area obtained using Model 1 (left) and Model 2 (right) initial fields.

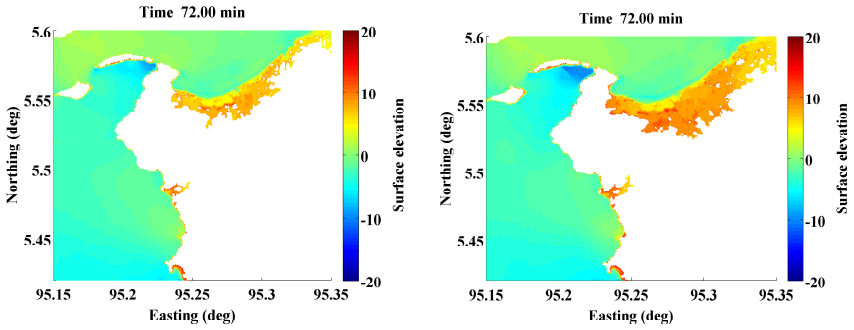

Figure 7.14: Snapshot of the sea surface elevation in the Banda Aceh area obtained using the initial field given by Model 1 (left) and its variant with doubled amplitude of the Northern part of rupture (right).

ever, expected since the double peak and the subsequent trough recorded by the Jason-1 satellite was caused by the incident wave. The interaction of incident and reflected waves was only observed on the later stages of the tsunami propagation. Also in both cases only amplitude, but not the shape of the reflected waves has changed.

7.5 Discussion

Here the ability of the model to simulate fast propagating tsunami waves and to accurately predict coastal inundation is shown. The results obtained using two different initial sea surface displacement fields were compared using a number of criteria. Namely, the model results are compared to the tide gauge data at the selected locations around the Indian Ocean, to satellite altimetry and to inundation results in the Banda Aceh area.

It is shown that although the initial fields give comparable arrival times the inundation results and the comparison to the satellite altimetry data are quite different. Modeled sea surface elevation along the satellite track obtained using the initial condition given by Model 1 are in a good agreement with the observations. The model, however, shows almost no flooding in the Banda Aceh area. The simulation driven by the Model 2 initial condition, on the other hand, shows good agreement with the observed inundation results, but not with the satellite altimetry data. These results, like similar studies, clearly show that the real uncertainties are in the source description. Although both the satellite altimetry and inundation measurement are valuable data sources,

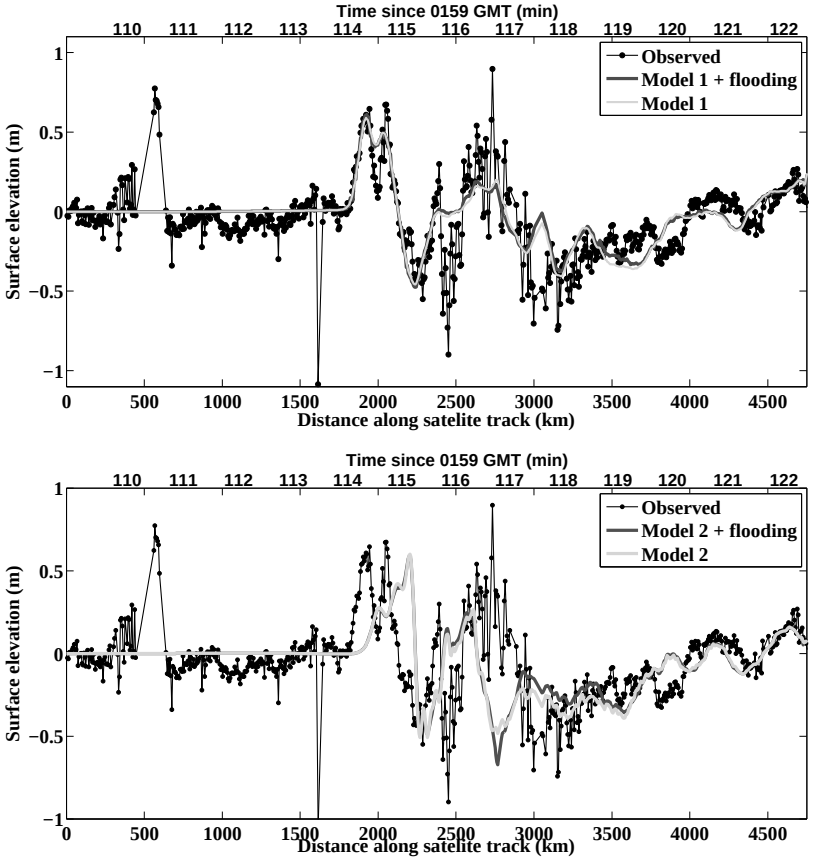

Figure 7.15: Comparison of modeled using Model 1 (top) and Model 2 (bottom) against observed sea surface elevation anomaly. The satellites altimeter data are shown in black.

it is not enough to compare to only one of them in order to assess the quality of an underlying rupture model.

Note also that in order to accurately model flooding and drying processes a very high resolution grid is to be employed. Although the grid used here has almost 6 times less nodes than the grid used by Harig et al. (2008) the model was still able to reproduce the inundation process quite well. The ability to handle complex geometries as typically found in coastal regions clearly demonstrates the advantage of using unstructured grids for coastal ocean applications.

8 Conclusions

In this thesis a new version of the unstructured staggered C-grid model, Delfin, for the shallow water equations is presented. The model, Delfin, was originally developed by Ham et al. (2005) and adopted as a starting point for the mixed finite difference finite volume approach by Casulli and Walters (2000). However, in Casulli and Walters (2000) and Ham et al. (2005) the advection is discretized using a semi-Lagrangian approach, which is shown to be stable at almost any Courant number. In the majority of the real life examples, however, a Courant number beneficial for using the semi-Lagrangian approach is not attainable. Besides that, most implementations of the semi-Lagrangian advection scheme do not provide momentum conservation and, thus, are not suitable for detailed modeling of flooding and drying processes. Therefore, the advection term is discretized in an Eulerian manner as described in Kleptsova et al. (2010). Although, most of the Eulerian advection schemes are momentum conservative in the 2D-case, special attention is required for the discretization of the momentum equation in the presence of multiple $z-$layers.

The main problem with $z-$layer models is connected with flow along a sloping bottom and surface. In this case the stepwise discontinuous representation of the topography and free surface can generate false flow structures, which is referred to as the staircase problem. Schemes of Fringer et al. (2006) and Stuhne and Peltier (2009) both employing the Eulerian advection scheme by Perot (2000) suffer from the staircase problem. Indeed, SUNTANS, the model of Fringer et al. (2006) does not conserve momentum in the cells that contain the free surface. SUNTANS is, however, mainly used for internal gravity wave simulations and the free surface dynamics are not their main concern. Stuhne and Peltier (2009) in their 3D global M2 tide simulation note deterioration of results in the coastal regions compared to their 2D simulation.

In Kleptsova et al. (2010) a local layer remapping procedure, which prevents the model from creating a vertical structure in the flow if there is no physical reason for that, is proposed. The idea behind the remapping procedure is that the discretized momentum equation for a particular layer should be identical to that of any other layer, if phenomena such as bottom friction, viscosity, diffusion are disregarded.

The C-grid methods use integral averages of vector components normal to the faces of the grid as the primary discrete unknowns, not the vectors themselves. It is often necessary to recover vectors from these spatially distributed vector components, such as for the calculation of momentum advection and Coriolis force, where the unknown tangential velocity component is needed. A linear combination of the normal velocity components of the surrounding faces is typically employed for this purpose, see for example Espelid et al. (2000); Bonaventura and Ringler (2005); Shashkov et al. (1998); Perot (2000).

While in the continuous system the Coriolis force is orthogonal to the velocity vector and, thus, makes no work, the discrete Coriolis term can become an infinite source of energy, Espelid et al. (2000). Therefore a proper velocity reconstruction should ensure that the discrete Coriolis operator is energetically neutral. Such a reconstruction is not unique, see for example Espelid et al. (2000); Ham et al. (2007); Kleptsova et al. (2009). In fact any linear combination of the normal velocity components can serve as an energetically-neutral tangential velocity reconstruction for a face, as soon as the normal velocity of the face itself is not included.

A velocity reconstruction which ensures no energy production due to the discrete Coriolis term does not, however, guarantee overall stability of the discrete system. In Kleptsova et al. (2009) it is shown that the reconstructed velocity field should also be consistent with the way the continuity equation is discretised. While being theoretically energy conservative the scheme can still become unstable if the above condition is violated. This is particularly true for the case of variable bottom topography. Note, that the Perot (2000) reconstruction automatically satisfies the continuity equation for the 3D shallow water equations and, in this case, the proper treatment of the bathymetry variations falls out naturally.

Different forms of the Navier-Stokes equations may have different conservation and symmetry properties and, thus, require different approaches to the velocity reconstruction procedure. Thuburn et al. (2009) use conservation of the potential vorticity as an additional consistency criterion in order to find a tangential velocity reconstruction for the 2D linearized shallow water equations

in the rotational form. Their work was generalized by Ringler et al. (2010) for the nonlinear shallow water equations in the rotational form. The velocity field was, however, still considered to be two-dimensional.

Similar to the other procedures, the methods by Thuburn et al. (2009); Ringler et al. (2010) assume the velocity component tangential to a face to be a linear combination of the normal velocity components of the surrounding faces. To find the weighting coefficients it is necessary to solve a linear system of equations, this makes the methods difficult to compare with others in the general case. For the case of uniform unstructured grids the methods are, however, identical to that of Perot (2000).

The ability of a model to conserve momentum and correctly represent vertical structure of a flow is crucial for the development of 3D models. It is the first step to modeling of the tidal motion and the associated thermal and density stratification, also in the regions of fresh water influence, as well as for studies of sedimentation processes caused by tsunami inundation.

Chapter 6 presents preliminary results which are the first steps towards development of a 3D multi-constituent high resolution model for the southern North Sea. It is shown that the model was able to accurately reproduce the essential characteristics of the M2 tide and the M4 and M6 overtides.

In Chapter 7 the ability of the model to simulate fast propagating tsunami waves and to accurately predict coastal inundation is shown. Two different initial sea surface displacement fields are used and the results are compared using a number of criteria. Namely, the model results are compared to tide gauge data at selected locations around the Indian Ocean, to satellite altimetry and to inundation results in the Banda Aceh area.

Although the initial fields give comparable arrival times, the inundation results and the comparison to the satellite altimetry data are quite different. Modeled sea surface elevation along the satellite track obtained using the initial condition given by Model 1 are in a good agreement with the observations. The model, however, shows almost no flooding in the Banda Aceh area. The simulation driven by the Model 2 initial condition, on the other hand, shows good agreement with the observed inundation results, but not with the satellite altimetry data. These results, like similar studies, clearly show that the real uncertainties are in the source description. Although both the satellite altimetry and inundation measurement are valuable data sources, it is not enough to compare to only one of them in order to assess the quality of an underlying rupture model.

In order to accurately model flooding and drying processes a high resolution

grid is to be employed. The ability to handle complex geometries, together with the possibility to use higher resolution in regions of particular interest, clearly demonstrates the advantage of using unstructured grids for coastal ocean applications.

8.0.1 Recommendations for future work

The model presented here guarantees no artificial vertical structure of the flow assosiated with stepwise discontinuous representation of the topography and free surface. The ability of the model to correctly reproduce a vertical structure existing in the flow is still to be evaluated. It is well known that the discontinuous representation of bathymetry in a $z-$layer model can cause large local truncation errors in the computation of bottom shear stress and near-bed turbulence along a sloping bottom. Platzek et al. (2012) show that the problem can be reduced through a local remapping to an equidistant layering near the bottom. Therefore a combination of the two layer remapping procedures could be investigated.

Non-hydrostatic effects form an important class of three dimensional phenomena occuring in the coastal ocean. It may be possible to incorporate non-hydrostatic correction terms, possibly in the manner proposed in Stelling and Zijlema (2003) or Cui et al. (2012). Scalar transport, which is a prerequisite for any sort of density current simulations as well as for many forms of turbulence model, is still missing in Delfin.

This thesis is mainly focused on the spatial discretization of the Coriolis and advection terms. However, no proper stability analysis of the numerical scheme has yet been carried out. It is recommended to carry these out in future studies.

Bibliography

Adcroft, A., Campin, J.-M., 2004. Rescaled height coordinates for accurate representation of free-surface flows in ocean circulation models. Ocean Modelling 7 (3-4), 269 – 284.

Adcroft, A., Hill, C., Marshall, J., 1997. Representation of Topography by Shaved Cells in a Height Coordinate Ocean Model. Monthly Weather Review 125 (9), 2293–2315.

Arakawa, A., Lamb, V., 1977. Computational design of the basic dynamical processes of the UCLA general circulation model. Methods in Computational Physics 17, 174267.

Balzano, A., 1998. Evaluation of methods for numerical simulation of wetting and drying in shallow water flow models. Coastal Engineering 34 (1-2), 83–107.

Baptista, A., Zhang, Y., Chawla, A., Zulauf, M., Seaton, C., Myers III, E., Kindle, J., Wilkin, M., Burla, M., Turner, P., 2005. A cross scale model for 3D baroclinic circulation in estuaryplumeshelf systems: II. Application to the Columbia River. Continental Shelf Research 25, 935–972.

Bleck, R., 2002. An oceanic general circulation model framed in hybrid isopycnic-Cartesian coordinates. Ocean Modelling 37, 55–88.

Bleck, R., Rooth, C., Hu, D., Smith, L., 1992. Ventilation patterns and mode water formation in a wind- and thermodynamically driven isopycnic coordinate model of the North Atlantic. Journal of Physical Oceanography 22, 1486–1505.

Bonaventura, L., Ringler, T., 2005. Analysis of discrete shallow-water models on geodesic Delaunay grids with C-type staggering. Monthly Weather Review 133 (8), 2351–2373.

Burchard, H., Petersen, O., 1997. Hybridization between $\sigma-$ and $z-$coordinates for improving the internal pressure gradient calculation in marine models with steep bottom slopes. International Journal for Numerical Methods in Fluids 25 (1), 1003–1023.

Campin, J.-M., Adcroft, A., Hill, C., Marshall, J., 2004. Conservation of properties in a free-surface model. Ocean Modelling 6 (3-4), 221 – 244.

Carrier, G. F., Wu, T. T., Yen, H., 2003. Tsunami run-up and draw-down on a plane beach. Journal of Fluid Mechanics 475, 79–99.

Casulli, V., Walters, R., 2000. An unstructured grid, three-dimensional model based on the shallow water equations. International Journal for Numerical Methods in Fluids 32 (3), 331–348.

Casulli, V., Zanolli, P., 2002. Semi-implicit numerical modeling of nonhydrostatic free-surface flows for environmental problems. Mathematical and Computer Modelling 36 (9-10), 1131–1149.

Casulli, V., Zanolli, P., 2005. High resolution methods for multidimensional advectiondiffusion problems in free-surface hydrodynamics. Ocean Modelling 10, 137–151.

Casulli, V., Zanolli, P., 2007. Comparing analytical and numerical solution of nonlinear two and three-dimensional hydrostatic flows. International Journal for Numerical Methods in Fluids 53 (6), 1049–1062.

Chen, Q., Kirby, J., Dalrymple, R., Kennedy, A., Chawla, A., 2000. Boussinesq modeling of wave transformation, breaking, and runup. II: 2D. Journal of Waterway, Port, Coastal and Ocean Engineering 126 (1), 48–56.

Cui, H., Pietrzak, J., Stelling, G., 2012. Improved efficiency of a non-hydrostatic, unstructured grid, finite volume model. Ocean Modelling 5455 (0), 55 – 67.

Cui, H., Pietrzak, J., Stelling, G., Androsov, A., Harig, S., 2010. Numerical Simulation of the 2004 Indian Ocean Tsunami: Accurate Flooding and drying in Banda Aceh. EGU General Assembly 2010, held 2-7 May, 2010 in Vienna, Austria, p.10280 12, 10280.

Dunbar, P., Stroker, K., McCullough, H., 2010. Do the 2010 Haiti and Chile earthquakes and tsunamis indicate increasing trends? Geomatics, Natural Hazards and Risk 1 (2), 95–114.

Espelid, T., Berntsen, J., 2007. Coriolis weighting on unstructured staggered grids. Ocean Modelling 16 (1-2), 61–75.

Espelid, T., Berntsen, J., Barthel, K., 2000. Conservation of energy for schemes applied to the propagation of shallow-water inertia-gravity waves in regions with varying depth . International Journal for Numerical Methods in Engineering 49 (12), 1521–1545.

Fringer, O., Gerritsen, M., Street, R., 2006. An unstructuredgrid, finite volume, nonhydrostatic, parallel coastal ocean simulator. Ocean Modelling 14, 139–173.

Fuhrman, D. R., Madsen, P. A., 2008. Simulation of nonlinear wave run-up with a high-order Boussinesq model. Coastal Engineering 55 (2), 139 – 154.

GEBCO, 2003. Centenary Edition of the GEBCO Digital Atlas. Published on CD-ROM on behalf of the Intergovernmental Oceanographic Commission and the International Hydrographic Organization as part of the General Bathymetric Chart of the Oceans; British Oceanographic Data Centre, Liverpool.

Gebraad, A., Philippart, M., 1998. The Dutch continental shelf model, DSCM98: calibration using altimeter data. . Tech. rep., RIKZ/OS-98.121x, Rijksinstituut voor Kust en Zee.

Griffies, S. M., Pacanowski, R. C., Schmidt, M., Balaji, V., 2001. Tracer Conservation with an Explicit Free Surface Method for z-Coordinate Ocean Models. Monthly Weather Review 129 (5), 1081–1098.

Hallberg, R., 1997. Stable split time stepping schemes for large-scale ocean modeling. Journal of Computational Physics 135 (1), 54–65.

Halyer, P. J., Lermusiaux, P. F. J., 2010. Multiscale two-way embedding schemes for free-surface primitive-equations in the "Multidisciplinary Simulation, Estimation and Assimilation System" (MSEAS). Article in press.

Ham, D., Kramer, S., Stelling, G., Pietrzak, J., 2007. The symmetry and stability of unstructured mesh C grid shallow water models under the influence of Coriolis. Ocean Modelling 16 (1-2), 47–60.

Ham, D., Pietrzak, J., Stelling, G., 2005. A scalable unstructured grid 3-dimensional finite volume model for the shallow water equations. Ocean Modelling 10, 153–169.

Ham, D. A., 2006. On techniques for modelling coastal and ocean flow with unstructured meshes. Ph.D. thesis, Technische Universiteit Delft.

Hanert, E., Legat, V., Deleersnijder, E., 2003. A comparison of three finite elements to solve the linear shallow water equations. Ocean Modelling 5 (1), 17 – 35.

Hanert, E., Walters, R. A., Roux, D. Y. L., Pietrzak, J. D., 2009. A tale of two elements: and RT0. Ocean Modelling 28 (1-3), 24 – 33.

Harig, S., Chaeroni, ., Pranowo, W., Behrens, J., 2008. Tsunami simulations on several scales. Ocean Dynamics 58, 429–440.

Henry, R. F., Walters, R. A., 1993. Geometrically based, automatic generator for irregular triangular networks. Communications in Numerical Methods in Engineering 9, 555 – 566.

Hoechner, A., Babeyko, A., Sobolev, S., 2008. Enchances GPS inversion technique applied to the 2004 Sumatra earthquake and tsunami. Geophysical research letters 35 (8), L08310.

Houbolt, J., 1968. Recent sediment in the southern bight of the North Sea. Geol. Mijnbouw 47, 245–273.

Hyman, J. M., Shashkov, M., 1999. The Orthogonal Decomposition Theorems for Mimetic Finite Difference Methods. SIAM J. Numer. Anal. 36 (3), 788–818.

Kanoglu, U., Synolakis, C. E., 1998. Long wave runup on piecewise linear topographies. Journal of Fluid Mechanics 374, 1–28.

Kleptsova, O., Pietrzak, J. D., Stelling, G. S., 2009. On the accurate and stable reconstruction of tangential velocities in C-grid ocean models. Ocean Modelling 28 (1-3, Sp. Iss. SI), 118–126.

Kleptsova, O., Pietrzak, J. D., Stelling, G. S., 2012. On a momentum conservative z-layer unstructured C-grid ocean model with flooding. Ocean Modelling 54-55, 18–36.

Kleptsova, O., Stelling, G., Pietrzak, J., 2010. An accurate momentum advection scheme for a z-level coordinate models. Ocean Dynamics 60, 1447–1461.

Kliem, N., Pietrzak, J., 1999. On the pressure gradient error in sigma coordinate ocean models: A comparison with a laboratory experiment. Journal of Geophysical Research 104 (C12), 29781–29799.

Kramer, S. C., Stelling, G. S., 2008. A conservative unstructured scheme for rapidly varied flows. International Journal For Numerical Methods in Fluids 58 (2), 183–212.

Lynett, P., Wu, T.-R., Liu, P.-F., 2002. Modeling wave runup with depth-integrated equations. Coastal Engineering 46 (2), 89–107.

Menard, Y., Fu, L.-L., Escudier, P., Parisot, F., Perbos, J., Vincent, P., Desai, S., Haines, B., Kunstmann, G., 2003. The Jason-1 Mission. Marine Geodesy 26 (3-4), 131–146(16).

Miglio, E., Quarteroni, A., Saleri, F., 1999. Finite element approximation of Quasi-3D shallow water equations. Computer Methods in Applied Mechanics and Engineering 174 (3), 355–369.

NOAA, 2010. US National Hurricane Centre.
URL http://www.nhc.noaa.gov/ssurge

Otto, L., Zimmerman, J., Furnes, G., Mork, M., Saetre, R., Becker, G., 1990. Review of the physical oceanography of the North Sea. Netherlands Journal of Sea Research 26 (2-4), 161 – 238.

Perot, B., 2000. Conservation properties of unstructured staggered mesh schemes. Journal of Computational Physics 159 (1), 58–89.

Perot, J. B., Vidovic, D., Wesseling, P., 2006. Mimetic reconstruction of vectors. Ima volumes in mathematics ant its applications 142, 173–188.

Pietrzak, J., Jakobsen, J., Burchard, H., Vested, H., Petersen, O., 2002. A Three-Dimensional Hydrostatic Model for Coastal and Ocean Modelling using a Generalised Topography following Co-ordinate System. Ocean Modelling 4, 173–205.

Pietrzak, J., Socquet, A., Ham, D., Simons, W., Vigny, C., Labeur, R. J., Schrama, E., Stelling, G., Vatvani, D., 2007. Defining the source region of the Indian Ocean Tsunami from GPS, altimeters, tide gauges and tsunami models. Earth and Planetary Science Letters 261, 49–64.

Pingree, R. D., Griffiths, D. K., 1978. Tidal Fronts on the Shelf Seas Around the British Isles. J. Geophys. Res. 83, 4615–4622.

Platzek, F., Stelling, G., Jankowski, J., Patzwahl, R., 2012. On the representation of bottom shear stress in z-layer models. Proceedings of HIC 2012 - 10th International Conference on Hydroinformatics, Hamburg, Germany.

Proudman, J., Doodson, A. T., 1924. The Principal Constituent of the Tides of the North Sea. Philosophical Transactions of the Royal Society of London.

Series A, Containing Papers of a Mathematical or Physical Character 224, 185–219.

Rabinovich, A., Thomson, R., 2007. The 26 December 2004 Sumatra Tsunami: Analysis of Tide Gauge Data from the World Ocean Part 1. Indian Ocean and South Africa. Pure and Applied Geophysics 164, 261–308.

Ringler, T. D., Thuburn, J., Klemp, J. B., Skamarock, W. C., 2010. A unified approach to energy conservation and potential vorticity dynamics for arbitrarily-structured C-grids. J. Comput. Phys. 229, 3065–3090.

Robinson, I., 1983. Chapter 7: Tidally Induced Residual Flows. In: Johns, B. (Ed.), Physical Oceanography of Coastal and Shelf Seas. Vol. 35 of Elsevier Oceanography Series. Elsevier, pp. 321 – 356.

Shashkov, M., Swartz, B., Wendroff, B., 1998. Local reconstruction of a vector field from its normal components on the faces of grid cells. Journal of Computational Physics 139 (2), 406–409.

Simpson, J., Hunter, J. R., 1974. Fronts in the Irish Sea. Nature 250, 404–406.

Stelling, G., Duinmeijer, S., 2003. A staggered conservative scheme for every Froude number in rapidly varied shallow water flows. International Journal for Numerical Methods in Fluid 43 (12), 1329–1354.

Stelling, G., Van Kester, J., 1994. On the approximation of horizontal gradients in sigma co-ordinates for bathymetry with steep bottom slopes. International Journal for Numerical Methods in Fluids 18, 915–935.

Stelling, G., Zijlema, M., 2003. An accurate and efficient finite-difference algorithm for non-hydrostatic free-surface flow with application to wave propagation. International Journal for Numerical Methods in Fluids 43 (1), 1–23.

Strang, G., 1988. Linear Algebra and its Applications, 3rd Edition. Harcourt Brace.

Stuhne, G., Peltier, W., 2009. An unstructured c-grid based method for 3-d global ocean dynamics: Free-surface formulations and tidal test cases. Ocean Modelling 28 (1-3), 97 – 105.

Tanioka, Y., Yudhicara, Kususose, T., Kathiroli, S., Nishimura, Y., Iwasaki, S., Satake, K., 2006. Rupture process of the 2004 great Sumatra-Andaman earthquake estimated from tsunami waveforms. Earth, Planets, and Space 58, 203–209.

Taylor, G. I., 1922. Tidal Oscillations in Gulfs and Rectangular Basins. Proc. London Math. Soc. s2-20 (1), 148–181.

Thacker, W. C., 1981. Some exact solutions to the nonlinear shallow-water wave equations. Journal of Fluid Mechanics Digital Archive 107 (-1), 499–508.

Thuburn, J., Ringler, T. D., Skamarock, W. C., Klemp, J. B., 2009. Numerical representation of geostrophic modes on arbitrarily structured C-grids. J. Comput. Phys. 228, 8321–8335.

Vigny, C., Simons, W. J. F., Abu, S., Bamphenyu, R., Satirapod, C., Choosakul, N., Subarya, C., Socquet, A., Omar, K., Abidin, H. Z., Ambrosius, B. A. C., 2005. Insight into the 2004 Sumatra-Andaman earthquake from GPS measurements in southeast Asia. Nature 436, 201–206.

Walters, R., Casulli, V., 2001. A robust, finite element model for hydrostatic surface water flows. Communications in Numerical Methods in Engineering 14 (10), 931–940.

Walters, R. A., Lane, E. M., Hanert, E., 2009. Useful time-stepping methods for the coriolis term in a shallow water model. Ocean Modelling 28 (1-3), 66 – 74, the Sixth International Workshop on Unstructured Mesh Numerical Modelling of Coastal, Shelf and Ocean Flows.

Wenneker, I., Segal, A., P., W., 2002. A Mach-uniform unstructured staggered grid method. International Journal for Numerical Methods in Fluids 40 (9), 1209–1235.

Zimmerman, J., 1981. Dynamics, diffusion and geomorphological significance of tidal residual eddies. Nature 290 (5807), 549–555.

List of Publications

1. O. Kleptsova, J.D. Pietrzak, and G.S. Stelling, **On the accurate and stable reconstruction of tangential velocities in C-grid ocean models**, *Ocean Modelling*, Volume 28, Issue 1-3, pp. 118–126, 2009.

2. O. Kleptsova, G.S. Stelling and J.D. Pietrzak, **On accurate momentum advection scheme for a z-level coordinate models**, *Ocean Dynamics*, Volume 60, Issue 6, pp. 1447–1461, 2010.

3. O. Kleptsova, J.D. Pietrzak, and G.S. Stelling, **On a momentum conservative z-layer unstructured C-grid ocean model with flooding**, *Ocean Modelling*, Volume 54-55, pp. 18–36, 2012.

Curriculum Vitae

Olga Kleptsova was born in Sidorovka, USSR, in 1978. In 2002 she received the engineer degree in applied mathematics and informatics from Ufa State Aviation Technical University, Ufa, Russian Federation. In 2005 she received the MSc degree in applied mathematics from Delft University of Technology, Delft, The Netherlands.

Subsequently in 2005 she started to work as a PhD student in the Fluid Mechanics Section of the Faculty of Civil Engineering and Goesciences of Delft University of Technology. The results of her work are presented in this thesis and the three referenced publications.

Since August 2011 Olga works as a Junior Advisor/Researcher at Deltares Software Centre, Deltares, Delft.